Cosmology with the galaxy bispectrum

Dissertation
zur
Erlangung des Doktorgrades (Dr. rer. nat.)
der
Mathematisch-Naturwissenschaftlichen Fakultät
der
Rheinischen Friedrich-Wilhelms-Universität Bonn

von
Victoria Yankelevich
aus
Rostow am Don, Russland

Bonn, 2019

Dieser Forschungsbericht wurde als Dissertation von der Mathematisch-Naturwissenschaftlichen Fakultät der Universität Bonn angenommen und ist auf dem Hochschulschriftenserver der ULB Bonn http://nbn-resolving.de/urn:nbn:de:hbz:5n-56046 elektronisch publiziert.

1. Gutachter:	Prof. Dr. Cristiano Porciani
2. Gutachter:	Prof. Dr. Peter Schneider
Tag der Promotion:	26.09.2019
Erscheinungsjahr:	2019

To my mom and my uncle

Двум кандидатам, воспитавшим одного доктора

Abstract

The last decades witnessed huge progress in understanding the large-scale structure of the Universe. While homogeneous and isotropic on the largest scales, the matter and galaxy distributions display complex patterns on smaller scales where we observe elongated filaments, compact clusters and volume-filling underdense regions. These features are not captured by studies of two-point statistics like the power spectrum that does not retain information on the phases of the Fourier modes of the density field. Therefore, higher-order statistics like the bispectrum should provide additional information. However, the exact gain has never been measured convincingly.

Current and forthcoming galaxy redshift surveys, such as *Euclid*, cover large enough volumes to provide robust measurements of the bispectrum. For this reason, it is a perfect time to develop the tools to interpret these measurements and extract cosmological information out of them. The main goals of this work are to explore this field, to study the properties of the bispectrum, discover and demonstrate advantages and difficulties of making the bispectrum a useful and applicable tool to learn more about the Universe.

Historically the bispectrum has been considered a useful tool to learn about the statistical properties of the primordial density perturbations that seeded structure formation, and to study non-linear processes like gravitational dynamics and galaxy biasing. Since these processes generate different functional dependencies on the triangular configurations, they can be disentangled by fitting bispectrum measurements with theoretical templates. This will ultimately remove the degeneracy between the linear bias coefficient and the amplitude of the dark matter perturbations found in power-spectrum studies.

However, the potential of the bispectrum as a means to extract additional cosmological information has never been explored. One part of my thesis has been devoted to quantifying this potential using the Fisher-matrix formalism.

Firstly, it is necessary to understand the power of the bispectrum as a statistic for extracting cosmological information and its advantages with respect to the classic power spectrum analysis. For this research we developed a code for evaluating the Fisher matrix and the covariance matrix for the power spectrum, the bispectrum and their combination with redshift space distortions considering ΛCDM, wCDM and w_0w_aCDM models and using tree-level perturbation theory. As the result, the Fisher matrix forecasts for all these cosmological parameters are presented. Our study shows that there is a clear advantage in combining the power spectrum and the bispectrum to infer the galaxy bias parameters and constrain the dark-energy equation of state.

Another significant problem is compressing the information contained in the bispectrum. In this work, we are using all possible variants of triangles and it is necessary to combine them in a sensible way, which from one hand will be possible to compare with observational data and from the other hand provide a good statistics. The bispectrum is described by five variables: three of them fix the shape of a triangle and two others fix the orientation in space. We explored the symmetry of the

bispectrum with respect to its triangular bin spatial orientation. Results demonstrate that with a one quarter of the original parameter space it is possible to describe all configurations. That helps saving computation time and resources.

Finally, there is another issue related to compression of the bispectrum data. It is unclear how to optimally bin the bispectrum and how to compute theoretical models for the binned data. Different strategies affect accuracy and computational cost. These research provide the golden mean between computational resources and accuracy. We have developed several ways of calculating the bispectrum for a given theoretical model by averaging differently the variables. The advantages and disadvantages of this approach will depend on the specific purpose of the required task. The ultimate purpose of this research is to demonstrate an optimal way of compressing the information to compare it against actual observational data.

List of publications

Publication included in the thesis

- **[Chapter 2] V. Yankelevich** & C. Porciani (2019). Cosmological information in the redshift-space bispectrum. *Monthly Notices of the Royal Astronomical Society*, 483, 2078. arXiv:1807.07076;

Publication included in the thesis (in preparation)

- **[Chapter 3] V. Yankelevich** & C. Porciani. Binning effects on cosmological constraints from the bispectrum. Prepairing for submittion to *Monthly Notices of the Royal Astronomical Society*;

Other publications

- *Euclid* Collaboration, A. Blanchard, S. Camera, C. Carbone, V.F. Cardone, S. Casas, S. Clesse, S. Ilić, M. Kilbinger, T. D. Kitching, M. Kunz, F. Lacasa, E. Linder, E. Majerotto, K. Markovič, M. Martinelli, V. Pettorino, A. Pourtsidou, Z. Sakr, Ariel G. Sánchez, I. Tutusaus, S. Yahia-Cherif, **V. Yankelevich** (2019). Forecast validation for the *Euclid* satellite. To be submitted to *Astronomy & Astrophysics*.
- **V. Yankelevich** & S. Pilipenko (2018). Scaling the dark matter halo mass function. *Open Astronomy*, 27, 150. arXiv:1503.04650;
- **V. Yankelevich** (2014). Notes on counter-orbiting globular clusters in the Milky Way. *Astronomical & Astrophysical Transactions*, 28, 347. arXiv:1401.3704;

Contents

CHAPTER 1

Introduction

Cosmology (from the Greek $\kappa\acute{o}\sigma\mu o\varsigma$, kosmos – 'world' and $\lambda o\gamma\iota\alpha$, logia – 'discourse') is the study of the origin and evolution of the Universe. Since prehistoric times, people have been fascinated by the night sky. Originating in ancient Egypt and Mesopotamia, Babylon and China, and evolving from astrology to astronomy, cosmology became established as a science.

Today, cosmology is the science on a junction of astronomy, astrophysics, theoretical physics and particle physics. It combines together theoretical studies, observations and computational simulations. Cosmology describes and explains the origin of the Universe, its evolution in the past and current times, and predicts its future development.

One pillar of modern cosmology is the cosmological principle, which is based on the fundemental idea that there are no distinguished observers and that space appears uniform in all directions. The combination of this statement together with the admission of isotropy of the Universe, results in the assumption of homogeneity of the Universe.

Other pillars of cosmology are the Big Bang and inflation theories. The Universe formed ~ 13.7 billion years ago from a hot, dense singularity with radiation as the dominant form of energy. Then, during 10^{-37} seconds, the Universe expanded more than 60 e-folds. This process is called inflation. It is assumed that some scalar field ϕ, the inflaton, characterised by negative pressure, caused rapid expansion of the Universe. This sudden increase in size due to inflation distributes the small-scale fluctuations of the initial scalar field to all points of the expanding Universe. This explains why some parts of the Universe, at distances greater than the distance light can travel in ~ 13.7 billion years, have the same properties. After the inflation period ended, the Universe continued expanding (but with deceleration) and cooling. With the decreasing Universe temperature, firstly, free quarks and gluons condensed into baryons. Then, at the recombination era, protons and electrons combined to form neutral hydrogen atoms, and photons became free travel without interactions. Within the first three minutes after the Big Bang, the lightest elements (hydrogen, helium and lithium) formed. If we increase the time steps, later, dark matter formed haloes due to the gravitational force. Baryons then gave rise to the first stars and later proto-galaxies. Nuclear fusion in the first stars formed heavy elements. Up to the present day, galaxies continued to form. Finally, after ~ 13.7 from the moment of origin, we see the Universe as it is now. However, it is necessary to mention, that current observations show us the past of the Universe. The finite speed of light results in the phenomenon of always looking back into the past as light needs time to travel form the source to the observer. At greater observed distances, the Universe appears younger. This makes it impossible to see the current picture of the

Universe, we always observe the past.

We do not know if our Universe is unique, or if other universes exist. The multiverse theory studies a variety of possible universes. In this work, we study only our Universe. All assumptions are made base on this fact, as we can observe only parts of our Universe. And finally, we live only in this Universe.

The general concepts of cosmology presented in this Chapter, are based on the literature of Peebles (1993); Peacock (1999); Barkana & Loeb (2001); Bernardeau et al. (2002); Dodelson (2003); Schneider (2006); Gorbunov & Rubakov (2011a,b) if not stated otherwise.

1.1 Very brief history of cosmology

The key moments in the history of cosmology, which are relevant for the following work, are presented here.

1915: Albert Einstein published the final version of the General Relativity (GR). This marks the beginning of modern cosmology.

1917: Albert Einstein firstly introduced the concept of the cosmological constant. Originally, it supposed to cancel the effects of gravity and achieve a static universe.

1922/1927: Cosmological solutions of the field equations of GR are presented by Alexander Friedmann and Georges Lemaître. In 1935 Howard Robertson and Arthur Walker found geometrical solution for the same problem. Because of this historical reason, the exact solution of Einstein's field equations of GR is called the Friedmann–Lemaître–Robertson–Walker (FLRW) metric.

1928: Edwin Hubble discovered the cosmic expansion and this finished the era of a static universe. The Hubble law was formulated (Fig. 1.1)[1].

1933: The measurement of the velocity dispersion with a virial theorem in the Coma Cluster made by Fritz Zwicky demonstrated the evidence of unseen mass ('dunkle Materie'/'dark matter').

1946: George Gamow predicted the Cosmic Microwave Background (CMB) with a temperature ~ 5 K as a relict of the Big Bang.

1965: Arno Penzias and Robert Wilson discovered the CMB with a temperature ~ 3 K. ★ 1978: Nobel Prize in physics.

1970 (1950-1970): The first galaxy redshift survey was made by Gerard de Vaucouleurs.

1970: Vera Rubin studied the rotation curves of spiral galaxies and demonstrated the necessity of dark matter (Fig. 1.2).

1974: Bill Press and Paul Schechter estimated the abundance of massive gravitationally bound objects.

1981: The first paper about inflation published by Alan Guth. The beginning of the inflation cosmology era.

1981: Estimation that there are three neutrino families (according to the measurement of the helium content of the Universe) (e.g. Yang et al., 1979; Schramm & Steigman, 1981).

1985 - current time: The era of the numerical cosmology. The Cold Dark Matter (CDM) model became established (e.g. Davis et al., 1985).

1986: The first clear picture of the large scale structure (LSS) of the Universe done by the Center for Astrophysics (CfA) redshift survey.

1992: *RELIKT-1* satellite detected the anisotropy of the CMB.

[1] [1]This Fig. is taken from the original paper (Hubble, 1929) and it has a typo on units of velocity. It should be km/s.

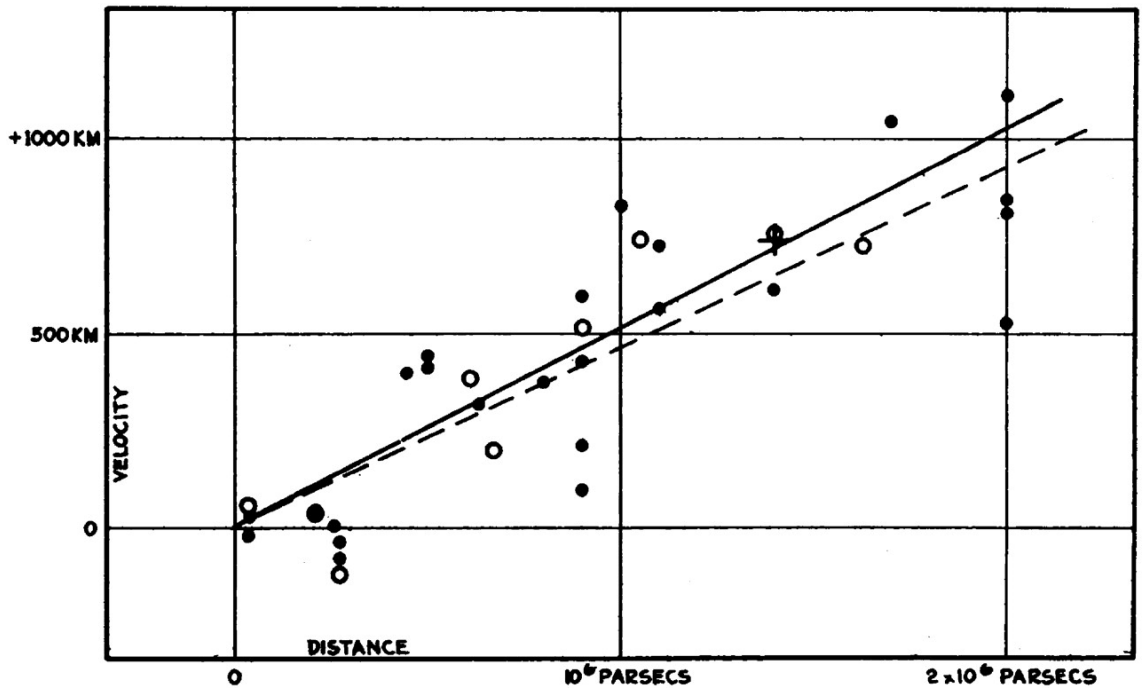

Figure 1.1: Velocity-distance relation among extra-galactic nebulae. Credit: Hubble (1929).

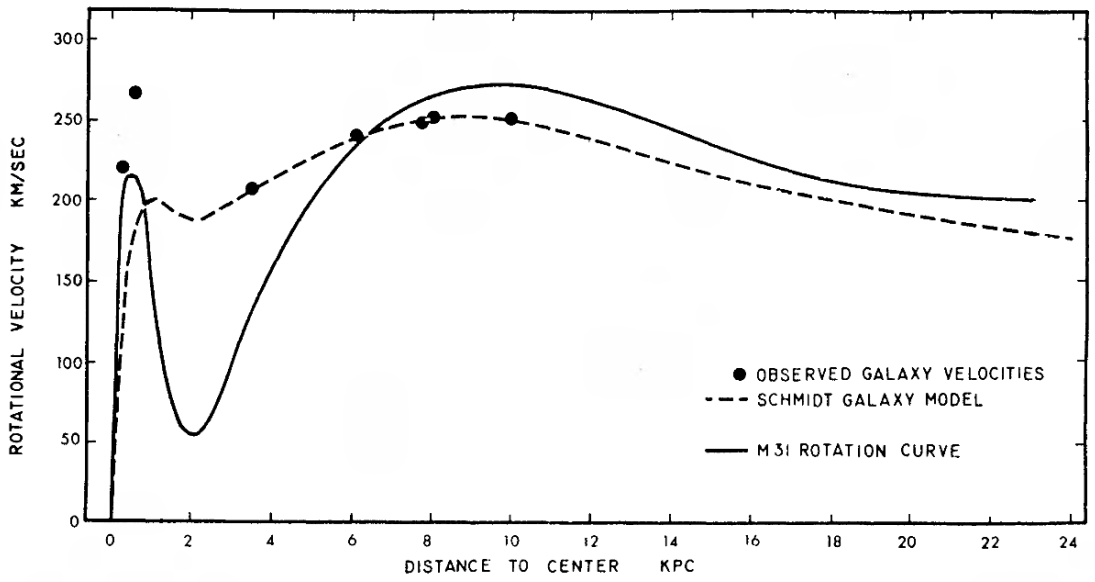

Figure 1.2: The comparison of observed rotation curves for Andromeda galaxy (M31) with theoretical predictions. Credit: Rubin & Ford (1970).

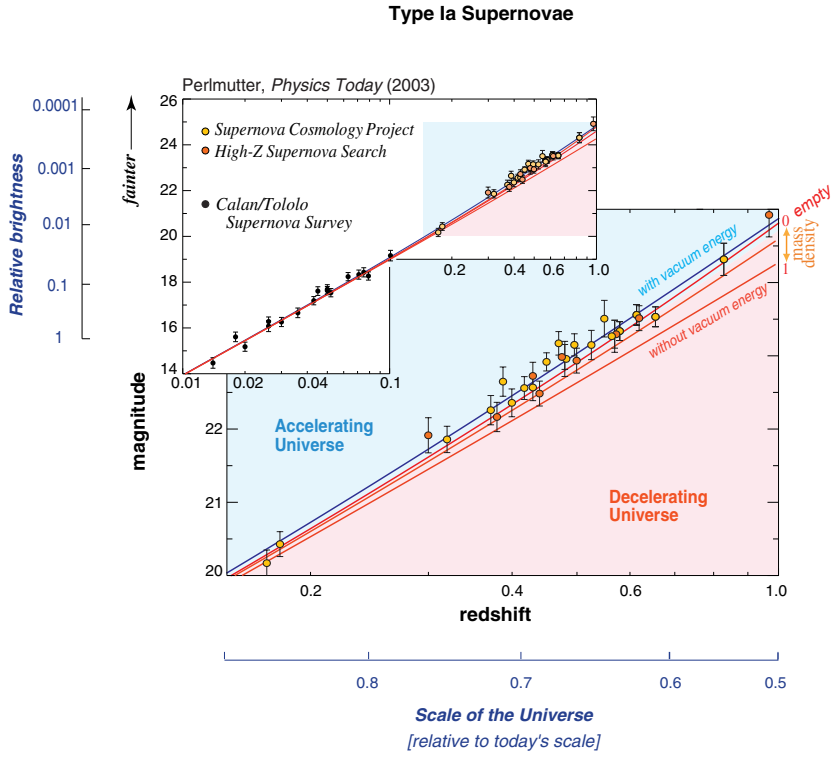

Figure 1.3: Observed magnitude versus redshift for well measured distant and (in the inset) nearby type Ia supernovae. Credit: http://supernova.lbl.gov.

1992: The first map of the CMB made by the *Cosmic Background Explorer* (*COBE*) (1989-1993) satellite. Detection of the CMB anisotropy, measurement of amplitude of the temperature fluctuations ($\sim 10^{-5}$). ★ 2006: Nobel Prize in physics for John Mather and George Smoot.

1998: The Universe is expanding with acceleration! The observation of the supernovae type Ia demonstrate the need of a non-zero cosmological constant to describe the expansion with accelerating rate (Fig. 1.3). ★ 2011: Nobel Prize in physics for Saul Perlmutter, Brian Schmidt and Adam Riess.

2001: The launch of the *Wilkinson Microwave Anisotropy Probe* (*WMAP*) satellite – the mission to measure the CMB temperature fluctuations. The first results came in 2003 and confirmed the standard cosmological model.

2001: The first results from the Two-degree Field Galaxy Redshift Survey (2dFGRS) came out and confirmed that the matter density is only 30 per cent of critical density.

2002: The first catalog of galaxies and their spectra was released by the Sloan Digital Sky Survey (SDSS).

2004: The Millennium Simulation (cosmological N-body simulation) finished and provided a detailed picture of evolution of matter structure over time (Fig. 1.4).

2005: The baryonic acoustic oscillations (BAO) have been detected for the first time in CfA and

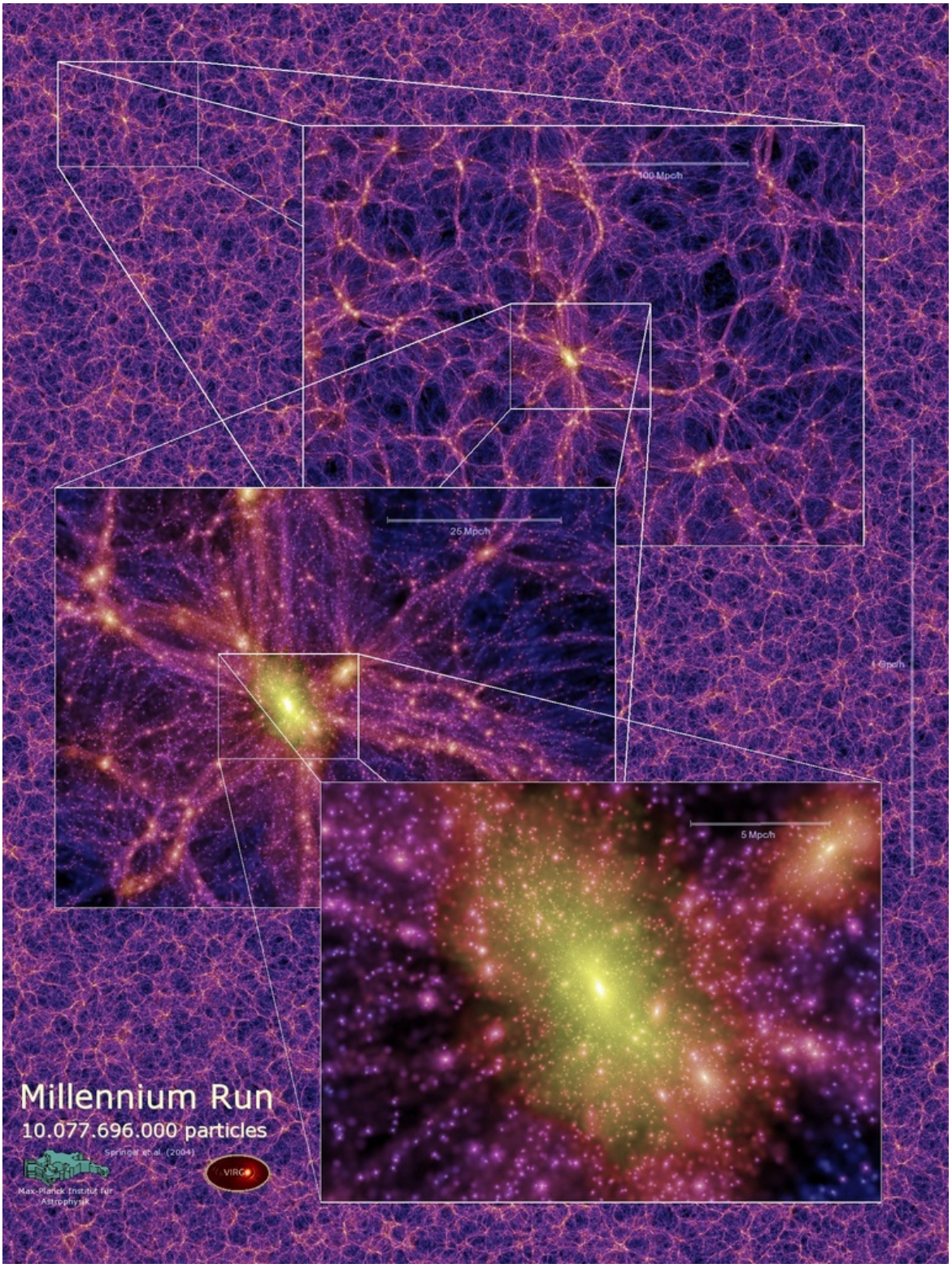

Figure 1.4: The Millennium cosmological simulation. This picture shows the dark matter density field. The overlaid panels zoom in by factors of 4 in each case, enlarging the regions indicated by the white squares. Credit: https://wwwmpa.mpa-garching.mpg.de/galform/virgo/millennium.

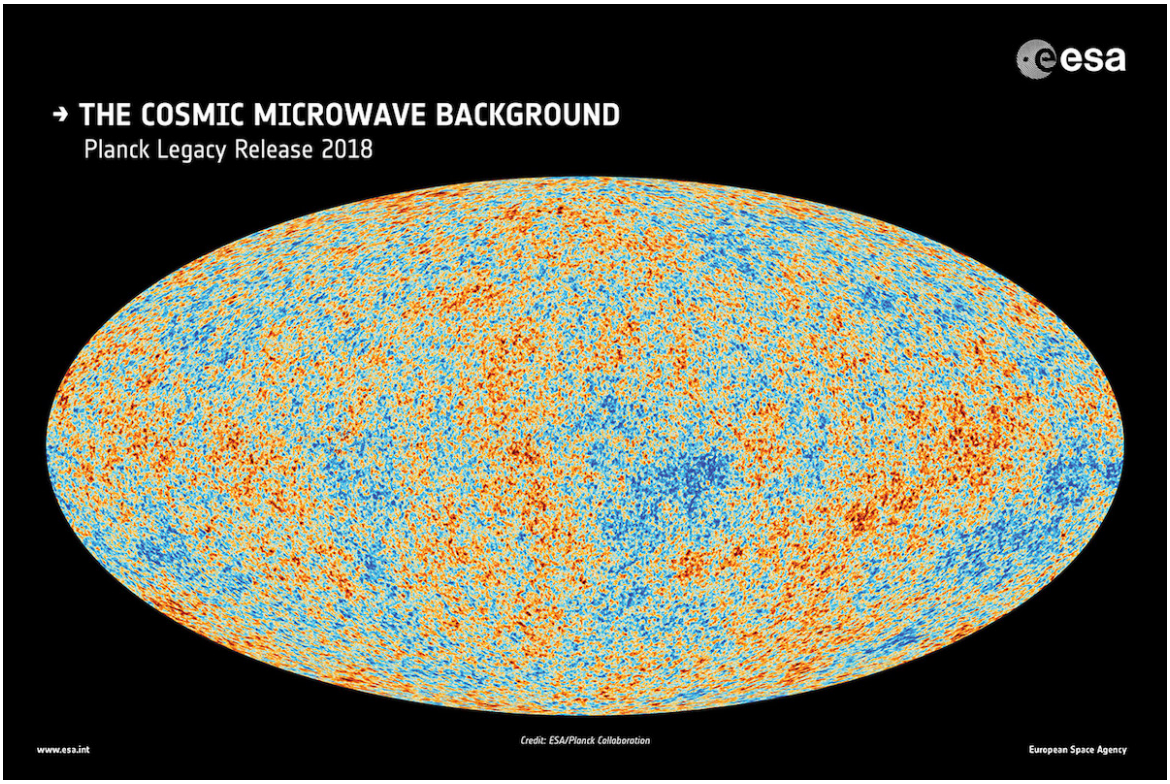

Figure 1.5: The temperature fluctuations $\Delta T/T \sim 10^{-5}$ of the cosmic microwave background as observed by European Space Agency (ESA) *Planck* mission. Credit: ESA/*Planck* Collaboration.

SDSS galaxy redshift surveys.

2009: The launch of the *Planck* mission. The latest measurements of CMB (Fig. 1.5). All current constraints on cosmological parameters are based on the results of this mission.

2015: The first detection of the gravitational waves. The crucial confirmation of GR. ★ 2017: Nobel Prize in physics for Rainer Weiss, Kip Thorne and Barry Barish.

1.2 Introduction to cosmology

Today we can confidently say that the Universe is homogeneous and isotropic on large scales. The Universe is expanding and galaxies are moving away from each other. However, neither space nor objects in this space are moving. The space itself, still being homogeneous and isotropic, is extending in size like a rubber. According to Einstein's theory of GR, the three dimensions of space and the one dimension of time form a single four-dimensional space-time continuum. To quantify the effect of the expanding, we define a scaling factor $a(t)$, which is set to be unity at the present time $a_0 = a(t_0) = 1$ (here after the index 0 denotes the current value of a parameter) and is growing with time such that $a(t_2) > a(t_1)$, where $t_2 > t_1$.

In the FLRW metric the distance (interval) in 4-dimensional space-time between two objects has the form

$$\mathrm{d}s^2 = c^2\,\mathrm{d}t^2 - a^2(t)\left[\mathrm{d}\chi^2 + f_K^2(\chi)\,\left(\mathrm{d}\theta^2 + \sin^2\theta\,\mathrm{d}\phi^2\right)\right], \tag{1.1}$$

where c is the speed of light, and (χ, θ, ϕ) are spatial spherical coordinates: χ is the radial comoving distance, θ and ϕ are the angular coordinates, and $f_K(\chi)$ is the comoving angular diameter distance, which is dependent on the curvature parameter K as

$$f_K(\chi) = \begin{cases} K^{-1/2} \sin\left(K^{1/2}\chi\right) & K > 0 \\ \chi & K = 0\,. \\ (-K)^{-1/2} \sinh\left[(-K)^{-1/2}\chi\right] & K < 0 \end{cases} \tag{1.2}$$

The expansion rate of the Universe is characterized by the Hubble parameter $H(a)$ (here after we use equivalent notations for the Hubble parameter $H(a)$ and $H(t)$, where $H(a) \equiv H(t)$)

$$H(a) = \frac{\dot{a}(t)}{a(t)}\,. \tag{1.3}$$

Conventionally, the current value of the Hubble constant H_0 is expressed in the form

$$H_0 = h\,100\,\frac{\mathrm{km}}{\mathrm{s\,Mpc}}\,, \tag{1.4}$$

where the most robust measurement value of h is 0.6766 ± 0.0042 (Table 1.1, Planck Collaboration et al. (2018)).

Similarly to the expansion of a distance between objects in the Universe, the photon wavelength increases too. If a photon was emitted at some moment t in the past with wavelength λ, then today at t_0 the same photon has a new physical wavelength λ_0 with $\lambda_0 > \lambda$,

$$\frac{\lambda_0}{\lambda} = \frac{a_0}{a(t)} = 1 + z\,, \tag{1.5}$$

where z is the cosmological redshift. The redshift can be directly measured by spectroscopy observations, and it allows the distance to objects from the observer to be inferred.

The distance $c\,\mathrm{d}t$ that light can travel in the time interval $\mathrm{d}t$ describes the comoving distance interval or comoving particle horizon as

$$\chi(a) = \int_a^1 \frac{c\,\mathrm{d}a'}{a'^2(t)H(a')}\,. \tag{1.6}$$

The expansion of the Universe is described by the Einstein equation of GR

$$R_{\mu\nu} - \frac{1}{2}g_{\mu\nu}R + g_{\mu\nu}\Lambda g_{\mu\nu} = \frac{8\pi G}{c^4}T_{\mu\nu}\,, \tag{1.7}$$

where $R_{\mu\nu}$ is the Ricci curvature tensor, $g_{\mu\nu}$ is the metric tensor, R is the scalar curvature, Λ is the cosmological constant and $T_{\mu\nu}$ is the energy-momentum tensor. Because the Universe assumed to be homogeneous, the matter content can be described as a uniform ideal fluid, characterized by its density $\rho(t)$ and pressure $p(t)$, with the equation-of-state

$$p = p\,(\rho)\,. \tag{1.8}$$

The energy-momentum tensor in this case is diagonal with components $(\rho c^2, -p, -p, -p)$. The

(00)-component (μ=0, ν=0) of the Einstein equation of GR specified to FLRW metric is the first Friedmann equation

$$\left(\frac{\dot{a}}{a}\right)^2 = \frac{8\pi G}{3}\rho - \frac{Kc^2}{a^2} + \frac{\Lambda c^2}{3}\,, \tag{1.9}$$

where G is Newton's gravitational constant. The second Friedmann equation is

$$\frac{\ddot{a}}{a} = -\frac{4\pi G}{3}\left(\rho + \frac{3p}{c^2}\right) + \frac{\Lambda c^2}{3}\,, \tag{1.10}$$

From the first law of thermodynamics for ideal fluid one can get (we also took into account that the volume of the matter depends on a scale factor)

$$\mathrm{d}(\rho c^2 a^3) = -p\,\mathrm{d}a^3\ . \tag{1.11}$$

In the differentiated form this equation became the following

$$\dot{\rho} + 3\frac{\dot{a}}{a}\left(\rho + \frac{p}{c^2}\right)\ . \tag{1.12}$$

The equations (1.8), (1.9) and (1.12) completely determine dynamics of the cosmological expansion. It should be noted that if the Universe consists of different types of matter, which do not interact with each other, the equations (1.8) and (1.12) are true for each of the matter type separately. At the same moment, ρ in equations (1.9) and (1.10) is the total matter-energy density in the Universe (here we separate cosmological constant from the total matter-energy).

Let us introduce the critical density parameter ρ_{crit}. In the case where Λ and K are equal to 0

$$\rho_{\mathrm{crit}} = \frac{3}{8\pi G}H_0^2 \approx 10^{-26}\,\mathrm{kg/m^3}\,. \tag{1.13}$$

Thus one can define all present matter densities in the way $\Omega_{i,0} = \frac{\rho_{i,0}}{\rho_{\mathrm{crit}}}$ with $\sum_i \Omega_{i,0} = 1$, where i is running over all forms of matter and energy. Now the Friedmann equation (1.9) can be rewritten in the form

$$H^2(a) = \left(\frac{\dot{a}}{a}\right)^2 = H_0^2\left(\Omega_{\mathrm{de}}(a) + \Omega_{\mathrm{m}}a^{-3} + \Omega_{\mathrm{r}}a^{-4} + \Omega_{\mathrm{K}}a^{-2}\right)\ . \tag{1.14}$$

The matter density parameter Ω_{m} consists of the dark matter Ω_{dm}, baryon Ω_{b} and neutrino Ω_ν densities; Ω_{de}, Ω_{r} and Ω_{K} are dark energy, radiation and spatial curvature densities respectively. The relation between spatial curvature density Ω_{K} and total matter-energy density Ω_0 is

$$\Omega_{\mathrm{K}} = 1 - \Omega_0\,. \tag{1.15}$$

In this way, the evolution of the Universe depends on the values of density parameters, the definition of the cosmological constant, the geometry of space-time and etc. All this information can be structured in various cosmological models. The most popular models are described in the following section.

1.3 Cold dark matter models

In modern cosmology, it is assumed that the total matter-energy content of the Universe is composed of baryonic matter, dark matter, neutrinos, radiation, dark energy and spatial curvature. According to the latest observational data, the curvature of the Universe is very close to zero, $\Omega_K = 0.0007 \pm 0.0019$ (Planck Collaboration et al., 2018). Therefore the total matter-energy density of the Universe is close to unity. This is consistent with the predictions of standard model of inflation.

The most straightforward contribution to the total matter-energy of the Universe is given by baryonic matter. This is the matter which form stars, planets, humans etc, and consist of non-relativistic (the speed of a particle is much smaller than the speed of light) particles with non-zero masses. The equation of state of baryonic matter gives $p = 0$, and therefore the density is decreasing with cosmic expansion as $\rho_b(a) \propto a^{-3}$. All components of Ω_m have the same dependence on the scaling factor. Baryons contribute about 5 per cent to the present day matter density (Table 1.1).

Neutrinos are particles that interact only via the weak nuclear force and gravity. For a long time, it was believed that neutrinos are massless. However, now the massive neutrino model consist of three species (electron neutrino ν_e, muon neutrino ν_μ, and tau neutrino ν_τ) with total mass $\sum_i m_{\nu,i} = 0.06\,\mathrm{eV}$. Today, neutrinos are non-relativistic and contribute to the total matter-energy of the Universe together with baryonic matter, although their contribution is very small. Though, in the past, neutrinos behaved as radiation and contributed to Ω_r[2]. The physics of neutrinos is still very debatable question between astrophysicists and particle physicists, see Lesgourgues et al. (2013) for example.

Another small contribution is provided by radiation $\Omega_r \lesssim 10^{-4}$, which consists mostly of photons and massless neutrinos. Radiation has a stronger dependence on the scaling factor than matter, and $\rho_r \propto a^{-4}$, where the extra a^{-1} comes from the dependence of the photon wavelength on redshift (equation 1.5). It is also important to mention, that in earlier times when the scale factor was small, the Universe was radiation dominated. This was due to the fact, that the term $\Omega_r a^{-4}$ was much bigger than $\Omega_m a^{-3}$ and $\Omega_{de}(a)$. The transition from the radiation-dominated era to the matter-dominated era occurs when $\Omega_m/a^3 = \Omega_r/a^4$, at redshift $z \approx 3110$.

The second biggest contribution to the total matter-energy budget is from the so-called dark matter. The nature of dark matter is one of the most important questions in modern cosmology. Dark matter interacts gravitationally with baryonic matter (e.g. Markevitch et al., 2006; Clowe et al., 2006; Robertson et al., 2017), and there is no evidence of electromagnetic interaction. Most likely, dark matter consist of an undiscovered elementary particle. There are three main possible types of dark matter: cold, warm and hot. These are distinguished by the size of the free streaming length of the dark matter particle (a free streaming length is an average distance travelled by a dark matter particle before it falls into a potential well). Cold dark matter has a length much smaller than the size of a protogalaxy (an object that later evolves into a dwarf galaxy), warm dark matter has a length of a similar order, and hot dark matter has a much greater length than a protogalaxy. It has been proven observationally that the structure of the Universe has a bottom-up formation. This means that galaxies formed first and galaxy clusters later. This could happen only if dark matter is cold (this was demonstrated through cosmological simulations (Davis et al., 1985)). In opposite, in a hot dark matter scenario, the top-down formation scenario would be observed, large scale structure forms first, and then galaxies[3].

[2] In Chapters 2 and 3, the radiation component is neglected, and neutrinos contribute only to the total mass Ω_m.

[3] There are also models with a combination of cold and warm dark matter, and even more exotic models, but they are not

CDM contribute ~ 26 per cent (Table 1.1) to the total matter-energy composition of the Universe and it is a fundamental component of all standard cosmological models. Thus, all cosmological models which include cold dark matter, baryons, neutrinos, and radiation with densities as in Table 1.1 can be combined in a class of CDM cosmological models.

CDM models differ in their definitions of dark energy. Presently, the origin and nature of dark energy is one of the most important and challenging questions in cosmology. This substance does not interact with any matter (at least no evidence has been found), does not clump, and is responsible for the accelerated expansion of the Universe. Moreover, dark energy constitutes about 69 per cent of the Universe and is the dominant factor in the current evolution of the Universe. The dark-energy equation of state in a general case is

$$p_{\rm de} = w(a)\, c^2 \rho_{\rm de}\,, \tag{1.16}$$

where $w(a)$ is a dimensionless parameter which may or may not be constant, depending on the model. Therefore, the evolution with the scale factor is

$$\rho_{\rm de} = \rho_{\rm de,0} \exp\left[-3 \int_1^a \frac{1 + w(a')}{a'}\, {\rm d}a'\right]\,. \tag{1.17}$$

The fact that the Universe is expanding with acceleration ($\ddot{a} > 0$) makes the constraint on the parameter $w(a)$. If we assume that all matter-energy density in equation (1.10) is dark energy (in this case there is no Λ in the right part of the equation), the constraint is the following: $w(a) < -1/3$.

Several different dark-energy model are described in the next subsections.

1.3.1 ΛCDM model

The most basic and simple model which can describe the Universe and agrees well with a variety of observational data is called the standard cosmological model or ΛCDM model.

The best candidate for dark energy is Einstein's cosmological constant Λ, where the equation of state is $p_\Lambda = -\rho_\Lambda = \text{const}$ with $w = -1$. It is also assumed that the cosmological constant is vacuum energy. Moreover, various observations show that the value of w is very close to -1 (Table 1.1).

As mentioned earlier, the early Universe was radiation-dominated, before evolving to the matter-dominated era. Recently, at redshifts $z = (2\Omega_\Lambda/\Omega_{\rm m})^{1/3} - 1 \approx 0.65$ (here, the radiation and the curvature contributions are neglected), the Universe entered the dark energy dominated era. This is why current observations show that the Universe started to expand with acceleration (it is necessary to mention, that the Universe have been always expanding, and crucial moment is the transition from decelerating to accelerating expansion).

1.3.2 *w*CDM model

The simplest extension to the ΛCDM is wCDM model, where dark energy is a quintessence (hypothetical scalar field) and w is a constant, but with a different from -1 value, $-1 < w < -1/3$[4]. The density in this case changes as $\rho_{de} \propto a^{-3(1+w)}$.

considered in this work.

[4] There is also a possibility, that dark energy is a phantom energy with the equation of state $w < -1$.

1.3.3 w_0w_aCDM model

Naturally, the next step is to add time-dependency in the dark-energy equation of state (Sahni & Starobinsky, 2006). The most popular choice is the linear model, where $w(a) = w_0 + w_a(1 - a)$ (Chevallier & Polarski, 2001; Linder, 2003). Here w_0 is the present-day value of the equation of state and w_a its rate of change. The dependence of density on the scale factor in this model is

$$\rho_{de} = \rho_{de,0} \exp\left\{-3\left[w_a(1 - a) + (1 + w_0 + w_a)\ln a\right]\right\} . \tag{1.18}$$

1.4 Modern cosmology

All cosmological models presented above would be pointless if there would be no observational evidence for them. Many of the ground, space, and flying telescopes make observations which provide constrains on cosmological parameters and models.

The CMB gives the picture of the Universe at the time of recombination (the moment when electrons and protons combined to neutral atoms and photons became free to travel in space). The picture of the CMB demonstrates the conditions which gave rise to the large scale structure of the present-day Universe. Thus, CMB measurements constrain basic cosmological parameters with high accuracy. The most resent CMB observations were carried out by the *Planck* satellite, and their data releases are of great value to modern cosmology (Planck Collaboration et al., 2014, 2016, 2018).

However, some cosmological parameters are degenerate, and so one can only measure their combination with high precision. The addition of other experiments and probes may resolve this issue. For example, the observations of type Ia supernovae are useful in constraining cosmological parameters connected to measurements of distance and the acceleration of the Universe, such as the Hubble parameter. Observations of BAO (see Section 1.6 for details) provide important information about the baryonic content.

The values with errors for the key cosmological parameters for ΛCDM, wCDM and w_0w_aCDM models obtain from the *Planck* mission are presented in Table 1.1[5].

1.5 Structure formation

The Universe is homogeneous and isotropic on very large scales. As soon as one zooms in to the scales of $\sim 200h^{-1}$Mpc, LSS became noticeable. The tiny matter fluctuations of order 10^{-5} observed in the CMB, grow over several billion years and lead to the formation of the galaxies and the LSS.

The LSS is a web-like structure which consists of overdense regions such as galaxy clusters, superclusters, sheets, walls and filaments, separated by underdense voids. It is also called 'the cosmic web'. Because dark matter cannot be observed, galaxies and clusters of galaxies are the only tracers of the matter distribution, which form knots in LSS. The cosmic web started from the tiny fluctuations in the gravitational potential, created during the time of inflation. The spatially deviating gravitational tug on the surrounding matter, accordingly guided the clustering of matter into increasing overdensities and away from regions with continuously decreasing densities – voids. Further the overdensities merged among each other. Later, these overdensities collapsed into virialised matter haloes. Then, the

[5] In Chapters 2 and 3, data from previous *Planck* release (Planck Collaboration et al., 2016) is used, as the current was not yet available at the time of writing.

Table 1.1: Cosmological parameters measured in the *Planck* survey (Planck Collaboration et al., 2018).

Description	Parameter	Value
ΛCDM model		
Physical baryon density parameter	$\Omega_{\rm b}h^2$	0.02242 ± 0.00014
Physical cold dark matter density parameter	$\Omega_{\rm cdm}h^2$	0.11933 ± 0.00091
Scalar spectral index	$n_{\rm s}$	0.9665 ± 0.0038
Hubble constant	H_0	67.66 ± 0.42
Dark energy density parameter	Ω_Λ	0.6889 ± 0.0056
Matter density parameter	$\Omega_{\rm m}$	0.3111 ± 0.0056
Equation of state of the dark energy	w	-1
Matter variance of scales of 8 Mpc/h	σ_8	0.8102 ± 0.0060
Spectral amplitude	10^9A	2.105 ± 0.030
w/w_0w_aCDM models		
Normalization of the dark-energy equation of state	w_0	-1.028 ± 0.032
Slope of the dark-energy equation of state	w_a	fixed to 0

baryonic matter formed galaxies on the fundament of dark matter haloes. The evolution of the matter distribution is a hierarchical process, where first the knots within the LSS have to form, then other structures as galaxies can form, after which massive haloes can be created. LSS can be seen by eye on the maps from surveys such as the CfA Redshift Survey (Geller & Huchra, 1989), 2dFGRS (Colless et al., 2001), SDSS (Fig. 1.6) etc.

The growth of the fluctuations by gravitational instability is a complicated non-linear process, which cannot be solved analytically. However, the small fluctuations of order 10^{-5} can be described by the linear theory.

In the expanding Universe one can use two types of coordinates: fixed coordinate $\boldsymbol{r}$ and comoving coordinate $\boldsymbol{x}$, corresponding to each other as $\boldsymbol{x} = \boldsymbol{r}/a(t)$. In the comoving frame, an object with the coordinate $\boldsymbol{x}$ is not moving. However, in the fixed frame, this object moves with the Hubble flow $\boldsymbol{v}(\boldsymbol{r},t) = H(t)\boldsymbol{r}$, where $\boldsymbol{v}(\boldsymbol{r},t) = \mathrm{d}\boldsymbol{r}/\mathrm{d}t$. The peculiar velocity is defined as $\boldsymbol{u}(\boldsymbol{r},t) = \boldsymbol{v}(\boldsymbol{r},t) - H(t)\boldsymbol{r}$. The relative density contrast is defined as

$$\delta(\boldsymbol{x},t) = \frac{\rho(\boldsymbol{x},t)}{\bar{\rho}(t)} - 1\,. \tag{1.19}$$

As mentioned before, we treat matter as a fluid with zero pressure (this works only in a matter-dominated era, but this assumption is fine for the described process). If the density contrast is small, one can linearize equations. In this case, the continuity and Euler equations in comoving coordinates are

$$\frac{\partial\delta(\boldsymbol{x},t)}{\partial t} + \frac{1}{a(t)}\boldsymbol{\nabla}_x\cdot\{[1+\delta(\boldsymbol{x},t)]\,\boldsymbol{u}(\boldsymbol{x},t)\} = 0\,, \tag{1.20}$$

$$\frac{\partial\boldsymbol{u}(\boldsymbol{x},t)}{\partial t} + \frac{\dot{a}(t)}{a(t)}\boldsymbol{u}(\boldsymbol{x},t) + \frac{1}{a(t)}\left[\boldsymbol{u}(\boldsymbol{x},t)\cdot\boldsymbol{\nabla}_x\right]\boldsymbol{u}(\boldsymbol{x},t) = -\frac{1}{a(t)}\boldsymbol{\nabla}_x\Phi(\boldsymbol{x},t)\,. \tag{1.21}$$

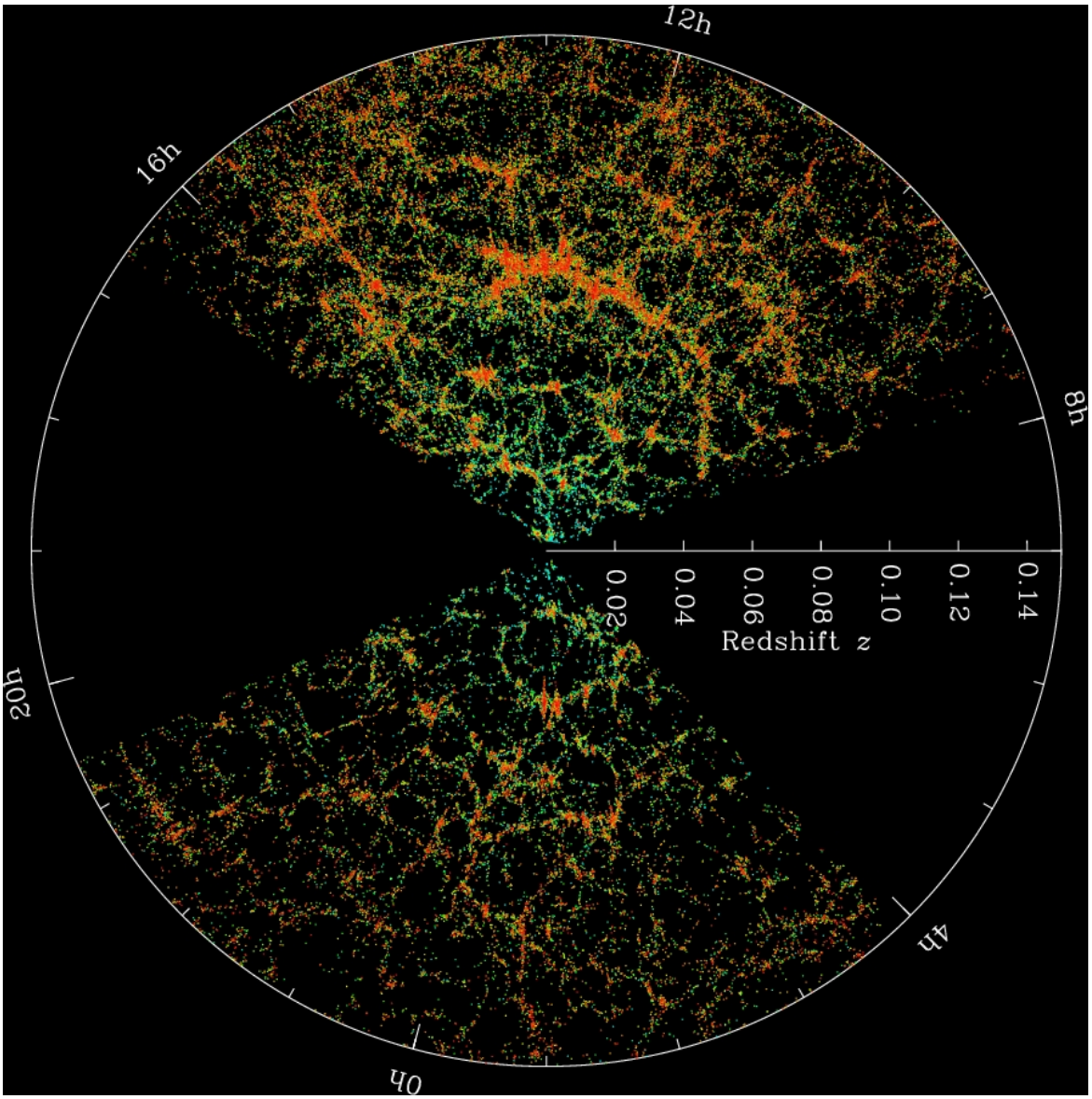

Figure 1.6: The LSS of the Universe observed by the SDSS. Each dot is a galaxy, where red points are galaxies with more red star light, indicating older galaxies. The cosmic web structure can be seen by eye. Credit: M. Blanton and SDSS www.sdss.org.

The Poisson equation is

$$\nabla_x^2 \Phi(\boldsymbol{x}, t) = \frac{3H_0^2 \Omega_\mathrm{m}}{2a(t)} \delta(\boldsymbol{x}, t)\,, \tag{1.22}$$

which relates the gravitational potential $\Phi(\boldsymbol{x}, t)$ and the density contrast $\delta(\boldsymbol{x}, t)$ in the expanding Universe.

These equations form the set of partial differential non-linear equations which can not be solved analytically. One option is to solve the set with some assumptions, e.g. using the linear approximation. This method will be described in the following Section 1.6. Another variant is to solve the set numerically, including non-linear effects. This will be discussed in Section 1.7.

1.6 Linear evolution

In the early Universe, according to CMB observations, density perturbations have been small $\delta(\boldsymbol{x}, t) \ll 1$. If one assumes the same for the peculiar velocity $|\boldsymbol{u}(\boldsymbol{x}, t)|/c \ll 1$ and for the gravitational potential $\Phi(\boldsymbol{x}, t)/c^2 \ll 1$, one can neglect any term of second order such as $\delta^2(\boldsymbol{x}, t)$, $u^2(\boldsymbol{x}, t)$ or $\delta(\boldsymbol{x}, t)\boldsymbol{u}(\boldsymbol{x}, t)$, and rewrite equations (1.20, 1.21) for linear case

$$\frac{\partial \delta(\boldsymbol{x}, t)}{\partial t} + \frac{1}{a(t)} \boldsymbol{\nabla}_x \cdot \boldsymbol{u}(\boldsymbol{x}, t) = 0\,, \tag{1.23}$$

$$\frac{\partial \boldsymbol{u}(\boldsymbol{x}, t)}{\partial t} + \frac{\dot{a}(t)}{a(t)} \boldsymbol{u}(\boldsymbol{x}, t) = -\frac{1}{a(t)} \boldsymbol{\nabla}_x \Phi(\boldsymbol{x}, t)\,. \tag{1.24}$$

The Poisson equation (1.22) is already linear. We now can combine all three equations (1.23, 1.24 and 1.22) together by taking the time derivative of equation (1.23) and the divergence of equation (1.24). As a result one gets

$$\frac{\partial^2 \delta(\boldsymbol{x}, t)}{\partial t^2} + 2H(t) \frac{\partial \delta(\boldsymbol{x}, t)}{\partial t} - \frac{3H_0^2 \Omega_\mathrm{m}}{2a^3(t)} \delta(\boldsymbol{x}, t) = 0\,. \tag{1.25}$$

This equation does not contain $\boldsymbol{x}$ or derivatives of $\boldsymbol{x}$. Thus this is ordinary second-order differential equation, which can be solved as

$$\delta(\boldsymbol{x}, t) = D_+(t) \Delta_+(\boldsymbol{x}) + D_-(t) \Delta_-(\boldsymbol{x})\,, \tag{1.26}$$

where $D_+(t)$ and $D_-(t)$ are two linearly independent solutions of

$$\ddot{D}(t) + \frac{2\dot{a}(t)}{a(t)} \dot{D}(t) - \frac{3H_0^2 \Omega_\mathrm{m}}{2a^3(t)} D(t) = 0\,, \tag{1.27}$$

and $D_+(t)$ grows with time, while $D_-(t)$ decreases. For the ΛCDM case the linear growth factor describing the time evolution of growing perturbations is

$$D_+(a) = \frac{5\Omega_\mathrm{m}}{2} \frac{H(a)}{H_0} \int_0^a \frac{\mathrm{d}a'}{\left[\Omega_\mathrm{m}/a' + \Omega_\Lambda a'^2 + \Omega_\mathrm{r}/a'^2 + (\Omega_0 - 1)\right]^{3/2}}\,. \tag{1.28}$$

Usually, the growth factor is normalized to unity at the time of today $D(a_0) = 1$. Now we can derive the evolution of velocity perturbations using equations (1.23) and (1.26). Again, we are interested in

growing mode only, so $\dot{\delta} = \left(\dot{D}(t)_+/D(t)_+\right)\delta$. The divergence of the velocity field is

$$\boldsymbol{\nabla}_x \cdot \boldsymbol{u}(\boldsymbol{x},t) = -a(t)\frac{\dot{D}_+(t)}{D_+(t)}\delta = -a\dot{a}\frac{1}{D_+(a)}\frac{\mathrm{d}D_+(a)}{\mathrm{d}a}\delta = -aH(a)f(a)\delta\,, \tag{1.29}$$

where $f(a)$ is the growth-of-structure parameter, defined as

$$f(a) = \frac{\mathrm{d}\ln D_+(a)}{\mathrm{d}\ln a} \approx \Omega_\mathrm{m}^{0.55}. \tag{1.30}$$

Strictly speaking, the solutions above are true only for the Universe in a matter-dominated era and within the GR formalism. But for the scale smaller than the Hubble radius $d_H = c/aH(a)$ one can use Newtonian gravity, without GR effects. For the radiation and matter-dominated eras the Hubble radius is different from the comoving radius/horizon by a factor of order unity.

The growth of the perturbations depends on their length-scale and on which era the Universe is in. On scales larger than the horizon (superhorizon scale) perturbations are always allowed to grow during both radiation and matter-dominated eras. However, the growth of fluctuations with length smaller than the horizon was prevented during the radiation-dominated era. In this case, the perturbations which enter the horizon during the radiation-dominated era (with wavevector k), will be suppressed later, compare with perturbations that entered during the matter-dominated era (with wavevector k_s). The transfer function T_k describes the ratio of fluctuation amplitudes for different wavevectors today, normalized with respect to the initial density perturbations at a_i

$$\frac{\delta(k,a_0)}{\delta(k_\mathrm{s},a_0)} = T_k\frac{\delta(k,a_i)}{\delta(k_\mathrm{s},a_i)}\,. \tag{1.31}$$

For the universe consisting only of CDM, a fitting formula (Bardeen et al., 1986) is

$$T_k = \frac{\ln(1+2.34q)}{2.34q}\left[1+3.89q+(16.1q)^2+(5.46q)^3+(6.71q)^4\right]^{-1/4}\,, \tag{1.32}$$

where $q = k/\Omega_\mathrm{m}h^2\mathrm{Mpc}^{-1}$. For a ΛCDM universe the transfer function should be calculated numerically, for example with the CAMB (Code for Anisotropies in the Microwave Background) code (https://camb.info, Lewis et al., 2000; Howlett et al., 2012), see examples in Fig. 1.7.

The linear matter power spectrum describes the growth of structures on the different perturbation scales as

$$P_L(k,a) = Ak^{n_\mathrm{s}}T^2(k)D_+^2(a)\,, \tag{1.33}$$

where n_s is the power spectrum index, A is the amplitude of the initial perturbations. Instead of the amplitude A one can use the standard deviation $\sigma(r)$ of the matter distribution within sphere of radius of $r = 8h^{-1}\mathrm{Mpc}$, where $\sigma_8 \equiv \sigma(r = 8h^{-1}\mathrm{Mpc})$. It can be calculated as the integral over the power spectrum

$$\sigma^2(r,a) = \int_0^\infty \frac{\mathrm{d}^3k}{(2\pi)^3}P_L(k,a)\,|W_r(k)|^2\,, \tag{1.34}$$

where $W_r(k)$ is the window function (smoothing kernel) over scales of radius r. The window function is defined as

$$W_r(k) = 3\frac{\sin(kr)-kr\cos(kr)}{(kr)^3}\,. \tag{1.35}$$

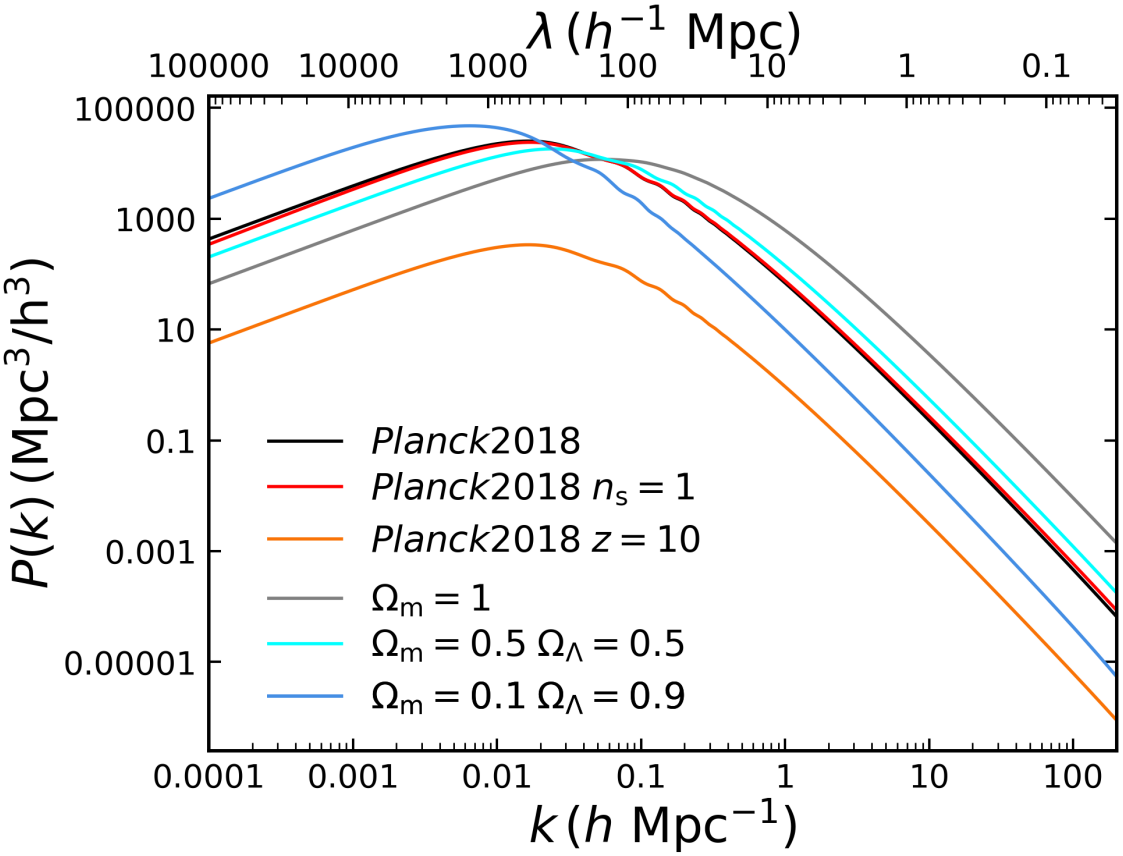

Figure 1.7: The power spectrum computed for different cosmological models by CAMB. The default model is the ΛCDM cosmology with *Planck* 2018 data. The rest of the models are the modifications of the default: ΛCDM with Harrison-Zel'dovich spectrum, default ΛCDM at the higher redshift, variations of the matter component fraction in the Universe. For all cases we assume flat cosmology.

The function of σ_8 plays an important role in cosmology and its constrain is given in Table 1.1.

In the Harrison-Zel'dovich theory (Harrison, 1970; Peebles & Yu, 1970; Zeldovich, 1972) the slope of the spectrum of initial perturbations, n_s, is unity, which gives a flat (it does not depend on scale k) power spectrum. Observations of the CMB found that the value of the slope of the spectrum is very close, but not exactly unity, $n_s = 0.9665 \pm 0.0038$ (Table 1.1). This is one of the main evidence for the need for an inflation model in the history of the Universe. In various inflationary scenarios the value of the slope of the spectrum of initial perturbations can be slightly different.

Before the recombination, the initial fluctuations drive acoustic waves in the baryon-photon fluid with the speed approaching the speed of light. Both the photons and the baryons moved outward together. Then, at the recombination era, photons became free to travel without interactions and continued to stream away and became almost completely uniform. On opposite, the baryons lost their motive pressure and remained in overdensities. Later, baryons and dark matter eventually settle into each other's potentials, creating the BAO visible as wriggles in the power spectrum on scales smaller than the horizon (see on scales of $\sim 100\,h^{-1}$Mpc in Fig.1.7). That is why BAO provide important cosmological information.

1.7 Non-linear evolution

The analytic solutions become inaccurate as soon as density perturbations become non-linear. One possibility is to use higher-order terms in perturbation series to approximate fluctuations on next orders. However, this method is also limited and stops being accurate as soon as fluctuations are about unity $\delta \sim 1$. Another variant is to use cosmological simulations, where equations are solved numerically with fewer approximations. Usually, simulations are computationally expensive and they can take months when running on supercomputers. Nevertheless, simulations are the best option currently to perform non-linear structure formation.

However, one specific case of non-linear density evolution still can be solved analytically – the evolution of a spherical mass overdensity. Firstly, we consider a region smaller than the horizon to use Newtonian gravity. Next, one consider the sphere of mass M with the radius $r(t)$ which starts to collapse at a time t_i. The spherical collapse can be described as

$$\frac{\mathrm{d}^2 r}{\mathrm{d}t^2} = H_0^2 \Omega_\Lambda r(t) - \frac{GM}{r^2(t)} \,. \tag{1.36}$$

The enclosed fluctuations δ grow initially as predicted by linear theory as $\delta_\mathrm{L} = \delta_i D(t)/D(t_i)$ (here after we use $D(t) \equiv D_+(t)$). As soon as δ grows above δ_L, the system collapses to a point and the overdensity predicted by linear theory is $\delta_\mathrm{L} = 1.686$. In the Einstein-de Sitter (EdS) universe[6] the sphere collapse at redshift z if its linear overdensity extrapolated to the present day is

$$\delta_\mathrm{L}(z) = \frac{1.686}{D(z)} \,. \tag{1.37}$$

These collapsed matter overdensities are the seeds for the matter haloes which will be part of the LSS. The halo mass function is a mass distribution of dark matter halos within a certain mass range depending on their mass and redshifts. The general form of the halo mass function is the following

$$\frac{\mathrm{d}n}{\mathrm{d}M}\,(M, z) = \frac{\bar{\rho}_{m,0}}{M} \left(-\frac{\mathrm{d}\ln\sigma}{\mathrm{d}M} \right) f(\sigma) \,, \tag{1.38}$$

where $\bar{\rho}_{\mathrm{m},0} = \Omega_\mathrm{m} \rho_{\mathrm{crit},0}$ is the mean matter density today. Press & Schechter first developed in 1974 the simple analytic model (Press & Schechter, 1974) with

$$f(\sigma) = \sqrt{\frac{2}{\pi}} \frac{\delta_\mathrm{L}}{\sigma} \exp\left(-\frac{\delta_\mathrm{L}^2}{2\sigma^2} \right) . \tag{1.39}$$

Nowadays there are plenty of models which match with simulations much better than Press-Schechter mass function.

1.7.1 Standard Perturbation Theory

Now we will consider the non-linear evolution of density and velocity fields in equations (1.20) and (1.21). It is convenient to work with these equations in a different notation. Firstly, we replace the cosmic

[6] EdS universe consist only from matter $\Omega_\mathrm{m} = 1$, Ω_Λ and Ω_K are assumed to be zero.

time t with the conformal time τ and the Hubble function $H(t)$ with the conformal expansion rate $\mathcal{H}(\tau)$, where $\mathrm{d}t = a(\tau)\,\mathrm{d}\tau$ and $\mathcal{H}(\tau) \equiv \mathrm{d}\ln a(\tau)\,/\mathrm{d}\tau = H(t)a(t)$ respectively. Secondly, one can replace the divergence of the velocity field with the function $\theta(\boldsymbol{x},\tau) \equiv \boldsymbol{\nabla}\cdot\boldsymbol{u}(\boldsymbol{x},\tau) = \boldsymbol{\nabla}\cdot[\boldsymbol{v}(\boldsymbol{x},\tau) - \mathcal{H}(\tau)\boldsymbol{x}]$. Now we can rewrite equations (1.20) and (1.21) as

$$\frac{\partial\delta(\boldsymbol{x},\tau)}{\partial\tau} + \boldsymbol{\nabla}\cdot\{[1+\delta(\boldsymbol{x},\tau)]\,\boldsymbol{u}(\boldsymbol{x},\tau)\} = 0\,, \tag{1.40}$$

$$\frac{\partial\boldsymbol{u}(\boldsymbol{x},\tau)}{\partial\tau} + \mathcal{H}(\tau)\boldsymbol{u}(\boldsymbol{x},\tau) + \boldsymbol{u}(\boldsymbol{x},\tau)\boldsymbol{\nabla}\cdot\boldsymbol{u}(\boldsymbol{x},\tau) = \boldsymbol{\nabla}\Phi(\boldsymbol{x},\tau)\,. \tag{1.41}$$

Compared to Section 1.6, now we will go further than the first order terms in perturbation series and use Standard Perturbation Theory (SPT). The density and velocity are expanded about the linear solutions and the variances of the linear fluctuations are assumed to be small. In this case, the density and velocity fields can be written as

$$\delta(\boldsymbol{x},t) = \sum_{n=1}^{\infty}\delta^{(n)}(\boldsymbol{x},t)\,, \tag{1.42}$$

$$\theta(\boldsymbol{x},t) = \sum_{n=1}^{\infty}\theta^{(n)}(\boldsymbol{x},t)\,, \tag{1.43}$$

where $\delta^{(1)}$ and $\theta^{(1)}$ are the linear (first order) perturbations, $\delta^{(2)}$ and $\theta^{(2)}$ are second-order perturbations etc. It is more convenient to work in Fourier space where we adopt the transformation in the form of

$$\tilde{f}(\boldsymbol{k},\tau) = \int f(\boldsymbol{x},\tau)\,e^{-i\boldsymbol{k}\cdot\boldsymbol{x}}\,\mathrm{d}^3x\,, \tag{1.44}$$

and the inverse transform is

$$f(\boldsymbol{x},\tau) = \int \tilde{f}(\boldsymbol{k},\tau)\,e^{i\boldsymbol{k}\cdot\boldsymbol{x}}\,\frac{\mathrm{d}^3k}{(2\pi)^3}\,. \tag{1.45}$$

Taking into account non-linear terms and Fourier transforming equations (1.40) and (1.41) we get

$$\frac{\partial\tilde{\delta}(\boldsymbol{k},\tau)}{\partial\tau} + \tilde{\theta}(\boldsymbol{k},\tau) = -\frac{1}{(2\pi)^3}\int \mathrm{d}^3\boldsymbol{k}_1\;\mathrm{d}^3\boldsymbol{k}_2\,\delta_D(\boldsymbol{k}-\boldsymbol{k}_{12})\alpha(\boldsymbol{k}_1,\boldsymbol{k}_2)\tilde{\theta}(\boldsymbol{k}_1,\tau)\tilde{\delta}(\boldsymbol{k}_2,\tau)\,, \tag{1.46}$$

$$\frac{\partial\tilde{\theta}(\boldsymbol{k},\tau)}{\partial\tau} + \mathcal{H}(\tau)\,\tilde{\theta}(\boldsymbol{k},\tau) + \frac{3}{2}\Omega_{\mathrm{m}}\mathcal{H}^2(\tau)\tilde{\delta}(\boldsymbol{k},\tau) = -\frac{1}{(2\pi)^3}\int \mathrm{d}^3\boldsymbol{k}_1\,\mathrm{d}^3\boldsymbol{k}_2\,\delta_D(\boldsymbol{k}-\boldsymbol{k}_{12})\times \\ \times\beta(\boldsymbol{k}_1,\boldsymbol{k}_2)\tilde{\theta}(\boldsymbol{k}_1,\tau)\tilde{\theta}(\boldsymbol{k}_2,\tau)\,, \tag{1.47}$$

where δ_D denotes the three-dimensional Dirac delta distribution, and $\boldsymbol{k}_1 + \boldsymbol{k}_2 = \boldsymbol{k}_{12}$. The functions

$$\alpha(\boldsymbol{k}_1,\boldsymbol{k}_2) \equiv \frac{\boldsymbol{k}_{12}\cdot\boldsymbol{k}_1}{k_1^2}\,, \tag{1.48}$$

$$\beta(\boldsymbol{k}_1,\boldsymbol{k}_2) \equiv \frac{k_{12}^2(\boldsymbol{k}_1\cdot\boldsymbol{k}_2)}{2k_1^2k_2^2}\,, \tag{1.49}$$

represent the non-linearity the mode coupling. The fluctuations can be expressed as

$$\tilde{\delta}(\boldsymbol{k},\tau) = \sum_{n=1}^{\infty} \int \frac{\mathrm{d}^3\boldsymbol{q}_1}{(2\pi)^3} \dots \frac{\mathrm{d}^3\boldsymbol{q}_n}{(2\pi)^3} (2\pi)^3 \delta_D(\boldsymbol{k} - \boldsymbol{q}_{1\dots n}) F_n(\boldsymbol{q}_1,\dots,\boldsymbol{q}_n,\tau) \tilde{\delta}_1(\boldsymbol{q}_1,\tau)\dots\tilde{\delta}_1(\boldsymbol{q}_n,\tau)\,, \tag{1.50}$$

$$\tilde{\theta}(\boldsymbol{k},\tau) = -f(\tau)\mathcal{H}(\tau) \sum_{n=1}^{\infty} \int \frac{\mathrm{d}^3\boldsymbol{q}_1}{(2\pi)^3} \dots \frac{\mathrm{d}^3\boldsymbol{q}_n}{(2\pi)^3} (2\pi)^3 \delta_D(\boldsymbol{k} - \boldsymbol{q}_{1\dots n}) G_n(\boldsymbol{q}_1,\dots,\boldsymbol{q}_n,\tau) \times$$
$$\times \tilde{\delta}_1(\boldsymbol{q}_1,\tau)\dots\tilde{\delta}_1(\boldsymbol{q}_n,\tau)\,, \tag{1.51}$$

where F_n and G_n are homogeneous functions of the wave vectors $\{\boldsymbol{q}_1,\dots,\boldsymbol{q}_n\}$ with degree zero. They are constructed from the fundamental mode coupling functions $\alpha(\boldsymbol{k}_1,\boldsymbol{k}_2)$ and $\beta(\boldsymbol{k}_1,\boldsymbol{k}_2)$. In the general case they are defined as

$$\begin{aligned} F_n(\boldsymbol{q}_1,\dots,\boldsymbol{q}_n) &= \sum_{m=1}^{n-1} \frac{G_m(\boldsymbol{q}_1,\dots,\boldsymbol{q}_m)}{(2n+3)(n-1)} \Big[(2n+1)\alpha(\boldsymbol{k}_1,\boldsymbol{k}_2) F_{n-m}(\boldsymbol{q}_{m+1},\dots,\boldsymbol{q}_n) + \\ &\quad + 2\beta(\boldsymbol{k}_1,\boldsymbol{k}_2) G_{n-m}(\boldsymbol{q}_{m+1},\dots,\boldsymbol{q}_n) \Big]\,, \end{aligned} \tag{1.52}$$

$$\begin{aligned} G_n(\boldsymbol{q}_1,\dots,\boldsymbol{q}_n) &= \sum_{m=1}^{n-1} \frac{G_m(\boldsymbol{q}_1,\dots,\boldsymbol{q}_m)}{(2n+3)(n-1)} \Big[3\alpha(\boldsymbol{k}_1,\boldsymbol{k}_2) F_{n-m}(\boldsymbol{q}_{m+1},\dots,\boldsymbol{q}_n) + \\ &\quad + 2n\beta(\boldsymbol{k}_1,\boldsymbol{k}_2) G_{n-m}(\boldsymbol{q}_{m+1},\dots,\boldsymbol{q}_n) \Big]\,, \end{aligned} \tag{1.53}$$

where $\boldsymbol{k}_1 \equiv \boldsymbol{q}_1 + \dots + \boldsymbol{q}_m$, $\boldsymbol{k}_2 \equiv \boldsymbol{q}_{m+1} + \dots + \boldsymbol{q}_n$, $\boldsymbol{k} \equiv \boldsymbol{k}_1 + \boldsymbol{k}_2$, and $F_1 = G_1 \equiv 1$. In a particular case of EdS universe, for $n = 2$ we have:

$$F_2(\boldsymbol{q}_1,\boldsymbol{q}_2) = \frac{5}{7} + \frac{1}{2}\frac{\boldsymbol{q}_1\cdot\boldsymbol{q}_2}{q_1 q_2}\left(\frac{q_1}{q_2} + \frac{q_2}{q_1}\right) + \frac{2}{7}\frac{(\boldsymbol{q}_1\cdot\boldsymbol{q}_2)^2}{q_1^2 q_2^2}\,, \tag{1.54}$$

$$G_2(\boldsymbol{q}_1,\boldsymbol{q}_2) = \frac{3}{7} + \frac{1}{2}\frac{\boldsymbol{q}_1\cdot\boldsymbol{q}_2}{q_1 q_2}\left(\frac{q_1}{q_2} + \frac{q_2}{q_1}\right) + \frac{4}{7}\frac{(\boldsymbol{q}_1\cdot\boldsymbol{q}_2)^2}{q_1^2 q_2^2}\,. \tag{1.55}$$

1.7.2 Bias

We already know how a dark matter halo is formed. Then baryons fell down into a gravitational potential well of a dark matter halo and formed a galaxy. Thus galaxies have to be located within the dark matter haloes. In this case the distribution of galaxies has to follow the dark-matter-halo distribution, predicted by cosmological simulations. In other words, if one put the map of the survey on top of the map predicted by simulations (see Fig. 1.8), they should be identical. However, these distributions are not the same. This difference is called dark matter haloes bias (Desjacques et al., 2018).

The general concept of galaxy bias was formed in the 1980s. The analysis of redshift surveys showed that the galaxy positions form a structure, and that areas with higher density are more likely to

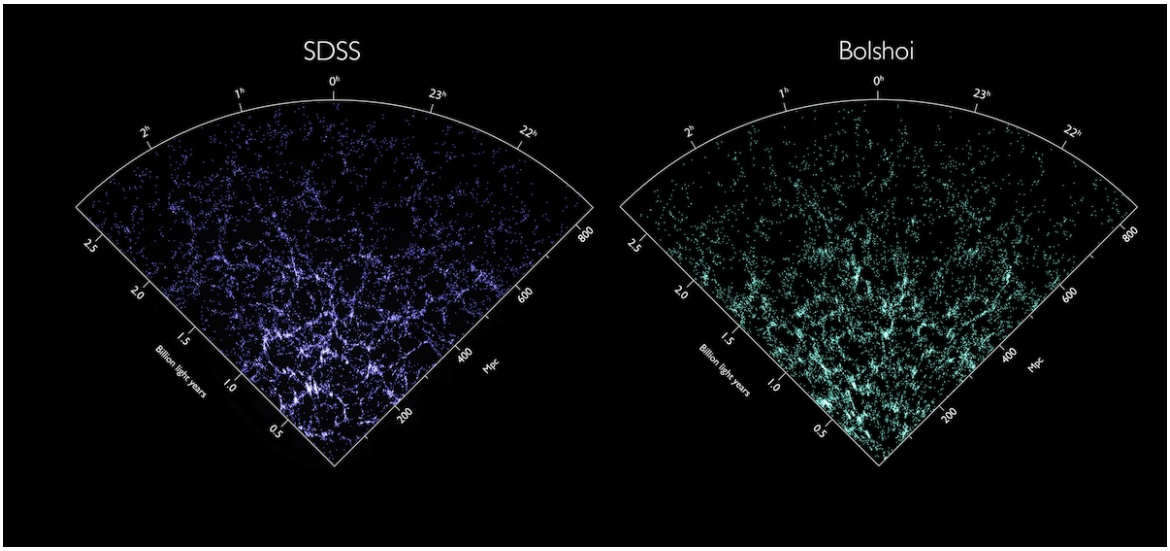

Figure 1.8: The maps of the galaxy distribution observed by SDSS and predicted by the Bolshoi Simulation. Credit: Nina McCurdy and Joel Primack (University of California, Santa Cruz), Ralf Kaehler and Risa Wechsler (Stanford University), Michael Busha (University of Zurich), SDSS www.sdss.org, Bolshoi simulation http://hipacc.ucsc.edu/Bolshoi/index.html.

host more haloes than less-density regions (Huchra et al., 1983; Kirshner et al., 1981). The explanation was found in 1984 by Nick Kaiser (Kaiser, 1987). He demonstrated that the high-density regions of a Gaussian random field are more strongly correlated than the field itself. In simple words, galaxies are forming in overdense regions, as soon as the gravitational potential is larger, more galaxies can be formed in this area.

If one uses again the linear assumption of $|\delta| \ll 1$ (here this works for large volumes), the relation between the galaxy and the mass density contrast is

$$\delta_{\mathrm{g}}(\boldsymbol{x}, t) = \sum_{O} b_O(t) O(\boldsymbol{x}, t)\,, \tag{1.56}$$

where δ_{g} is galaxies density contrast, $O(\boldsymbol{x}, t)$ is an operator, or statistical field, which describes properties of the galaxies' environment on which their density can depend, and $b_O(t)$ is a corresponding bias parameter (Fry & Gaztanaga, 1993; Desjacques et al., 2018). The simplest model, also know as 'local bias expansion', has operators which are power-law of the density contrast, $O = \delta^N$, $N \geq 1$. In this case, the corresponding bias parameters are $b_N = N! \delta_{\mathrm{g}^N}$. Study of N-body simulations shows that the haloes tend to assemble faster in high-density regions (White et al., 1987). Therefore, the linear bias assumption works well only on very large scale. If one zooms-in to smaller scales, it is necessary to extend the bias expansion at least up to second order:

$$\delta_{\mathrm{g}}(\boldsymbol{x}) = b_1\, \delta(\boldsymbol{x}) + \frac{b_2}{2}\left[\delta^2(\boldsymbol{x}) - \langle \delta^2(\boldsymbol{x})\rangle\right] + \frac{b_{s^2}}{2}\left[s^2(\boldsymbol{x}) - \langle s^2(\boldsymbol{x})\rangle\right]\,, \tag{1.57}$$

where b_2 and b_{s^2} are the Eulerian non-linear and non-local (tidal) bias (Catelan et al., 1998). The traceless tidal field has Cartesian components $s_{ij}(\boldsymbol{x}) = (\partial_i \partial_j - \delta_{ij}\, \nabla^2/3)\, \phi(\boldsymbol{x})$, where Kronecker

symbol δ_{ij} and the gravitational potential $\phi(\boldsymbol{x})$ satisfies the Poisson equation $\nabla^2\phi = \delta$. The tidal field represents the stretching or compressing of the matter field due to a gradient of the gravitational force. Tidal biases different from zero have been found in the analysis of cosmological simulations (Baldauf et al., 2012; Chan et al., 2012; Saito et al., 2014; Bel et al., 2015).

The issue of the galaxy bias is still one of the hottest topic today. There are many models of galaxy bias, which partially agree and disagree with real observations and cosmological simulations (for more details see McDonald & Roy (2009); Assassi et al. (2014); Desjacques et al. (2018)).

1.8 Statistics

In Sections 1.6, 1.7 and 1.7.1 we described the evolution of density fluctuations with time. However, we do not know their initial conditions at earlier times t_i. Unfortunately, no theories exist to predict the function $\delta(\boldsymbol{x}, t_i)$. Also, there is no way to have direct observations of the primordial fluctuations. Even with the available observations, we see only the partial evolution of different systems at different times. But one can predict the statistical properties of the initial fluctuation field. If at some fixed time the fluctuations will be considered as a realizations of a random field, we can describe their evolution later on. A random field is characterized by the probability that a specific realization $\delta(\boldsymbol{x})$ of the density fluctuations occurs. Let us assume that $\delta(\boldsymbol{x})$ can be described at sufficient accuracy on a regular grid of spatial coordinates $\boldsymbol{x}$, where $\delta(\boldsymbol{x}_i)$ are the values of the density contrast at $\boldsymbol{x}_i$. The realization of the random field is described by the set of $\delta(\boldsymbol{x}_i)$, and the random field is characterized by the joint probability distribution

$$p\left[\delta(\boldsymbol{x}_1), \ldots, \delta(\boldsymbol{x}_n)\right] \mathrm{d}\delta(\boldsymbol{x}_1) \ldots \mathrm{d}\delta(\boldsymbol{x}_n) \,, \tag{1.58}$$

where $\delta(\boldsymbol{x}_i)$ lies within $\mathrm{d}\delta(\boldsymbol{x}_i)$ of $\delta(\boldsymbol{x}_i)$. Consequently, the description of a random fields is basically a joint probability distribution function (PDF) of discrete random variables. The n^{th}-moment of a random field is defined as

$$\langle \delta(\boldsymbol{x}_1) \ldots \delta(\boldsymbol{x}_n) \rangle = \int \mathrm{d}\delta(\boldsymbol{x}_1) \ldots \mathrm{d}\delta(\boldsymbol{x}_n)\, p\left[\delta(\boldsymbol{x}_1), \ldots, \delta(\boldsymbol{x}_n)\right] \delta(\boldsymbol{x}_1) \ldots \delta(\boldsymbol{x}_n) \,, \tag{1.59}$$

where $\langle \delta(\boldsymbol{x}_1) \ldots \delta(\boldsymbol{x}_n) \rangle$ is the ensemble average over the whole set of realizations. The first moment is the mean. The n^{th}-moment of a random field can be decomposed into connected and disconnected parts. The n-point correlation function is defined as connected part of the joint ensemble average of the product of n fields and has a form of

$$\begin{aligned} \langle \delta(\boldsymbol{x}_1) \ldots \delta(\boldsymbol{x}_n) \rangle_{\mathrm{c}} \equiv \langle \delta(\boldsymbol{x}_1) \ldots \delta(\boldsymbol{x}_n) \rangle - \langle \delta(\boldsymbol{x}_1) \rangle_{\mathrm{c}} \langle \delta(\boldsymbol{x}_2) \rangle_{\mathrm{c}} \ldots \langle \delta(\boldsymbol{x}_n) \rangle_{\mathrm{c}} - \\ - \langle \delta(\boldsymbol{x}_1) \rangle_{\mathrm{c}} \langle \delta(\boldsymbol{x}_2) \ldots \delta(\boldsymbol{x}_n) \rangle_{\mathrm{c}} + \text{cycl.} - \langle \delta(\boldsymbol{x}_1) \delta(\boldsymbol{x}_2) \rangle_{\mathrm{c}} \langle \delta(\boldsymbol{x}_3) \ldots \delta(\boldsymbol{x}_n) \rangle_{\mathrm{c}} + \text{cycl.} - \ldots \\ - \langle \delta(\boldsymbol{x}_1) \ldots \delta(\boldsymbol{x}_{n-1}) \rangle_{\mathrm{c}} \langle \delta(\boldsymbol{x}_n) \rangle_{\mathrm{c}} + \text{cycl.} \,, \end{aligned} \tag{1.60}$$

where $\langle \delta(\boldsymbol{x}_1) \rangle_{\mathrm{c}} \equiv \langle \delta(\boldsymbol{x}_1) \rangle = 0$.

The density field should reflect the fact that the Universe is homogeneous and isotropic. This is true if all grid points are translated and rotated in the same way, $\boldsymbol{x} \to \mathcal{R}(\boldsymbol{x} + \boldsymbol{y})$, where $\mathcal{R}$ is a rotation matrix and $\boldsymbol{y}$ is a translation vector, the probability density p remains unchanged.

1.8.1 Two-point correlation function

The two-point correlation function is defined as the joint ensemble average of the density at two different locations

$$\langle \delta(\boldsymbol{x})\delta(\boldsymbol{x}+\boldsymbol{r})\rangle = \xi(r)\,, \tag{1.61}$$

which depends only on the distance r between the two points due to statistical homogeneity and isotropy. We adopt the same Fourier transform as in equations (1.44) and (1.45), and now $\delta(\boldsymbol{k})$ is a complex random variable. As $\delta(\boldsymbol{x})$ is real, it follows that

$$\delta(\boldsymbol{k}) = \delta^*(-\boldsymbol{k})\,. \tag{1.62}$$

The density field is determined by the statistical properties of the random variable $\delta(\boldsymbol{k})$. The two-point correlation function in Fourier space is

$$\begin{aligned}\langle \tilde{\delta}(\boldsymbol{k})\tilde{\delta}(\boldsymbol{k}')\rangle &= (2\pi)^3 \int \mathrm{d}^3\boldsymbol{x}\,\mathrm{d}^3\boldsymbol{r}\,\xi(r)e^{-i(\boldsymbol{k}+\boldsymbol{k}')\cdot\boldsymbol{x}-i\boldsymbol{k}'\cdot\boldsymbol{r}} = \\ &= (2\pi)^3\delta_D(\boldsymbol{k}+\boldsymbol{k}') \int \mathrm{d}^3\boldsymbol{r}\,\xi(r)e^{i\boldsymbol{k}\cdot\boldsymbol{r}} = (2\pi)^3\delta_D(\boldsymbol{k}+\boldsymbol{k}')P(k)\,,\end{aligned} \tag{1.63}$$

where $P(k)$ is the density power spectrum and $k = |\boldsymbol{k}|$. The inverse relation between the two-point correlation function and power spectrum is

$$\xi(r) = \int \frac{\mathrm{d}^3\boldsymbol{k}}{(2\pi)^3}P(k)e^{i\boldsymbol{k}\cdot\boldsymbol{r}}\,. \tag{1.64}$$

Therefore, the power spectrum and the two-point correlation function are Fourier transform pairs.

1.8.2 Gaussian random fields

The power spectrum is well-defined for almost all homogeneous random fields. However, this concept is extremely useful if a random field is Gaussian (Bardeen et al., 1986). In this case any joint probability distribution $p\,[\delta(\boldsymbol{x}_1),\ldots,\delta(\boldsymbol{x}_n)]$ of local densities $\delta(\boldsymbol{x}_i)$ follows the Gaussian distribution. A Gaussian random field has the following properties: the Fourier components $\tilde{\delta}(\boldsymbol{k})$ are mutually statistically independent, the probability density for $\tilde{\delta}(\boldsymbol{k})$ is described by Gaussian, and the joint probability distribution of a number of n of linear combinations of the random variables $\delta(\boldsymbol{x}_i)$ is a multivariate Gaussian. The Wick's theorem says that any ensemble average of products of variables can be calculated as a product of ensemble averages of pairs

$$\langle \tilde{\delta}(\boldsymbol{k}_1)\ldots\tilde{\delta}(\boldsymbol{k}_{2n+1})\rangle = 0\,, \tag{1.65}$$

$$\langle \tilde{\delta}(\boldsymbol{k}_1)\ldots\tilde{\delta}(\boldsymbol{k}_{2n})\rangle = \sum_{\text{all pair associations}}\ \prod_{n\,\text{pairs}(i,j)} \langle \tilde{\delta}(\boldsymbol{k}_i)\tilde{\delta}(\boldsymbol{k}_j)\rangle\,. \tag{1.66}$$

The correlator is vanishing for an odd number of variables, but for the even number it is fully specified by the power spectrum

$$\langle \tilde{\delta}(\boldsymbol{k}_1)\ldots\tilde{\delta}(\boldsymbol{k}_{2n})\rangle = \sum_{\text{all pair associations}}\ \prod_{n\,\text{pairs}(i,j)} (2\pi)^3P(k_i)\delta_D(\boldsymbol{k}_i+\boldsymbol{k}_j)\,. \tag{1.67}$$

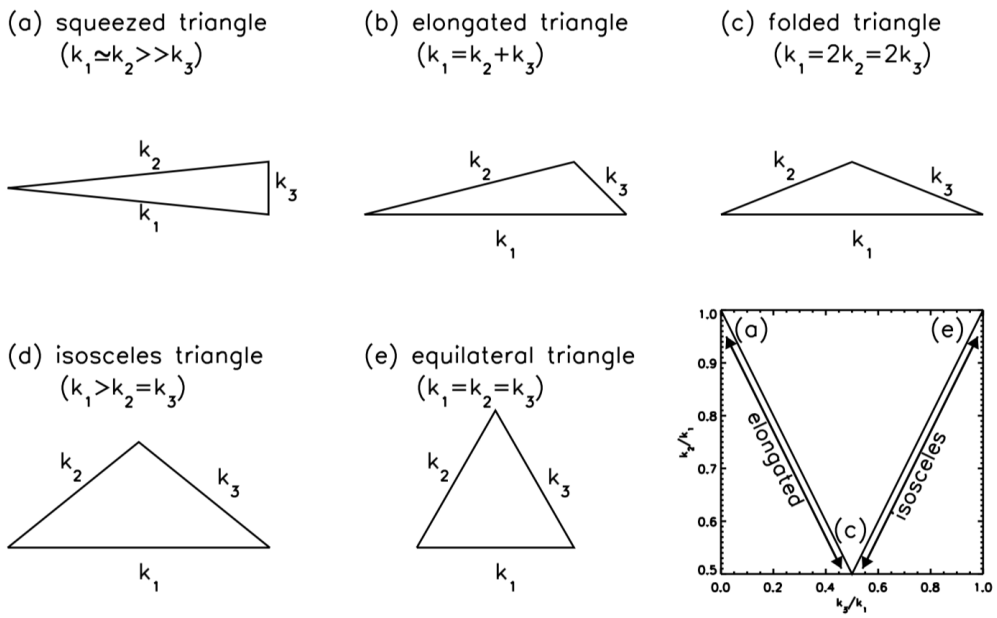

Figure 1.9: Different triangular configurations of the bispectrum satisfying the condition $k_1 \geq k_2 \geq k_3$. Credit: Jeong & Komatsu (2009)

Therefore, the n-point correlation function can be presented as

$$\langle \tilde{\delta}(\boldsymbol{k}_1) \dots \tilde{\delta}(\boldsymbol{k}_n) \rangle = (2\pi)^3 P_n(k_1, \dots, k_n) \delta_D(\boldsymbol{k}_1 + \dots + \boldsymbol{k}_n) \,. \tag{1.68}$$

1.8.3 Three-point correlation function

The bispectrum is the three-point correlation function defined as

$$\langle \tilde{\delta}(\boldsymbol{k}_1) \tilde{\delta}(\boldsymbol{k}_2) \tilde{\delta}(\boldsymbol{k}_3) \rangle = (2\pi)^3 B(\boldsymbol{k}_1, \boldsymbol{k}_2, \boldsymbol{k}_3) \delta_D(\boldsymbol{k}_1 + \boldsymbol{k}_2 + \boldsymbol{k}_3) \,. \tag{1.69}$$

The bispectrum is defined only for closed triangles of wavevectors, where $\boldsymbol{k}_1 + \boldsymbol{k}_2 + \boldsymbol{k}_3 = 0$. Hence, the bispectrum is a function of two independent vectors. Different triangular configurations of the bispectrum are shown in Fig. 1.9.

1.8.4 Redshift-space distortions

We assume that the density field is statistically homogeneous and isotropic and the correlation function $\xi(\boldsymbol{r})$ depends only on the separation $|\boldsymbol{r}|$. Also, the power spectrum depends only on $|\boldsymbol{k}|$, but not on the direction of the $\boldsymbol{k}$-vector. We do not observe the true position of a galaxy. We observe its angular position θ and its redshift. The measured redshift z is a superposition of the cosmic expansion and the peculiar velocity $\boldsymbol{u}$ of an object. Therefore, the line-of-sight coordinate is different in real ($\boldsymbol{r}$) and redshift ($\boldsymbol{s}$) space, $s_3 = r_3 + u_3/H_0$ (here we align 3$^{\rm rd}$ axis with line-of-sight $\boldsymbol{s}$), while two

other coordinates are the same in both spaces. This effect is called the redshift-space distortions (RSD). The effects of RSD are presented in Fig. 1.10 (Hamilton, 1998). Here one can see what will happen with galaxies (dots) falling down towards a spherical overdensity with some peculiar velocities (arrows). At large scales, the peculiar velocity of an infalling shell is small compared to its radius, and the shell appears squashed. At smaller scales, not only is the radius of a shell smaller, but also its peculiar infall velocity tends to be larger. The shell that is just at turnaround, its peculiar velocity just cancelling the general Hubble expansion, appears collapsed to a single velocity in redshift space. At yet smaller scales, shells that are collapsing in proper coordinates appear inside out in redshift space. The combination of collapsing shells with previously collapsed, virialized shells, gives rise to finger-of-God effect. Finger-of-God is well-known features of redshift surveys (Fig.1.10).

Let us introduce the number density of galaxies, $n(\boldsymbol{r})$ and $n(\boldsymbol{s})$, the mean galaxy density, $\bar{n}(\boldsymbol{r})$ and $\bar{n}(\boldsymbol{s})$, and fractional galaxy density contrast, $\delta_{\rm g}(\boldsymbol{r})$ and $\delta^s_{\rm g}(\boldsymbol{s})$, in real and redshift space respectively. For galaxy number density is true that

$$\begin{aligned} n(\boldsymbol{r}) &= \bar{n}(\boldsymbol{r})\left[1+\delta_{\rm g}(\boldsymbol{r})\right] , \\ n(\boldsymbol{s}) &= \bar{n}(\boldsymbol{s})\left[1+\delta^s_{\rm g}(\boldsymbol{s})\right] . \end{aligned} \tag{1.70}$$

Because of the number of galaxies is conserved value

$$\bar{n}(\boldsymbol{r})\left[1+\delta_{\rm g}(\boldsymbol{r})\right]{\rm d}^3\boldsymbol{r} = \bar{n}(\boldsymbol{s})\left[1+\delta^s_{\rm g}(\boldsymbol{s})\right]{\rm d}^3\boldsymbol{s} , \tag{1.71}$$

therefore

$$\delta^s_{\rm g}(\boldsymbol{s}) = \frac{1+\delta_{\rm g}(\boldsymbol{r})}{{\rm d}s_3\,/{\rm d}r_3} - 1 . \tag{1.72}$$

Taking into account the connection between real and redshift space coordinates and using only linear terms, one gets the following

$$\delta^s_{\rm g}\boldsymbol{r} = \delta_{\rm g}(\boldsymbol{r}) - \frac{1}{H_0}\frac{{\rm d}u_3}{{\rm d}r_3} . \tag{1.73}$$

If we present the peculiar velocity as the gradient of a potential

$$\boldsymbol{u}(\boldsymbol{r}) = \boldsymbol{\nabla}_r\psi(\boldsymbol{r}) , \tag{1.74}$$

and taking into consideration equations (1.29) and (1.30), we obtain the following

$$\boldsymbol{\nabla}^2_r\psi = \frac{1}{a^2(t)}\boldsymbol{\nabla}^2_x\psi \approx -H_0 f\delta . \tag{1.75}$$

The Fourier transform of this equation is

$$\tilde{\psi}(\boldsymbol{k}) = \frac{H_0 f}{k^2}\tilde{\delta}(\boldsymbol{k}) . \tag{1.76}$$

The line-of-sight component of the peculiar velocity in the Fourier space can be expressed as

$$\tilde{u}_3(\boldsymbol{k}) = -\frac{ik_3}{k}H_0 f\tilde{\delta}(\boldsymbol{k}) . \tag{1.77}$$

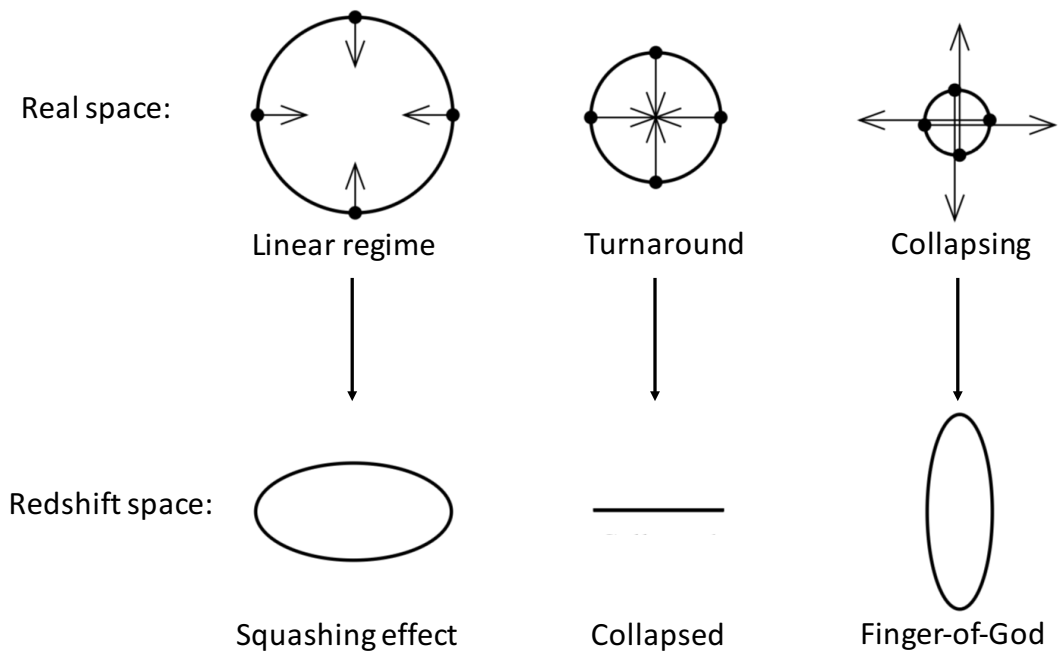

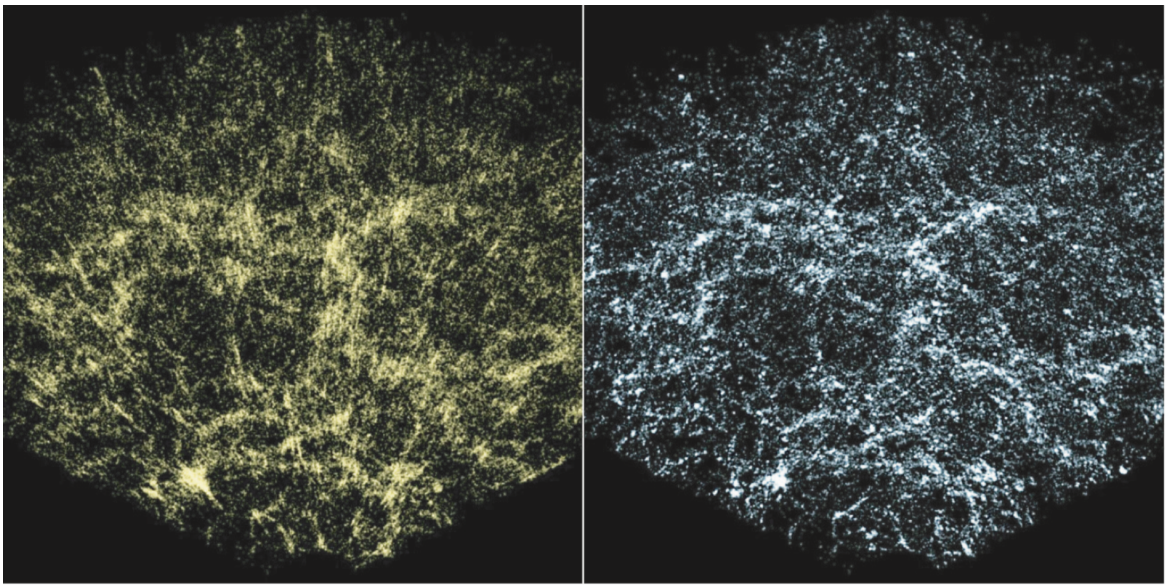

Figure 1.10: RSD caused by peculiar velocities. Top panel: The dots are 'galaxies' and the arrows represent their peculiar velocities. Depending on the relative locations of galaxies and peculiar velocities, the effect of RSD is different. Credit: Hamilton (1998). Bottom panel: The SDSS galaxy distribution before (left) and after (right) finger-of-God compression. Credit: Subba Rao et al. (2008).

Now, if one takes the Fourier transform of equation (1.73)

$$\tilde{\delta}_{\mathrm{g}}^{s}(\boldsymbol{k}) = \tilde{\delta}_{\mathrm{g}}(\boldsymbol{k}) + \frac{ik_3}{H_0}\tilde{u}_3(\boldsymbol{k})\,, \tag{1.78}$$

and combines with equation (1.77), then gets the following

$$\tilde{\delta}_{\mathrm{g}}^{s}(\boldsymbol{k}) = \left[1 + \beta\mu^2(\boldsymbol{k})\right]\tilde{\delta}_{\mathrm{g}}(\boldsymbol{k})\,, \tag{1.79}$$

where $\beta = \Omega_{\mathrm{m}}^{0.55}/b_1$ (we are working here with linear terms only) and $\mu(\boldsymbol{k}) = \boldsymbol{k}\cdot\hat{\boldsymbol{s}}/k$ is the cosine between $\boldsymbol{k}$-vector and line-of-sight $\boldsymbol{s}$. It is necessary to mention, that it is the density contrast δ of the matter which rules the peculiar velocity, not the galaxies density contrast $\delta_{\mathrm{g}} = b_1\delta$.

Finally, we can derive how RSD affects the galaxy power spectrum in linear theory:

$$P(\boldsymbol{k}) = Z_1^2(\boldsymbol{k})P_L(k)\,, \tag{1.80}$$

where $Z_1(\boldsymbol{k}) = b_1 + f\mu^2$.

In tree level SPT, the bispectrum can be expressed as multiplications of the power spectrum. Including the RSD effect one gets the following

$$B(\boldsymbol{k}_1, \boldsymbol{k}_2, \boldsymbol{k}_3) = 2\left[Z_2(\boldsymbol{k}_1, \boldsymbol{k}_2)Z_1(\boldsymbol{k}_1)Z_1(\boldsymbol{k}_2)P_L(k_1)P_L(k_2) + \text{cycl.}\right]\,, \tag{1.81}$$

where the cyclic permutations runs over pairs of $\boldsymbol{k}_1$, $\boldsymbol{k}_2$ and $\boldsymbol{k}_3$. The second order kernel is

$$Z_2(\boldsymbol{k}_i, \boldsymbol{k}_j) = \frac{b_2}{2} + b_1F_2(\boldsymbol{k}_i, \boldsymbol{k}_j) + f\mu_{ij}^2G_2(\boldsymbol{k}_i, \boldsymbol{k}_j) + \frac{f\mu_{ij}k_{ij}}{2}\left[\frac{\mu_i}{k_i}Z_1(\boldsymbol{k}_j) + \frac{\mu_j}{k_j}Z_1(\boldsymbol{k}_i)\right] + \\ + \frac{b_{s^2}}{2}S_2(\boldsymbol{k}_i, \boldsymbol{k}_j)\,. \tag{1.82}$$

The second-order kernels are the same as in equations (1.54) and (1.55), and $\boldsymbol{k}_{ij} = \boldsymbol{k}_i + \boldsymbol{k}_j$, and $\mu_{ij} = \boldsymbol{k}_{ij}\cdot\hat{\boldsymbol{s}}/k_{ij}$. The tidal kernel is

$$S_2(\boldsymbol{k}_i, \boldsymbol{k}_j) = \left(\frac{\boldsymbol{k}_i\cdot\boldsymbol{k}_j}{k_ik_j}\right)^2 - \frac{1}{3}\,. \tag{1.83}$$

1.9 Fisher-matrix formalism

Since ancient times observations have been the driving force of astronomy and astrophysics. This has not changed. At the beginning, observations were made using only the naked eye. Nowadays, we have modern telescopes which are extremely expensive, and can make incredibly good observations even in ranges inaccessible to the human eye. But still many astrophysical questions do not have clear answers. On the one hand, more telescopes and satellites are needed for investigating the mysteries of the Universe, and the technology is available to construct them. On the other hand, there is no way to build all requested instruments. Nowadays, it is not enough just to mention what should be observed. All new missions have to follow certain goals. Scientific groups have to present very detailed plans of how astrophysics will benefit from a new telescope or satellite, and how one question or another will be clarified. Therefore, it is necessary to demonstrate the power of the potential future mission.

Basically, one has to show that a telescope with characteristics A, B and C will measure the parameters D and E with accuracy F and G. Moreover, if a scientific group would like to measure some parameters with a certain accuracy, scientists can make a request regarding mission specifications. To know how well parameters can be measured, scientists do a forecast. There are several ways to make such kind of forecast. The most popular and widely used is the Fisher matrix technique. This technique helps to forecast the precision of a future mission while it is still in the design phase.

1.9.1 Likelihood function

In this work we follow Bayesian statistics (Heavens, 2009; March, 2013), since we can observe only one universe. In Bayesian statistics only the data is real and known and the model has to be estimated from this data. In this case, the probability is a measure of the degree of belief. Let us assume, that there is an observed value x_i, based on a model with some parameters $\Theta = \theta_1, \theta_2, \ldots, \theta_M$. Some model parameter values are more believable than others, depending on how well they reproduce the data and on the prior knowledge on these parameters. In this way, the probability with which the data is reproduced by the parameter set Θ defines the degree of belief of these model parameters. This belief is described by the posterior probability distribution $P(\Theta|\boldsymbol{x})$. The Bayes' theorem is

$$P(\Theta|\boldsymbol{x}) = \frac{P(\Theta)}{P(\boldsymbol{x})}\mathcal{L}(\boldsymbol{x}|\Theta)\,, \tag{1.84}$$

where $P(\Theta)$ is the prior information about our parameters and $P(\boldsymbol{x})$ is the evidence. The likelihood function $\mathcal{L}(\boldsymbol{x}|\Theta)$ expresses the probability to obtain the observations $\boldsymbol{x}$ given a defined set of model parameter values Θ.

In case of Gaussian-distributed and independent data, the likelihood has the following form

$$\mathcal{L}(\boldsymbol{x}|\Theta) = \prod_i \frac{1}{\sqrt{2\pi\sigma_i^2}} \exp\left[-\frac{(x_i-\mu_i)^2}{2\sigma_i^2}\right], \tag{1.85}$$

where σ_i^2 is the variance in the observed data point x_i, μ_i is the expected value given the model parameters Θ. In order to obtain the best fit between observations and model parameters, the χ^2-value has to be minimised, where

$$\chi^2 = \sum_i \left(\frac{(x_i-\mu_i)}{\sigma_i}\right)^2 . \tag{1.86}$$

This method is called the maximul likelihood estimation.

1.9.2 Fisher matrix and error covariance matrix

The Fisher formalism is a way of measuring the amount of information about an unknown parameter that can be extracted from the set of observable known parameters. In other words, the Fisher information can tell how accurately it is possible to estimate model parameters from a given data set. The statistician Ronald Fisher developed this method in 1935 (Fisher, 1935) and since that time it has been widely used in astrophysics (e.g Bunn, 1995; Vogeley & Szalay, 1996; Tegmark et al., 1997; Heavens, 2009; March, 2013; Euclid Collaboration et al., 2019).

In a general case, the Fisher matrix is defined as the expectation value of the second derivatives of the logarithmic likelihood function (the Hessian matrix) at its maximum, averaged over the data realizations:

$$F_{\alpha\beta} = -\left\langle \frac{\partial^2 \ln \mathcal{L}(\theta)}{\partial\theta_\alpha \partial\theta_\beta}\bigg|_{\max} \right\rangle , \tag{1.87}$$

where α and β label the parameters of interest θ_α and θ_β. The approximation with Taylor expansion around the maximum likelihood is

$$\ln \mathcal{L}(p) \approx \ln \mathcal{L}_{\max} - \frac{1}{2}\sum_{\alpha\beta} \frac{\partial^2 \ln \mathcal{L}(\theta)}{\partial\theta_\alpha \partial\theta_\beta}\bigg|_{\max} (\theta_\alpha - \theta_\alpha^{\max})(\theta_\beta - \theta_\beta^{\max}) , \tag{1.88}$$

where $\mathcal{L}_{\max}$ is the maximum likelihood and $\theta_{\alpha,\beta}^{\max}$ are the values of $\theta_{\alpha,\beta}$ which maximize the likelihood. For data with Gaussian errors, the Fisher matrix has an analytic expression that depends only on the expected mean and covariance of the data

$$F_{\alpha\beta} = \frac{1}{2}\,\mathrm{tr}\left[\frac{\partial \mathbf{C}}{\partial\theta_\alpha}\mathbf{C}^{-1}\frac{\partial \mathbf{C}}{\partial\theta_\beta}\mathbf{C}^{-1}\right] + \sum_{ij}\frac{\partial\mu_i}{\partial\theta_\alpha}(\mathbf{C}^{-1})_{ij}\frac{\partial\mu_j}{\partial\theta_\beta} , \tag{1.89}$$

where $\boldsymbol{\mu}$ is the mean of the data vector $\boldsymbol{x}$ and $\mathbf{C} = \langle(\boldsymbol{x}-\boldsymbol{\mu})(\boldsymbol{x}-\boldsymbol{\mu})^T\rangle$ is the expected covariance of the data. The trace and sum over α or β represent summations over the variables in the data vector. For Gaussian distributed data $\langle \boldsymbol{x}\rangle = \mu$. The inverse of the Fisher matrix provides the full error covariance matrix of the parameters of interests $\theta_{\alpha\beta}$

$$\mathrm{Cov}_{\alpha\beta} = \left(F^{-1}\right)_{\alpha\beta} . \tag{1.90}$$

The diagonal elements of the error covariance matrix are the marginalised errors of the parameters $\theta_{\alpha,\beta}$. For instance, the expected marginalised 1σ error of parameter θ_α is

$$\sigma_\alpha^{\mathrm{marg}} = \sqrt{\mathrm{Cov}_{\alpha\alpha}} . \tag{1.91}$$

When we quoting uncertainties on parameter θ_α, the other parameters (e.g. θ_β, θ_ν) have automatically been marginalized over. That means their probabilities have been integrated over: these parameters have been set free to hold any values while we calculate the range of acceptable value of θ_α. Conversely, the unmarginalised expected error is just the square root of the diagonal element of the Fisher matrix with the same index as parameter

$$\sigma_\beta^{\mathrm{unmarg}} = \frac{1}{\sqrt{F_{\beta\beta}}} . \tag{1.92}$$

The Cramer-Rao theorem states that for any unbiased estimator of a model parameter $\theta_{\alpha,\beta}$ the measurement error can not be smaller than the inverse of the Fisher matrix (the errors obtain from equation 1.92). The non-diagonal element e.g. $\mathrm{Cov}_{\alpha\beta} = \rho_{\alpha\beta}\sigma_\alpha\sigma_\beta$ shows the correlation between the errors of the parameters θ_α and θ_β. The parameters can be absolutely independent $\rho_{\alpha\beta} = 0$, partially correlated $0 < \rho_{\alpha\beta} < 1$ and completely correlated $\rho_{\alpha\beta} = 1$.

Marginalization over all parameters is equivalent to the full Fisher matrix inversion as in equation 1.90. However, it may be that one desires to omit 'nuisance' parameters in the final errors. In this case,

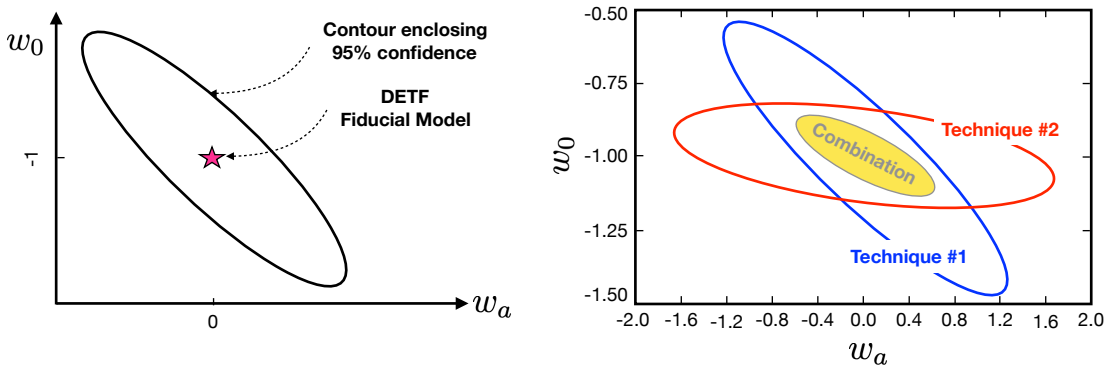

Figure 1.11: The implementation of the Fisher matrix and the figure of merit by the Dark Energy Task Force (DETF). Left panel: The DETF figure of merit is defined as the reciprocal of the area of the error ellipse in the $w_0 - w_a$ plane that encloses the 95% confidence level contour. Right panel: Illustration of the power of combining techniques. Technique #1 and Technique #2 have roughly equal DETF figure of merit. When results are combined, the DETF figure of merit is substantially improved. Credit: Albrecht et al. (2006).

the first step is to invert original Fisher matrix $F_{\alpha\beta}$ to $\mathrm{Cov}_{\alpha\beta}$. The second step is to remove the rows and columns corresponding to the parameters that are to be marginalise-out. Finally, the smaller covariance matrix $\widetilde{\mathrm{Cov}}_{\alpha\beta}$ is inverted and the result will be new smaller Fisher matrix $\widetilde{F}_{\alpha\beta}$, which is marginalised over the selected parameters.

It is also possible to make a combined constraint from multiple experiments (Albrecht et al., 2006; Coe, 2009). One can just sum the Fisher matrices in a proper way: for the same parameters, rows and columns are summed, and for the different parameters extra rows and columns are added. For example, the combination of two Fisher matrices $F_{\alpha\beta\nu}$ and $F'_{\alpha\beta\eta}$ is

$$\begin{bmatrix} F_{\alpha\alpha} & F_{\alpha\beta} & F_{\alpha\nu} \\ F_{\beta\alpha} & F_{\beta\beta} & F_{\beta\nu} \\ F_{\nu\alpha} & F_{\nu\beta} & F_{\nu\nu} \end{bmatrix} + \begin{bmatrix} F'_{\alpha\alpha} & F'_{\alpha\beta} & F'_{\alpha\eta} \\ F'_{\beta\alpha} & F'_{\beta\beta} & F'_{\beta\eta} \\ F'_{\eta\alpha} & F'_{\eta\beta} & F'_{\eta\eta} \end{bmatrix} = \begin{bmatrix} F_{\alpha\alpha} + F'_{\alpha\alpha} & F_{\alpha\beta} + F'_{\alpha\beta} & F_{\alpha\nu} & F'_{\alpha\eta} \\ F_{\beta\alpha} + F'_{\beta\alpha} & F_{\beta\beta} + F'_{\beta\beta} & F_{\beta\nu} & F'_{\beta\eta} \\ F_{\nu\alpha} & F_{\nu\beta} & F_{\nu\nu} & \\ F'_{\eta\alpha} & F'_{\eta\beta} & F'_{\eta\eta} & \end{bmatrix}. \tag{1.93}$$

The marginalization should be performed after the sum. The new marginalized errors are smaller compare to the individual experiments, for instance see Fig. 1.11.

If the Fisher matrix is defined for one set of parameters $\theta_{\alpha\beta}$, it can be recalculated for the another set θ_{ij}. In this case the new Fisher matrix S_{ij} is defined as

$$S_{ij} = \frac{\partial p_\alpha}{\partial \theta_i} F_{\alpha\beta} \frac{\partial p_\beta}{\partial \theta_j}, \tag{1.94}$$

where $\partial p_\alpha / \partial \theta_i$ are the Jacobian matrices which relate the old and new sets of parameters.

In astrophysics, a popular implementation of the Fisher matrix is in providing an error ellipse (contour plot, see Fig. 1.11). It shows how well two parameters can be measured together. The ellipse's

shape parameters are defined as

$$a^2 = \frac{\sigma_\alpha^2 + \sigma_\beta^2}{2} + \sqrt{\frac{\left(\sigma_\alpha^2 - \sigma_\beta^2\right)^2}{4} + \sigma_{\alpha\beta}^2}\,, \tag{1.95}$$

$$b^2 = \frac{\sigma_\alpha^2 + \sigma_\beta^2}{2} - \sqrt{\frac{\left(\sigma_\alpha^2 - \sigma_\beta^2\right)^2}{4} + \sigma_{\alpha\beta}^2}\,, \tag{1.96}$$

$$\tan 2\theta = \frac{2\sigma_{\alpha\beta}}{\sigma_\alpha^2 - \sigma_\beta^2}\,. \tag{1.97}$$

The semi-major and semi-minor axes a and b then need to be multiplied by a coefficient $\alpha_{\mathrm{C.L.}}$ (where $\alpha_{\mathrm{C.L.}} = \sqrt{\Delta\chi^2}$) depending on the confidence level (C.L.) we are interested in. For 68.3% C.L. (1σ), $\Delta\chi^2 \approx 2.3$ and $\alpha_{\mathrm{C.L.}} \approx 1.52$. For 95.4% C.L. ($2\sigma$), $\Delta\chi^2 \approx 6.17$ and $\alpha_{\mathrm{C.L.}} \approx 2.48$.

The Fisher matrix analysis is a straightforward and easily-implemented method. Due to this distinct advantage it is widely used. However, it is necessary to work very carefully with the Fisher matrix itself. If the matrix contains many degenerate parameters, the inversion operation may not be stable. In this case, any small changes in any element of $F_{\alpha\beta}$ may cause dramatic changes in the final errors. Therefore, the parameters $\theta_{\alpha\beta}$ have to be chosen carefully.

1.9.3 Figure of merit

The square root of a diagonal element of covariance matrix provides one-dimensional error, so it is useful if one needs to know how well a specific parameter can be measured. However, for many cosmological parameters, their one-dimensional errors are correlated. Therefore, the product of these errors may not give the true value of the measurement of these parameters together. Thus, to know how well the experiment can constrain two or more parameters together it is convenient to use a figure of merit (FoM) (Albrecht et al., 2006; Wang, 2008; Mortonson et al., 2010). The definition of the FoM is

$$\mathrm{FoM}_{\alpha\beta} = \frac{1}{\mathcal{A}\sqrt{\det \mathrm{Cov}_{\alpha\beta}}}\,, \tag{1.98}$$

where the coefficient $\mathcal{A}$ depends on C.L. in the definition. Larger FoM indicates greater accuracy. The FoM as a quantity to constrain dark energy became widely used after the DETF report (Albrecht et al., 2006) (see Fig. 1.11). Currently, this is one of the most important targets of proposals for future missions to study cosmology.

1.10 Galaxy clustering with the *Euclid* mission

Galaxy clustering is a cosmological probe which helps to measure many cosmological parameters. Following the idea that structure formation initiated from a homogeneous and isotropic density field, also the correlation function is expected to be isotropic. Respectively, studying the distribution of large samples of galaxies allows to reconstruct this correlation function and thus the underlying cosmology dependence (e.g. Laureijs (2009); Giannantonio et al. (2012)).

The previous sections introduce various cosmological models and expansion history of the Universe, the power spectrum, the bispectrum, RSD, galaxy bias, etc. To measure all of these features, one needs to have a specific survey, which covers a large sky area and redshift range. In this section, we describe a promising instrument for such observations - the *Euclid*[7] satellite (Laureijs, 2009; Pozzetti et al., 2016; Amendola et al., 2018; Euclid Collaboration et al., 2019). The main goal of *Euclid* is to understand the physical origin of the accelerated expansion of the Universe. The mission will explore the history of the Universe and the evolution of cosmic structures by measuring shapes and redshifts of galaxies over a large fraction of the sky. *Euclid* plans to image a billion galaxies, and measure nearly 30 million galaxy redshifts.

This new probe is expected to improve the constraint on the dark-energy equation of state by a factor of more than 300 for FoM($w_0 w_a$) compared to previous studies (Laureijs, 2009). The details of the future mission are summarised in the following sections.

1.10.1 The *Euclid* mission and instrument specifications

Euclid is a medium-class mission of the ESA Cosmic Vision 2015-2025 programme. The satellite will be launched by a Soyuz ST-2.1b rocket with a Fregat-MT space tug from the Kourou spaceport and transferred to the Lagrange point L2 of the Sun-Earth System. The satellite is scheduled to launch in 2022, and the planned mission lifetime is 6 years. The *Euclid* survey will cover 15000 deg^2 of the sky in a redshift range $z \sim 0.9 - 1.8$.

Euclid consists of a 1.2 meter Korsch telescope with a silicon carbide mirror, and three imaging and spectroscopic instruments working in the visible (VIS) and the near-infrared (NISP) wavelength ranges. The NISP contains a slitless spectrometer and a three bands photometer. The VIS and the NISP have a common field-of-view of 0.53 deg^2.

The VIS works in the wavelength range from 500 to 900 nm in the R+I+Z bands, has a pixel resolution of 0.1 arcseconds, and consists of 6 × 6 Charged Coupled Devices. *Euclid* will make high resolution images of billion galaxies, to measure the shapes of galaxies and to obtain the gravitational lensing effects on distant background galaxies. As a main goal, the dark matter distribution and its changes over the last 10 billion years will be reconstructed.

The NISP photometer consists of 16 HgCdTe near infra-red detectors working in the Y, J, and H bands with 0.3 arcsecond pixel resolution. The wavelength range of the instrument is between 900 and 2000 nm. The near infrared photometry data will be combined with the VIS data to derive photometric redshifts and rough estimates of distances of galaxies observed by the VIS. The near infrared spectrometer will measure redshifts for ∼ 30 million galaxies, their distances, and their 3-dimensional position in the Universe. These data will be used to describe the distribution and clustering of galaxies and their changes over the last 10 billion years due to the effects of dark matter, dark energy and gravity.

Euclid will measure the shear from galaxy ellipticities for weak gravitational lensing studies. BAO will also be determined from a spectroscopic survey, with redshift precision greater than 0.001. Additionally, two 20 deg^2 deep field observations will be made in addition to the 15000 deg^2 wide survey.

Artistic view of the *Euclid* satellite is presented in Fig. 1.12, and the mission characteristics are summarized in Table1.2.

[7] https://www.Euclid-ec.org

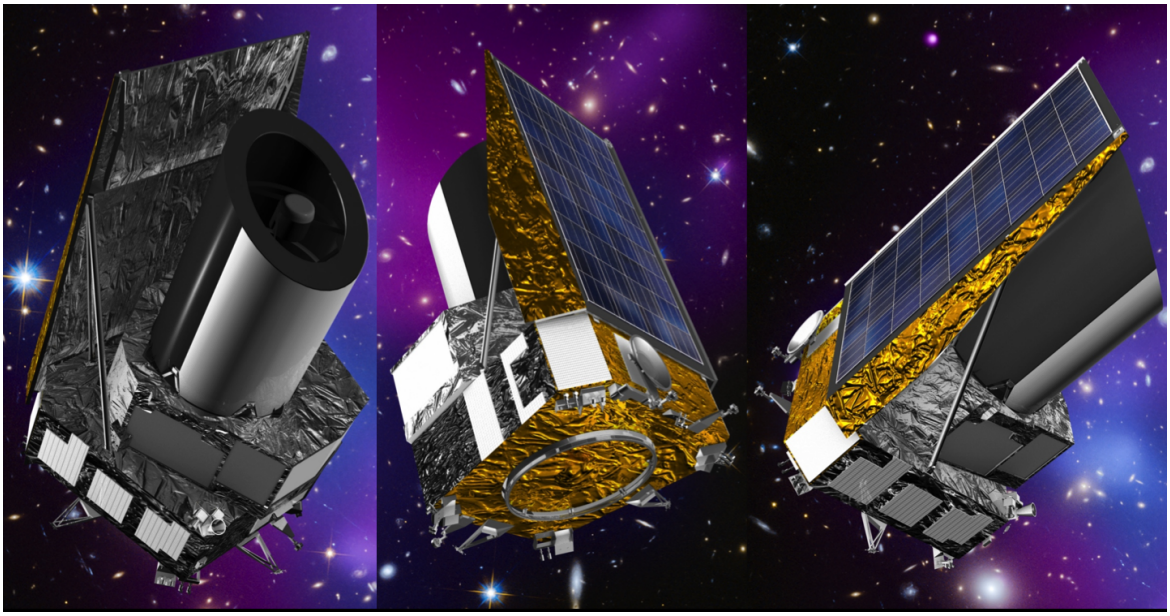

Figure 1.12: The artist view of the ESA medium class astronomy and astrophysics space mission *Euclid*. Credit: ESA (https://www.Euclid-ec.org.)

Table 1.2: Main characteristics of the *Euclid* mission. Credit: ESA (https://www.euclid-ec.org), Laureijs (2009); Amendola et al. (2018)

Mission	ESA M-class
Launch date	2022
Mission lifetime	6.25 years
Wavelength coverage	Visible in 550-900 nm and Near infrared in 900-2000 nm
Wide survey area	15000 deg^2
Deep survey area	40 deg^2
Instruments	Visible imager (VIS) and Near Infrared Spectrometer and Photometer (NISP)
Common VIS and NISP field of view	0.53 deg^2
VIS filters	Very broad band R+I+Z
NISP filters	Broad band Y, J, H
Minimum and maximum redshift	0.9 – 1.8

1.10.2 Science goals

Euclid is predominantly a cosmology and fundamental physics mission. The main aim of the mission is to understand the nature of dark energy and the accelerating expansion of the Universe. With the new observational data, we should be able to better understand the properties of dark energy, to test models of the origin of dark energy, and to test GR on different scales. It is hoped that the mission will aid in understanding dark energy and predicting the future evolution of the Universe. Another important goal is to explore the nature and properties of dark matter. A final goal is to reconstruct the initial conditions which led to the present cosmic structure of the Universe.

The observation of gravitational lensing effect on galaxies, BAO and RSD will help to study dark matter and dark energy via their impact on the expansion rate of the Universe, the growth of cosmic structures and the properties of galaxy clustering. In particular, the effect of dark matter can be detected by weak lensing observations. In combination with the angular distances, the expansion rate will be probed. Moreover, BAO is also a direct distance-redshift measurement for the same study. RSD probes the growth rate of cosmic structures and gravity. Therefore, the combination of these three probes provides multifaceted knowledge about dark energy. Also, independent observations of clusters of galaxies and the Integrated Sachs-Wolf effect (the effect caused by the gravitational redshift of CMB photons which occurs between the surface of last scattering and the Earth) will be done. They will be used to cross-check the results obtained from weak lensing, BAO and RSD and help to better understand and control systematic errors. In addition to the primary science, there are other questions which the *Euclid* mission will help to answer. The wide survey will provide observations of a billion galaxies for various studies. The deep survey will provide several million sources that will be unique samples for extragalactic and stellar astronomy. Also, many other issues as the CMB *Euclid* galaxy survey cross-correlations, strong lensing statistics, galaxy-galaxy lensing, cool brown dwarfs, large streams and merger histories of galaxies, stellar populations in the Galaxy, Galaxy evolution, exoplanets, supernovae and transients can be investigated with the *Euclid* mission.

Finally, the groundwork and experience of the *Euclid* Consortium will help other space missions and observatories e.g. *GAIA*[8], *e-ROSITA*[9], SKA[10], *JWST*[11], LSST[12], ALMA[13], *WFIRST*[14] etc.

[8] http://sci.esa.int/gaia/
[9] *extended ROentgen Survey with an Imaging Telescope Array* (*e-ROSITA*), https://www.mpe.mpg.de/eROSITA
[10] Square Kilometre Array (SKA), https://www.skatelescope.org
[11] *James Webb Space Telescope* (*JWST*), https://www.jwst.nasa.gov
[12] Large Synoptic Survey Telescope (LSST), https://www.lsst.org
[13] Atacama Large Millimeter Array (ALMA), https://www.almaobservatory.org/en/home
[14] *Wide Field Infrared Survey Telescope* (*WFIRST*), https://wfirst.gsfc.nasa.gov

CHAPTER 2

Cosmological information in the redshift-space bispectrum[1]

2.1 Introduction

The last decades have witnessed a tremendous increase in the size of galaxy redshift catalogues that culminated in the completion of the 2dFGRS and the SDSS as well as their more recent extensions. The scientific output of these efforts have been unprecedented and contributed to fostering several fields of astrophysics. The detection of BAO in the galaxy two-point statistics (Cole et al., 2005; Eisenstein et al., 2005) was a major breakthrough in cosmology, as it allowed us to measure the distance-redshift relation on large scales and thus reconstruct the expansion history of the Universe.

Still, there is need for conducting even wider and deeper observational campaigns to address several key issues: (i) the nature of dark energy and dark matter, (ii) the neutrino masses, (iii) the statistical properties of primordial density fluctuations. These are the main science drivers of the planned next generation of surveys that will be conducted, for instance, with the Dark Energy Spectroscopic Instrument (DESI) (DESI, DESI Collaboration et al., 2016a,b), the *Euclid* satellite (Laureijs, 2009) and the SKA (SKA, Maartens et al., 2015).

It is customary to extract cosmological information from galaxy catalogues using the two-point correlation function or its Fourier transform, the power spectrum. Either of these functions fully characterize a zero-mean Gaussian random field. However, the galaxy distribution displays complex patterns characterized by elongated filaments, compact clusters, and volume-filling underdense regions. These features are not captured by two-point statistics that do not retain information on the phases of the Fourier modes of the galaxy distribution. Therefore, if measured with sufficient accuracy and precision, higher-order statistics like the n-point correlation functions (with $n > 2$) and their Fourier transforms, the polyspectra, should contain additional information.

Until recently, galaxy redshift surveys could only provide rather noisy and imprecise measurements of higher-order statistics (Jing & Börner, 1998; Frieman & Gaztañaga, 1999; Scoccimarro et al., 2001; Verde et al., 2002; Croton et al., 2004; Jing & Börner, 2004; Kulkarni et al., 2007; Gaztañaga et al., 2009; Marín, 2011). In fact, the presence or the absence of rare large-scale structures within the surveyed volume can shift the estimated statistics significantly thus calling for the need to build

[1]This Chapter and Appendix A have been published in Yankelevich & Porciani (2019). The format has been adapted to match the remaining thesis.

statistically representative samples that cover larger volumes (Croton et al., 2004; Gaztañaga et al., 2005; Nichol et al., 2006). For this reason, there is a lack of dedicated tools (theoretical predictions, estimators, likelihood models) to analyse higher-order statistics with respect to those specifically developed for the power spectrum. However, the situation is gradually changing as surveys cover unprecedentedly large volumes sampled with high galaxy number densities (Gil-Marín et al., 2015, 2017; Slepian et al., 2017). In particular, the bispectrum will be robustly and accurately measured with the advent of the above-mentioned experiments of the next generation. Developing techniques for exploiting the galaxy bispectrum is thus necessary to maximize the scientific return of these missions.

Historically, the bispectrum has been considered as a useful tool to learn about the statistical properties of the primordial density perturbations that seeded structure formation (their degree of non-Gaussianity, in particular) and to study non-linear physical processes like gravitational dynamics and galaxy biasing. Since these processes generate different functional dependences on the triangular configurations, they can be disentangled by fitting the measurements with theoretical templates. This procedure, for instance, removes the degeneracy between the galaxy linear bias coefficient and the amplitude of the dark-matter perturbations invariably found in power-spectrum studies (e.g. Fry, 1994; Matarrese et al., 1997; Sefusatti et al., 2006).

Forecasts for the constraining power of the galaxy bispectrum usually determine the expected uncertainty for the bias and/or non-Gaussianity coefficients by assuming the main cosmological parameters are known exactly (Scoccimarro et al., 2004; Sefusatti & Komatsu, 2007; Song et al., 2015; Tellarini et al., 2016; Yamauchi et al., 2017a; Karagiannis et al., 2018). This strategy has been recently extended to modified theories of gravity (Yamauchi et al., 2017b). In this chapter, we follow a different approach and use the Fisher-matrix formalism to quantify the potential of the bispectrum as a means to extract additional cosmological information with respect to traditional power-spectrum studies. For surveys of the previous generation, a similar analysis has been presented by Sefusatti et al. (2006) who made forecasts for the combination of galaxy-clustering data from SDSS North with the analysis of the CMB performed by the *WMAP*. Given the substantially improved perspectives for studies of galaxy clustering, it is imperative to update the prior investigation by utilizing the characteristics of the forthcoming surveys. Recent related work focuses either on developing optimal compression algorithms for three-point statistics (Byun et al., 2017; Gualdi et al., 2019) or on detecting primordial non-Gaussianity due to the presence of massive spinning particles during inflation (Moradinezhad Dizgah et al., 2018). Here, we discuss the advantages (or lack thereof) of combining measurements of the galaxy power spectrum and bispectrum to constrain the standard cosmological parameters and, in particular, the dark-energy equation of state. In order to provide a concrete example, we focus on a *Euclid*-like survey and consider flat cosmological models dominated by dark energy and CDM with Gaussian primordial perturbations. We also combine the constraints from the clustering data with those from the CMB analysis by the *Planck* mission. Apart from considering datasets of current interest, we improve upon Sefusatti et al. (2006) in multiple other ways. For instance, we (i) consider the full galaxy bispectrum in redshift space instead of its monopole moment, (ii) make forecasts for dynamical dark-energy models, and (iii) account for a more sophisticated bias expansion that also depends on the tidal field and which represents the current state of the art. We are interested in the constraining power of two- and three-point statistics of the actual galaxy distribution in redshift space. Therefore, as a first step, we neglect observational limitations that will somewhat reshuffle and degrade the information. For example, we only approximately take into account the survey geometry through our binning strategy and neglect the Alcock-Paczynski effect (as in Sefusatti et al., 2006). These issues will be accounted for in our future work.

The Chapter is organized as follows. In Section 2.2, we introduce our notation and define the relevant statistical quantities. In Section 2.3, we briefly summarize the Fisher-matrix formalism and describe the set-up of our study. Our results are presented in Section 2.4 and discussed in Section 2.5. Finally, in Section 2.6, we conclude.

2.2 Galaxy statistics

2.2.1 Power spectrum and bispectrum

Given a galaxy population, we model its spatial distribution at fixed time as the discrete sampling of a continuous random field $\rho_{\rm g}(\boldsymbol{x})$ which gives the local galaxy density per unit comoving volume in the expanding Universe. We assume that $\delta_{\rm g}(\boldsymbol{x})$ is statistically homogeneous, i.e. that all its connected n-point correlation functions are invariant under spatial translations. After defining the mean galaxy density $\bar{\rho}_{\rm g} = \langle \rho_{\rm g}(\boldsymbol{x}) \rangle$ (the brackets here denote averages taken over an ideal ensemble of realisations), we introduce the dimensionless overdensity as

$$\delta_{\rm g}(\boldsymbol{x}) = \frac{\rho_{\rm g}(\boldsymbol{x})}{\bar{\rho}_{\rm g}} - 1 \,. \tag{2.1}$$

We would like to decompose $\delta_{\rm g}(\boldsymbol{x})$ into simple oscillatory functions like plane waves. For a generic absolutely integrable function $f(\boldsymbol{x})$, we can write

$$f(\boldsymbol{x}) = \int \tilde{f}(\boldsymbol{k})\, e^{i\boldsymbol{k}\cdot\boldsymbol{x}}\, \frac{\mathrm{d}^3 k}{(2\pi)^3} \,, \tag{2.2}$$

where

$$\tilde{f}(\boldsymbol{k}) = \int f(\boldsymbol{x})\, e^{-i\boldsymbol{k}\cdot\boldsymbol{x}}\, \mathrm{d}^3 x \tag{2.3}$$

denotes the Fourier transform of $f(\boldsymbol{x})$. However, $\delta_{\rm g}(\boldsymbol{x})$ cannot be Fourier transformed as, in almost all realisations, the integral $\int |\delta_{\rm g}(\boldsymbol{x})|\, \mathrm{d}^3 x$ diverges when taken over all space. Therefore, we consider a finite region of volume V and define a 'sample function' $\delta_V(\boldsymbol{x})$ such that $\delta_V(\boldsymbol{x}) = \delta_{\rm g}(\boldsymbol{x})$ if $\boldsymbol{x} \in V$ and $\delta_V(\boldsymbol{x}) = 0$ if $\boldsymbol{x} \notin V$. The power spectral density of $\delta_{\rm g}(\boldsymbol{x})$ can be defined as

$$P(\boldsymbol{k}) = \lim_{V\to\infty} \frac{\langle |\tilde{\delta}_V(\boldsymbol{k})|^2 \rangle}{V} = \lim_{V\to\infty} \frac{\langle \tilde{\delta}_V(\boldsymbol{k})\, \tilde{\delta}_V(-\boldsymbol{k}) \rangle}{V} \,, \tag{2.4}$$

where the limit exists only if it is performed after taking the ensemble average. In general, we can write

$$\langle \tilde{\delta}_V(\boldsymbol{k})\, \tilde{\delta}_V(\boldsymbol{q}) \rangle = \int \xi(r)\, e^{-i\boldsymbol{k}\cdot\boldsymbol{r}}\, \mathrm{d}^3 r \int_V e^{-i(\boldsymbol{k}+\boldsymbol{q})\cdot\boldsymbol{x}}\, \mathrm{d}^3 x \,, \tag{2.5}$$

where $\xi(\boldsymbol{r}) = \langle \delta_{\rm g}(\boldsymbol{x})\, \delta_{\rm g}(\boldsymbol{x}+\boldsymbol{r}) \rangle$ denotes the two-point correlation function of $\delta_{\rm g}(\boldsymbol{x})$ and the first integral runs over all separation vectors $\boldsymbol{r} = \boldsymbol{y} - \boldsymbol{x}$ such that $(\boldsymbol{x}, \boldsymbol{y}) \in V \times V$. Taking the limit for $V \to \infty$ and extending the definitions above to generalized functions, we obtain

$$\lim_{V\to\infty} \left\langle \tilde{\delta}_V(\boldsymbol{k})\, \tilde{\delta}_V(\boldsymbol{k}') \right\rangle = (2\pi)^3\, P(\boldsymbol{k})\, \delta_{\rm D}(\boldsymbol{k}+\boldsymbol{k}') \,, \tag{2.6}$$

where $\delta_{\rm D}(\boldsymbol{k})$ denotes the three dimensional Dirac delta distribution and the power spectrum $P(\boldsymbol{k})$ is the Fourier transform of $\xi(\boldsymbol{r})$.

Similarly, at the three-point level we can write

$$B(\boldsymbol{k}_1, \boldsymbol{k}_2, \boldsymbol{k}_3) = \lim_{V\to\infty} \frac{\langle \tilde{\delta}_V(\boldsymbol{k}_1)\, \tilde{\delta}_V(\boldsymbol{k}_2)\, \tilde{\delta}_V(-\boldsymbol{k}_1 - \boldsymbol{k}_2)\rangle}{V}\,, \tag{2.7}$$

or, equivalently,

$$\lim_{V\to\infty} \left\langle \tilde{\delta}_V(\boldsymbol{k}_1)\, \tilde{\delta}_V(\boldsymbol{k}_2)\, \tilde{\delta}_V(\boldsymbol{k}_3)\right\rangle = (2\pi)^3\, B(\boldsymbol{k}_1, \boldsymbol{k}_2, \boldsymbol{k}_3)\, \delta_{\rm D}(\boldsymbol{k}_{123})\,, \tag{2.8}$$

where $B(\boldsymbol{k}_1, \boldsymbol{k}_2, \boldsymbol{k}_3)$ defines the galaxy bispectrum (i.e. the Fourier transform of the connected three-point correlation function) and $\boldsymbol{k}_{123} = \boldsymbol{k}_1 + \boldsymbol{k}_2 + \boldsymbol{k}_3$, meaning that the bispectrum is defined only for closed triangles of wavevectors.

Different statistics (based on alternative expansions with respect to the Fourier decompositions) need to be employed to analyse samples that cover a wide solid angle on the sky (e.g. Fisher et al., 1994; Heavens & Taylor, 1995; Pápai & Szapudi, 2008).

2.2.2 Redshift-space distortions

We infer the comoving position of a galaxy by using two observables (position on the sky and redshift) and by assuming that the photons we receive from it propagate in an unperturbed Friedmann-Robertson-Walker model universe. The resulting galaxy distribution in this 'redshift space' provides a distorted representation of the actual one in 'real space' due to the presence of inhomogeneities and peculiar velocities. The latter generate the largest distortions (Jackson, 1972; Sargent & Turner, 1977; Kaiser, 1987; Hamilton, 1998) that dominate over other relativistic effects (see e.g. Borzyszkowski et al., 2017, and references therein) that we will neglect in this work.

Although the galaxy distribution in real space is statistically isotropic (implying that $P(\boldsymbol{k})$ only depends on the magnitude k and $B(\boldsymbol{k}_1, \boldsymbol{k}_2, \boldsymbol{k}_3)$ on the three values k_1, k_2 and k_3), RSD break this isotropy and introduce some angular dependences. In the distant-observer approximation, when galaxy separations are much smaller than the distance from the observer to the galaxies so that a single line of sight $\hat{\boldsymbol{s}}$ can be defined for the whole sample, the power spectrum in redshift space depends on k and $\mu = (\boldsymbol{k}\cdot\hat{\boldsymbol{s}})/k$. This result derives from the fact that density and velocity perturbations are correlated (Kaiser, 1987). Similarly, the redshift-space bispectrum depends on the line-of-sight projections μ_1 and μ_2 of $\boldsymbol{k}_1$ and $\boldsymbol{k}_2$ (as $\boldsymbol{k}_3 = -\boldsymbol{k}_1 - \boldsymbol{k}_2$). Therefore, the bispectrum depends on five variables, three of which determine the shape of the triangle of wavevectors while the remaining two indicate its orientation with respect to the line of sight. In Appendix A.1 we discuss two different parameterizations of the coefficients μ_1 and μ_2 in terms of convenient angular variables that here we schematically denote by $0 \le \theta \le \pi$ and $0 \le \phi < 2\pi$.

To reduce the complexity of cosmological investigations, the μ-dependence of the galaxy power spectrum at fixed wavenumber is often expanded in a Fourier-Legendre series (Taylor & Hamilton, 1996)

$$P(\boldsymbol{k}) = \sum_{\ell=0}^{\infty} P_\ell(k)\, \mathcal{L}_\ell(\mu)\,, \tag{2.9}$$

where $\mathcal{L}_\ell(\mu)$ denotes the Legendre polynomials and the functions

$$P_\ell(k) = \frac{2\ell+1}{2} \int_{-1}^{1} P(k)\, \mathcal{L}_\ell(\mu)\, \mathrm{d}\mu \tag{2.10}$$

are known as the 'redshift-space multipoles' of the power spectrum. In linear perturbation theory, only the monopole ($\ell = 0$), quadrupole ($\ell = 2$) and hexadecapole ($\ell = 4$) do not vanish (see equation (2.18) in Section 2.2.3 without the exponential term on the rhs). Recent studies show that these three multipoles indeed contain the bulk of the information on the main cosmological parameters (e.g. Taruya et al., 2011; Kazin et al., 2012; Beutler et al., 2014). Therefore, a simplified inference method (with small information loss) can be engineered by only considering three functions of k instead of a function of both k and μ. This approach can be generalized to the galaxy bispectrum. In fact, the dependence on the orientation of a triangle of wavevectors can be decomposed into spherical harmonics (Scoccimarro et al., 1999a),

$$B(\boldsymbol{k}_1, \boldsymbol{k}_2, \boldsymbol{k}_3) = \sum_{\ell=0}^{\infty} \sum_{m=-\ell}^{\ell} B_{\ell m}(k_1, k_2, k_3)\, Y_{\ell m}(\theta, \phi)\,, \tag{2.11}$$

where

$$B_{\ell m}(k_1, k_2, k_3) = \int_{-1}^{+1} \int_{0}^{2\pi} B(\boldsymbol{k}_1, \boldsymbol{k}_2, \boldsymbol{k}_3)\, Y^*_{\ell m}(\theta, \phi)\, \mathrm{d}\cos(\theta)\, \mathrm{d}\phi\,. \tag{2.12}$$

A popular choice is to focus on the coefficients with $m = 0$ which are often called the 'redshift-space multipoles' of the bispectrum. They satisfy a relation similar to equation (2.9) for the ϕ-averaged bispectrum:

$$\int_0^{2\pi} B(\boldsymbol{k}_1, \boldsymbol{k}_2, \boldsymbol{k}_3)\, \frac{\mathrm{d}\phi}{2\pi} = \sum_{\ell=0}^{\infty} B_{\ell 0}(k_1, k_2, k_3)\, \mathcal{L}_\ell(\cos\theta)\,. \tag{2.13}$$

These multipoles are simple to estimate from a galaxy catalogue using fast Fourier transform-based methods (Scoccimarro, 2015, see also Bianchi et al. (2015)) and provide a convenient procedure to compress the bispectrum measurements into data structures of lower dimensionality. This, however, unavoidably causes loss of information. For a fixed cosmological model, Gagrani & Samushia (2017) show that constraints on the velocity linear growth factor, galaxy bias coefficients and Alcock-Paczinsky parameters based on B_{00}, B_{20} and B_{40} are quite similar to those derived from the full (θ, ϕ) dependence of the bispectrum. This suggests that using only the lowest-order bispectrum multipoles is not associated with a significant loss of information about (at least) some selected cosmological parameters. We will revisit this issue using our own results in Section 2.5.3.

For the sake of completeness, in this work, we do not compress $P(\boldsymbol{k})$ and $B(\boldsymbol{k}_1, \boldsymbol{k}_2, \boldsymbol{k}_3)$ into their low-order multipoles and exploit their full angular dependence in redshift space. The price we pay for doing this is dealing with large data sets and high-dimensional covariance matrices.

2.2.3 Perturbative models

We model the galaxy power spectrum and the bispectrum in redshift space by combining three ingredients: (i) SPT for the growth of long-wavelength density and velocity perturbations in a single-stream collisionless fluid (see Bernardeau et al., 2002, for a review), (ii) a galaxy bias model, and (iii) a non-perturbative phenomenological model for RSD due to motions within virialized

structures ('finger-of-God' effect). We only consider expressions to the lowest non-vanishing order in the perturbations.

Definitions

We consider a flat FLRW background with expansion factor a and Hubble parameter H. The present-day value of H is $H_0 = 100\,h$ km s^{-1} Mpc^{-1}. We model dark energy as a barotropic fluid with equation of state $p = w\rho c^2$ where p and ρc^2 denote pressure and energy density, respectively, and w is a dimensionless parameter that can, in principle, change with a.

The evolution of a and H is regulated by Friedmann equations that can be expressed in terms of the present-day value of the matter density parameter Ω_m and the dark-energy equation of state. Neglecting the late-time contribution from radiation, we have

$$\frac{H^2}{H_0^2} = \left(\frac{\Omega_\mathrm{m}}{a^3} + (1-\Omega_\mathrm{m})\,\exp\left\{\left\{-3\int_1^a [1+w(x)]\;\mathrm{d}\ln x\right\}\right\}\right), \tag{2.14}$$

and the condition for the accelerated expansion of the Universe is $w < -1/3$.

On sub-horizon scales, linear density perturbations in the matter component grow proportionally to the growth factor D_+ that we compute by solving the ordinary differential equation

$$D_+'' + \left(\frac{3}{a} + \frac{\mathrm{d}\ln H}{\mathrm{d}\,a}\right) D_+' - \frac{3\Omega_\mathrm{m}}{2a^5\,(H^2/H_0^2)} D_+ = 0\,, \tag{2.15}$$

where the symbol $'$ denotes a derivative with respect to a. In order to link linear density and velocity perturbations, we introduce the growth-of-structure parameter

$$f = \frac{\mathrm{d}\ln D_+}{\mathrm{d}\ln a}\,. \tag{2.16}$$

Galaxy biasing

We adopt an Eulerian non-linear and non-local bias model to express the fluctuations in the galaxy density in terms of the underlying matter perturbations, $\delta(\boldsymbol{x})$, and the traceless tidal field with Cartesian components $s_{ij}(\boldsymbol{x}) = (\partial_i\partial_j - \delta_{ij}\,\nabla^2/3)\,\phi(\boldsymbol{x})$ (where δ_{ij} denotes the Kronecker symbol and the gravitational potential, $\phi(\boldsymbol{x})$, satisfies the Poisson equation $\nabla^2\phi = \delta$). Namely, we write

$$\delta_g(\boldsymbol{x}) = b_1\,\delta(\boldsymbol{x}) + \frac{b_2}{2}\left[\delta^2(\boldsymbol{x}) - \langle\delta^2(\boldsymbol{x})\rangle\right] + \frac{b_{s^2}}{2}\left[s^2(\boldsymbol{x}) - \langle s^2(\boldsymbol{x})\rangle\right], \tag{2.17}$$

where b_1, b_2 and b_{s^2} denote the linear, the non-linear and the tidal (non-local) bias parameters, respectively. Equation (2.17) extends the local bias model introduced by Fry & Gaztanaga (1993) to account for the anisotropy and environmental dependence of gravitational collapse (Catelan et al., 1998). The tidal-bias term alters the dependence of the galaxy bispectrum on the triangular configurations of the wavevectors (Catelan et al., 2000) and a non-vanishing b_{s^2} has been measured for dark-matter haloes extracted from cosmological simulations (Baldauf et al., 2012; Chan et al., 2012; Saito et al., 2014; Bel et al., 2015). The tidal bias is also required to ensure a proper renormalization (in the field-theory sense) of the quadratic local bias that is otherwise sensitive to short-wavelength

modes of the density field that are not suitable for a perturbative analysis (McDonald & Roy, 2009; Assassi et al., 2014; Desjacques et al., 2018).

Equation (2.17) is nowadays the standard bias model for the galaxy bispectrum and is routinely used to interpret observational data (Gil-Marín et al., 2015, 2017) and make forecasts for future missions (Tellarini et al., 2016; Moradinezhad Dizgah et al., 2018; Karagiannis et al., 2018).

Galaxy power spectrum and bispectrum

We only consider expressions to the lowest non-vanishing order in the perturbations corrected with a phenomenological model for non-linear RSD. For the galaxy power spectrum in redshift space we thus write

$$P(\boldsymbol{k}) = Z_1^2(\boldsymbol{k})\, P_{\rm L}(k)\, \exp\left[-\frac{(k\,\mu\,\sigma_{\rm p})^2}{2}\right], \tag{2.18}$$

where $P_{\rm L}$ is the power spectrum of linear matter-density fluctuations and

$$Z_1(\boldsymbol{k}) = Z_1(k,\mu) = b_1 + f\mu^2 \tag{2.19}$$

accounts for linear biasing and linear RSD. The exponential term, instead, provides a phenomenological (non-perturbative) characterization of the suppression of power due to non-linear velocities. It describes virialized motions as an incoherent Gaussian scatter with (scale-independent) pairwise velocity dispersion $a\,H\,\sigma_{\rm p}$ (here $\sigma_{\rm p}$ is conveniently expressed in units of $h^{-1}\,{\rm M}pc$) and it has been shown to approximately match the results of N-body simulations when $\sigma_{\rm p}$ is treated as a free parameter (Peacock, 1992; Peacock & Dodds, 1994; Ballinger et al., 1996). Note that $a\,H\,\sigma_{\rm p}$ does not coincide with the actual pairwise velocity dispersion of the galaxies (which is scale-dependent, e.g. Scoccimarro, 2004; Kuruvilla & Porciani, 2018) and should be merely considered as a nuisance parameter of the same order of magnitude. It is also important to stress that, at the scales analysed in this work, the exponential term in equation (2.18) is always very close to unity and can be approximated as $1-(k\,\mu\,\sigma_{\rm p})^2/2$. Therefore, our results do not depend on the assumption of a Gaussian (rather than a Lorentzian) damping factor.

Similarly, for the galaxy bispectrum we get

$$B(\boldsymbol{k}_1,\boldsymbol{k}_2,\boldsymbol{k}_3) = 2\,\left[Z_2(\boldsymbol{k}_1,\boldsymbol{k}_2)\,Z_1(\boldsymbol{k}_1)\,Z_1(\boldsymbol{k}_2)\,P_{\rm L}(k_1)P_{\rm L}(k_2) + {\rm cycl.}\right]\times \\ \times\,\exp\left[-(k_1^2\mu_1^2 + k_2^2\mu_2^2 + k_3^2\mu_3^2)\,\frac{\sigma_{\rm p}^2}{2}\right], \tag{2.20}$$

where the cyclic permutation runs over pairs of $\boldsymbol{k}_1$, $\boldsymbol{k}_2$ and $\boldsymbol{k}_3$ and the second-order kernel describing the effect of non-linearities due to dynamics, biasing and RSD is

$$Z_2(\boldsymbol{k}_i,\boldsymbol{k}_j) = \frac{b_2}{2} + b_1 F_2(\boldsymbol{k}_i,\boldsymbol{k}_j) + f\mu_{ij}^2 G_2(\boldsymbol{k}_i,\boldsymbol{k}_j) + \\ + \frac{f\mu_{ij}k_{ij}}{2}\left[\frac{\mu_i}{k_i}Z_1(\boldsymbol{k}_j) + \frac{\mu_j}{k_j}Z_1(\boldsymbol{k}_i)\right] + \frac{b_{s^2}}{2}S_2(\boldsymbol{k}_i,\boldsymbol{k}_j)\,. \tag{2.21}$$

Here, $\boldsymbol{k}_{ij} = \boldsymbol{k}_i + \boldsymbol{k}_j$ and $\mu_{ij} = \boldsymbol{k}_{ij}\cdot\hat{\boldsymbol{s}}/k_{ij}$, while F_2 and G_2 denote the second-order kernels of the

density and the velocity fields, respectively,

$$F_2(\boldsymbol{k}_i, \boldsymbol{k}_j) = \frac{5}{7} + \frac{m_{ij}}{2}\left(\frac{k_i}{k_j} + \frac{k_j}{k_i}\right) + \frac{2}{7}\,m_{ij}^2\,, \tag{2.22}$$

$$G_2(\boldsymbol{k}_i, \boldsymbol{k}_j) = \frac{3}{7} + \frac{m_{ij}}{2}\left(\frac{k_i}{k_j} + \frac{k_j}{k_i}\right) + \frac{4}{7}\,m_{ij}^2\,, \tag{2.23}$$

where $m_{ij} = \left(\boldsymbol{k}_i \cdot \boldsymbol{k}_j\right) / \left(k_i k_j\right)$. Finally, the tidal kernel

$$S_2(\boldsymbol{k}_i, \boldsymbol{k}_j) = m_{ij}^2 - \frac{1}{3}. \tag{2.24}$$

Although equations (2.22) and (2.23) hold true only in an Einstein-de Sitter universe, they provide accurate approximations in the general case (Scoccimarro et al., 1998; Bernardeau et al., 2002; Fonseca de la Bella et al., 2017). Consistently with the power-spectrum analysis, in equation (2.20), we adopt a Gaussian damping function to describe non-perturbative contributions to RSD. This term depends on the parameter σ_p that we also use for the power spectrum. Tests conducted against N-body simulations show that this is a reasonable approximation for matter clustering on sufficiently large scales and for redshifts $z > 0.5$ (Hashimoto et al., 2017). In this case, the best-fitting σ_p does not differ much from linear-theory predictions.

2.2.4 Discreteness effects

Galaxies are discrete objects and their clustering statistics are affected by shot noise. Assuming that their distribution derives from Poisson sampling an underlying continuous density field allows us to relate the observed spectra (denoted with a tilde) with those given in equations (2.18) and (2.20) (e.g. Matarrese et al., 1997). In terms of the galaxy number density, n_g,

$$\tilde{P}(\boldsymbol{k}) = P(\boldsymbol{k}) + P_\mathrm{shot}\,, \tag{2.25}$$

$$\tilde{B}(\boldsymbol{k}_1, \boldsymbol{k}_2, \boldsymbol{k}_3) = B(\boldsymbol{k}_1, \boldsymbol{k}_2, \boldsymbol{k}_3) + \left[P(\boldsymbol{k}_1) + P(\boldsymbol{k}_2) + P(\boldsymbol{k}_3)\right] P'_\mathrm{shot} + B_\mathrm{shot}\,, \tag{2.26}$$

where $P_\mathrm{shot} = P'_\mathrm{shot} = n_\mathrm{g}^{-1}$ and $B_\mathrm{shot} = n_\mathrm{g}^{-2}$.

2.3 Fisher matrix

2.3.1 Estimators and finite-volume effects

Actual redshift surveys cover finite comoving volumes and contain observational artefacts (gaps, masked regions, variable depth, etc.). Clustering statistics are thus measured using specifically designed estimators that minimize the impact of these features. An estimate for $\delta_\mathrm{g}(\boldsymbol{x})$ is usually computed by weighing the contribution of each galaxy based on the selection criteria of the survey (Feldman et al., 1994). Schematically, the observed galaxy overdensity can be written as $\delta_\mathrm{obs}(\boldsymbol{x}) = \delta_\mathrm{g}(\boldsymbol{x})\, W(\boldsymbol{x})$ (where $W(\boldsymbol{x})$ is the window function of the survey) so that $\tilde{\delta}_\mathrm{obs}(\boldsymbol{k}) = \int \tilde{W}(\boldsymbol{q})\, \tilde{\delta}_\mathrm{g}(\boldsymbol{k} - \boldsymbol{q})\, \mathrm{d}^3q/(2\pi)^3$. Therefore, an estimator for the power spectrum in redshift space can be built by replacing the ensemble average in equation (2.4) with a mean taken over a finite bin of wavevectors with similar values of k

and μ in a single realization:

$$\hat{P}_i = V^{-1} \int_{\mathcal{K}_i} \tilde{\delta}_{\rm obs}(\boldsymbol{k})\, \tilde{\delta}_{\rm obs}(-\boldsymbol{k})\, \frac{\mathrm{d}^3 k}{K_s}\,. \tag{2.27}$$

Here, $V = \int W(\boldsymbol{x})\, \mathrm{d}^3 x$ denotes the effective volume of the survey and K_s is the k-space volume covered by the bin $\boldsymbol{k} \in \mathcal{K}_i$. The ensemble average of $\hat{P}_i$ is

$$\langle \hat{P}_i \rangle = \int \tilde{W}(\boldsymbol{k}_i - \boldsymbol{q})\, P(\boldsymbol{q})\, \frac{\mathrm{d}^3 q}{(2\pi)^3} + \text{shot noise terms}\,, \tag{2.28}$$

and thus $\hat{P}_i$ is a biased estimator. This reflects the fact that plane waves (the basis functions of the Fourier expansion) are not orthonormal over a finite, non-periodic volume. Typically, $\tilde{W}(\boldsymbol{k})$ shows a prominent peak at $\boldsymbol{k} \simeq 0$ with a width of $\Delta k \sim V^{-1/3}$ (if the surveyed volume is not elongated, otherwise Δk coincides with the inverse of the shortest dimension). Therefore, the power-spectrum estimator in equation (2.27) mixes the contributions from Fourier modes with wavenumber differences $\Delta k < V^{-1/3}$. This is a manifestation of the uncertainty principle between conjugate variables in a Fourier transform: if the galaxy positions are confined to a region of linear size $V^{1/3}$, then the wavenumbers of the Fourier modes are 'uncertain' within a range $2\pi/V^{1/3}$.

Likewise, after introducing an estimator for the bispectrum that averages over a set of triangular configurations $\mathcal{T}_i$ centred around $(\boldsymbol{k}_1, \boldsymbol{k}_2, -\boldsymbol{k}_1 - \boldsymbol{k}_2)$

$$\hat{B}_i = V^{-1} \int_{\mathcal{T}_i} \tilde{\delta}_{\rm obs}(\boldsymbol{p})\, \tilde{\delta}_{\rm obs}(\boldsymbol{q})\, \tilde{\delta}_{\rm obs}(-\boldsymbol{p} - \boldsymbol{q})\, \frac{\mathrm{d}^3 p\, \mathrm{d}^3 q}{K_\triangle} \tag{2.29}$$

with

$$K_\triangle = \int_{\mathcal{T}_i} \delta_{\rm D}(\boldsymbol{p} + \boldsymbol{q} + \boldsymbol{k})\, \mathrm{d}^3 p\, \mathrm{d}^3 q\, \mathrm{d}^3 k\,, \tag{2.30}$$

(Scoccimarro, 2000) one finds (e.g. Gil-Marín et al., 2015)

$$\langle \hat{B}_i \rangle = \int \tilde{W}(\boldsymbol{k}_1 - \boldsymbol{q})\, \tilde{W}(\boldsymbol{k}_2 - \boldsymbol{q})\, B(\boldsymbol{q}_1, \boldsymbol{q}_2, -\boldsymbol{q}_1 - \boldsymbol{q}_2)\, \frac{\mathrm{d}^3 q_1}{(2\pi)^3}\, \frac{\mathrm{d}^3 q_2}{(2\pi)^3} + \text{shot noise terms}\,. \tag{2.31}$$

Although the systematic shift of $\hat{P}_i$ and $\hat{B}_j$ due to the window function is only noticeable on scales comparable with the extension of the survey, it needs to be accounted for in order to make unbiased inference about the cosmological parameters. One option is to deconvolve the window function from the measured spectra (Lucy, 1974; Baugh & Efstathiou, 1993; Lin et al., 1996). Alternatively, the theoretical models can be convolved with the window function of the survey before performing a fit to the measured spectra. A third possibility is not to use the Fourier decomposition and expand the galaxy density in orthonormal modes that maximize the signal-to-noise (S/N) ratio given the survey geometry and the selection function (plus a fiducial model for the spectra) using the Karhunen-Loève transform (Vogeley & Szalay, 1996; Tegmark et al., 1997).

For simplicity, in this work, we only approximately take into account the effects of the window function by considering k-bins of size $\Delta k = 2\pi/V^{1/3} = k_{\rm f}$ (i.e. the expected broadening for the

primary peak[1] of $\tilde{W}$ for a cubic survey volume of side $L = V^{1/3}$). We thus compute the band-averaged power spectra and bispectra by evaluating the mean over the set of configurations that contribute to each bin. Note that most forecast papers instead just use one characteristic configuration per bin to speed the calculation up.

2.3.2 Binning strategy and covariance matrices

Power spectrum

Within the distant-observer approximation, the galaxy power spectrum in redshift space is a function of k and μ^2. Therefore, we define our power-spectrum estimator using bins that run over a spherical shell of Fourier modes of widths Δk and $\Delta\mu$ and central values $\bar{k}_i$ and $\bar{\mu}_i$. In this case,

$$K_s = \int_{\mathcal{K}_i} \mathrm{d}^3 q = 2\pi\,\Delta\mu \left[\bar{k}^2 \Delta k + \frac{(\Delta k)^3}{12}\right] \simeq 2\pi\,\Delta\mu\,\bar{k}_i^2 \Delta k\,, \tag{2.32}$$

where the last expression on the right-hand side is valid only for narrow bins with $\Delta k \ll \bar{k}_i$. Note that the estimator in equation (2.27) is symmetric between $\boldsymbol{k}$ and $-\boldsymbol{k}$ meaning that, for every $\bar{k}_i$, it suffices to consider the interval $0 \leq \mu \leq 1$ and partition it over the bins of size $\Delta\mu$.

The covariance matrix of an estimator encodes information regarding the precision to which the estimand can be measured and the correlations between estimates corresponding to different configurations. The covariance matrix for the binned galaxy power spectrum is defined as

$$(C_{\mathrm{PP}})_{ij} = \langle (\hat{P}_i - \langle \hat{P}_i \rangle)\,(\hat{P}_j - \langle \hat{P}_j \rangle) \rangle = \langle \hat{P}_i\,\hat{P}_j \rangle - \langle \hat{P}_i \rangle\,\langle \hat{P}_j \rangle \tag{2.33}$$

and it can be decomposed in a disconnected (or Gaussian, since it is the only term present for a Gaussian random field) contribution and a connected (or non-Gaussian) contribution that is proportional to the trispectrum (the Fourier transform of the connected 4-point correlation function) of the galaxy distribution. On the large scales, we are interested in, the Gaussian contribution dominates (Scoccimarro et al., 1999b; Bertolini et al., 2016; Mohammed et al., 2017) and, for narrow bins, we can write (Feldman et al., 1994; Meiksin & White, 1999)

$$(C_{\mathrm{PP}})_{ij} \simeq \frac{2\,\tilde{P}_i^2}{N_P}\,\delta_{ij}\,, \tag{2.34}$$

where

$$N_P = \frac{K_s}{k_{\mathrm{f}}^3} \simeq \frac{V}{(2\pi)^2}\,\bar{k}_i^2\,\Delta k\,\Delta\mu\,. \tag{2.35}$$

The ratio $N_P/2$ gives the number of independent fundamental Fourier cells contributing to the band averaged power spectrum. The 2 at the denominator comes from the fact that the density field is real valued and $\tilde{\delta}(-\boldsymbol{k}) = \tilde{\delta}(\boldsymbol{k})^*$. Note that the statistical noise of $\hat{P}_i$ reflects the survey size: larger surveys contain more independent Fourier modes that contribute to a given bin and thus are associated with smaller random errors. Strictly speaking, equation (2.34) is exact only for cubic volumes with periodic boundary conditions but it is reasonable to expect that, to first approximation, the covariance does not

[1] If $W(\boldsymbol{x}) = 1$ within a cube of side L and 0 otherwise, then $\tilde{W}(\boldsymbol{k}) = \prod_{i=1}^{3} (2/k_i)\,\sin(k_i\,L/2)$ and the main peak along each Cartesian component extends for $\Delta k = 2\pi/L$ on the positive-frequency side.

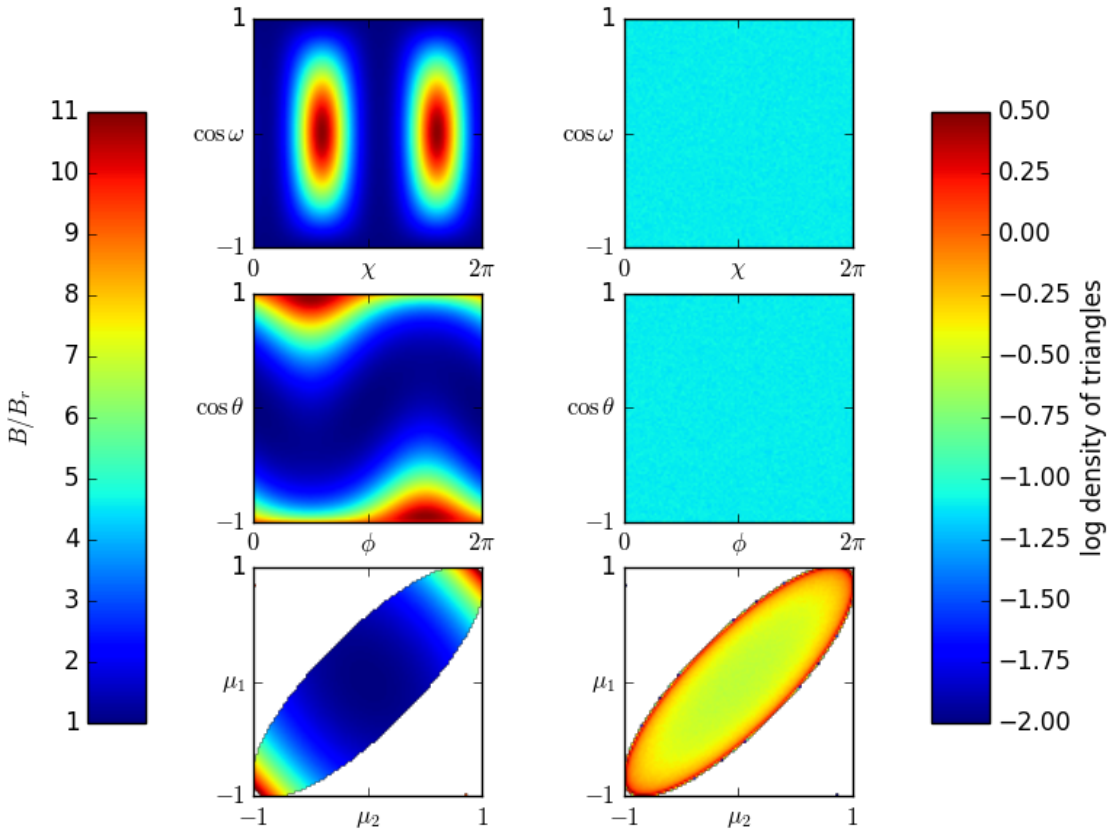

Figure 2.1: The panels on the left-hand side illustrate an example of how RSD affect the bispectrum. Shown is the ratio between the redshift-space and real-space bispectrum for a fixed triangular configuration of wavevectors with $(k_1, k_2, k_3) = (23, 14, 10) \times 3.93 \times 10^{-3}\, h\,\mathrm{Mpc}^{-1}$. From top to bottom, three different coordinate systems are used to parameterize the relative orientation of the triangle and the line of sight (see the main text and Appendix A.1 for details). The corresponding probability density of finding a triangle with a given orientation is shown in the right-hand-side panels.

depend on the survey shape (especially for $k \gg k_\mathrm{f}$). It is also worth mentioning that only the Gaussian part of C_PP is diagonal and non-linear couplings between Fourier modes generate non-vanishing off-diagonal terms.

Bispectrum

The galaxy bispectrum in redshift space depends on the triangular configuration of the wavevectors and its orientation with respect to the line of sight. In this section, we show that the orientation dependence severely complicates the analysis with respect to studies of the bispectrum in real space or the monopole in redshift space.

We characterize the shape of a triangle using an ordered triplet of numbers that indicate the length of its sides: $k_\mathrm{s} \leq k_\mathrm{m} \leq k_\mathrm{l}$. To describe its orientation, we need to use two angular variables that, for the moment, we denote using a generic solid angle Ω. Therefore, we define our bispectrum estimator

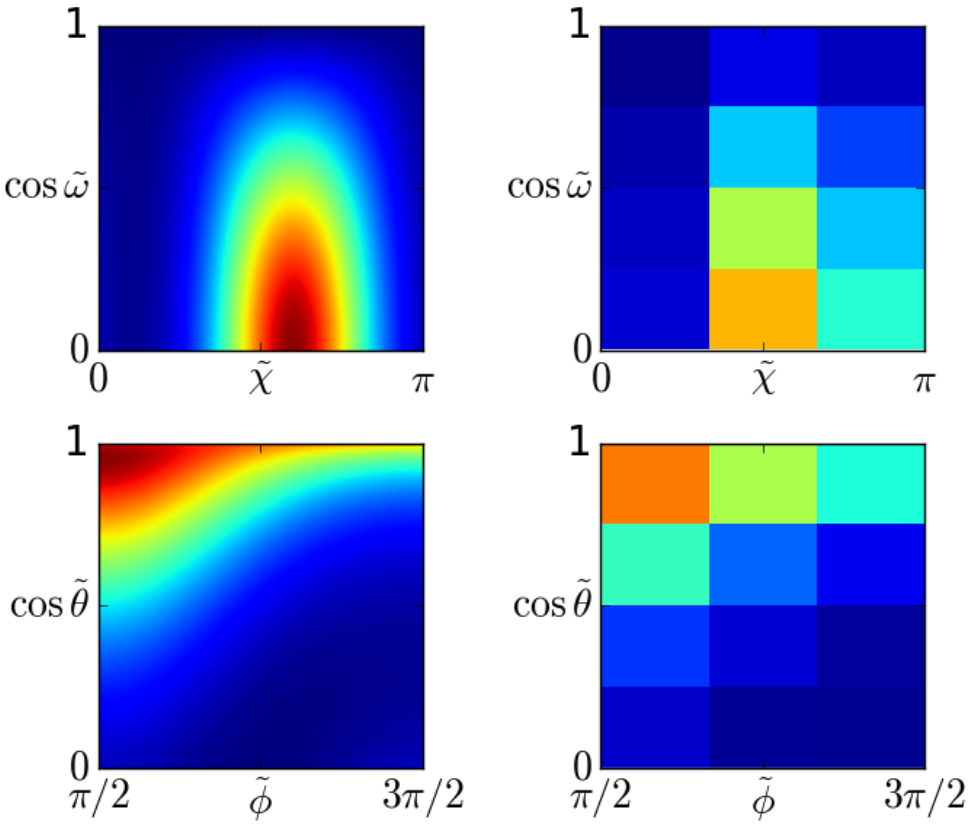

Figure 2.2: RSD displayed in Fig. 2.1 are now plotted as a function of the optimal angular coordinates $(\tilde{\omega}, \tilde{\chi})$ and $(\tilde{\theta}, \tilde{\phi})$. We adopt infinite resolution in the left-hand-side panels and partition parameter space into 12 bins in the right-hand-side panels. The colour coding is the same as in Fig. 2.1.

using finite bins with central values $\bar{k}_\mathrm{s}, \bar{k}_\mathrm{m}, \bar{k}_\mathrm{l}, \bar{\Omega}$ as well as widths $\Delta k_\mathrm{s} = \Delta k_\mathrm{m} = \Delta k_\mathrm{l} = \Delta k$ and $\Delta\Omega$. It follows that,

$$K_\triangle \simeq 8\pi^2\, \bar{k}_\mathrm{l}\, \bar{k}_\mathrm{m}\, \bar{k}_\mathrm{s}\, (\Delta k)^3\, \Sigma(\bar{\Omega})\, \Delta\Omega\,, \tag{2.36}$$

where $\Sigma(\bar{\Omega})\,\Delta\Omega$ denotes the fraction of triangles with fixed shape that populate a bin with solid angle $\Delta\Omega$, i.e. $\int_{4\pi} \Sigma(\Omega)\,\mathrm{d}\Omega = 1$. Note that the right-hand side of equation (2.36) should be divided by 2 for degenerate triangular configurations contained in a line (Mehrem, 2009; Chan & Blot, 2017).

We now discuss more in detail how to parameterize the orientation of a triangle with respect to the line of sight. To this end, in Appendix A.1, we introduce two different coordinate systems that we dub (ω, χ) and (θ, ϕ). They both define spherical coordinates but use different polar axes: the triangle's normal for (ω, χ) and one of the legs of the triangle for (θ, ϕ). A third possibility that more closely matches power-spectrum studies is to directly use μ_1 and μ_2 as indicators of the orientation of the triangle (e.g. Song et al., 2015). We briefly discuss here advantages and disadvantages of these three options. In the left column of Fig. 2.1, we show how RSD modify the shot-noise-subtracted galaxy bispectrum for a fixed triangular configuration. From top to bottom we show the ratio between the redshift-space bispectrum and its real-space counterpart as a function of (ω, χ), (θ, ϕ) and

(μ_1, μ_2). Note that, for selected orientations, RSD enhance the clustering signal by more than an order of magnitude. Obviously, the size of the distortions is the same in all panels but their overall pattern appears very different in the various coordinate systems that are connected by non-linear transformations.

Another important quantity to analyse is the function $\Sigma(\Omega)$ that determines the noise of the bispectrum estimator as a function of the orientation of the triangles. By construction, the number of triangles are uniformly distributed in $\mathrm{d}\cos\omega\,\mathrm{d}\chi$ and $\mathrm{d}\cos\theta\,\mathrm{d}\phi$, i.e. $\Sigma(\omega,\chi) = (4\pi)^{-1}\sin\omega$ and $\Sigma(\theta,\phi) = (4\pi)^{-1}\sin\theta$. On the other hand, the distribution of orientations gets more complicated when expressed in terms of the (μ_1, μ_2) coordinates. Using equations (A.7) and (A.8) to evaluate the Jacobian determinant of the coordinate transformation, we obtain[2]

$$\Sigma(\mu_1,\mu_2) = \left(2\pi\sqrt{\sin^2\xi_{12} - \mu_1^2 - \mu_2^2 + 2\cos\xi_{12}\,\mu_1\mu_2}\right)^{-1} . \tag{2.37}$$

The results of a Monte Carlo simulation obtained by randomly rotating the same triangle confirm our analytical results (the bottom right-hand panel in Fig. 2.1). Triangles only populate a finite region of the (μ_1, μ_2) plane bounded by an ellipse whose orientation depends on the shape of the triangles as defined by the shortest rotation angle ξ_{12} between $\boldsymbol{k}_1$ and $\boldsymbol{k}_2$. The density of triangles increases considerably towards the boundaries of the ellipse. Regrettably, this subtlety has been missed by Song et al. (2015) who, in their equation (20), assume that triangles are uniformly distributed within the entire (μ_1, μ_2) plane. Therefore, some care should be taken when interpreting their forecasts.

In the left column of Fig. 2.1, the symmetry between the triangles $(\boldsymbol{k}_1, \boldsymbol{k}_2, \boldsymbol{k}_3)$ and $(-\boldsymbol{k}_1, -\boldsymbol{k}_2, -\boldsymbol{k}_3)$ is evident. This corresponds to the transformations $(\omega,\chi) \to (\omega, \pi+\chi)$, $(\theta,\phi) \to (\pi-\theta, 2\pi-\phi)$ and $(\mu_1,\mu_2) \to (-\mu_1,-\mu_2)$. In practical applications, it makes sense, then, to select bins that combine these two configurations so that to reduce the size of the data and, as we are about to show, also get a diagonal covariance matrix (to first approximation). Moreover, RSD also possess an additional symmetry due to the fact that they only depend on $\sin\omega$ or $\sin\phi$. It is possible to 'fold' the original coordinate systems (ω,χ) and (θ,ϕ) so that to optimally exploit all these symmetries. We separately discuss how to do this in Section A.1.4 so as not to interrupt the flow of the discussion with technicalities. Here, it suffices to say that we end up using two sets of variables, $(\tilde{\omega},\tilde{\chi})$ or $(\tilde{\theta},\tilde{\phi})$, with the following range of variability: $0 \le \tilde{\omega} < \pi/2$, $0 \le \tilde{\chi} < \pi$, $0 \le \tilde{\theta} < \pi/2$, and $\pi/2 \le \tilde{\phi} < 3\pi/2$. Although they span a more compact range, the new coordinates fully cover the original parameter space shown in Fig. 2.1. The left column of Fig. 2.2 illustrates how they optimally isolate the basic pattern that repeats four times in Fig. 2.1. It is also worth stressing that random triangular orientations are still uniformly distributed in terms of the variables $(\cos\tilde{\omega},\tilde{\chi})$ and $(\cos\tilde{\theta},\tilde{\phi})$. For this reason, we partition parameter space into $N_\mathrm{p} \times N_\mathrm{a}$ identical bins of linear size $1/N_\mathrm{p}$ for the cosine of the polar angle (i.e. $\cos\tilde{\omega}$ or $\cos\tilde{\theta}$) and π/N_a for the azimuthal angle (i.e. $\tilde{\chi}$ or $\tilde{\phi}$). The right column of Fig. 2.2 shows an example of how RSD look like when $N_\mathrm{p} = 4$ and $N_\mathrm{a} = 3$.

The covariance matrix for the bispectrum estimator is

$$(C_\mathrm{BB})_{ij} = \langle(\hat{B}_i - \langle\hat{B}_i\rangle)\,(\hat{B}_j - \langle\hat{B}_j\rangle)\rangle = \langle\hat{B}_i\,\hat{B}_j\rangle - \langle\hat{B}_i\rangle\,\langle\hat{B}_j\rangle \tag{2.38}$$

where the indices i and j label bins of triangular configurations and orientations for the wavevectors.

[2] Since μ_2 only depends on $\sin\phi$, there are two values of ϕ that give the same μ_2. This explains the factor 2π in equation (2.37).

Also in this case, the covariance can be decomposed into Gaussian and non-Gaussian contributions that include terms up to the pentaspectrum (i.e. the Fourier transform of the connected six-point correlation function). The Gaussian part (which is expected to dominate on large scales) receives non-vanishing contributions whenever any one of the sides of the triangle i is the opposite vector to any one of the sides of the triangle j. Therefore, if the bispectrum bins are chosen such that a triangle and its negative end up in the same bin, we obtain (Fry et al., 1993; Scoccimarro et al., 2004; Sefusatti et al., 2006; Chan & Blot, 2017)

$$(C_{\rm BB})_{ij} \simeq \frac{s_{\rm B}\, V\, \tilde{P}_{i\rm l}\, \tilde{P}_{i\rm m}\, \tilde{P}_{i\rm s}}{N_B}\, \delta_{ij}\,, \tag{2.39}$$

where the indices $(i\rm l, i\rm m, i\rm s)$ identify the lengths and orientations of the sides of the triangular configuration $\triangle_i$ and

$$N_B \simeq \frac{K_\triangle}{k_{\rm f}^6} \simeq \frac{V^2}{8\pi^4}\, \bar{k}_{\rm l}\, \bar{k}_{\rm m}\, \bar{k}_{\rm s}\, (\Delta k)^3\, \Sigma(\bar{\Omega})\, \Delta\Omega \tag{2.40}$$

gives the number of triangles falling into a bin for shapes and orientations and the coefficient $s_{\rm B} = 6, 2, 1$ for equilateral, isosceles and scalene bin configurations, respectively. This number counts the matching pairs between the sides of the bins $\triangle_i$ and $\triangle_j$. Note that the diagonal elements of the covariance matrix are inversely proportional to the survey volume.

Finally, we consider the (rectangular) cross-covariance matrix between the estimators for the power spectrum and the bispectrum,

$$(C_{\rm PB})_{ij} = \langle (\hat{P}_i - \langle \hat{P}_i \rangle)\, (\hat{B}_j - \langle \hat{B}_j \rangle) \rangle = \langle \hat{P}_i\, \hat{B}_j \rangle - \langle \hat{P}_i \rangle\, \langle \hat{B}_j \rangle \tag{2.41}$$

which is composed of a disconnected part proportional to the product between P and B and a connected part proportional to the quadrispectrum (the Fourier transform of the connected 5-point correlation function). Sefusatti et al. (2006) report that, although this quantity does not have a Gaussian contribution, it is non-negligible even on large scales where the disconnected part dominates. In order to evaluate this term for our binning scheme, we need to generalize the expressions found in the literature that do not consider the orientation of the triangles. A non-vanishing cross-covariance is generated by configurations in which the wavevector $\boldsymbol{k}$ in the power-spectrum estimator, equation (2.27), coincides with (or with the reverse of) one of the legs $\boldsymbol{p}$, $\boldsymbol{q}$ and $-\boldsymbol{p}-\boldsymbol{q}$ of the triangle in the bispectrum estimator, equation (2.29). When the bins for the power spectrum ($\boldsymbol{k} \in \mathcal{K}_i$) and for the legs of the bispectrum triangles, $(\boldsymbol{p}, \boldsymbol{q}, -\boldsymbol{p}-\boldsymbol{q}) \in \mathcal{T}_j$, are taken with the same criterion (for instance by only requiring that $\bar{k}_i - \Delta k/2 < k < \bar{k}_i + \Delta k/2$, so that the bispectrum estimator can be labelled with three indices $\hat{B}_{j_1 j_2 j_3}$) either zero or all triangles in $\mathcal{T}_{j_1 j_2 j_3}$ have, say, $\boldsymbol{q} \in \mathcal{K}_i$ and the cross-covariance between $\hat{P}_i$ and $\hat{B}_{j_1 j_2 j_3}$ is given by $(C_{\rm PB})_{ij} \simeq 2\, s_{PB}\, \hat{P}_i\, \hat{B}_j\, (\delta_{ij_1} + \delta_{ij_2} + \delta_{ij_3})/N_P$ with $s_{PB} = 3, 2, 1$ for equilateral, isosceles and scalene triangles, respectively. However, to study the bispectrum in redshift space, we also bin in Ω and we need to take into account that $\mu_{\rm m}$ and $\mu_{\rm s}$ also depend on the angular variables. Because of this, the k-space volumes spanned by $\boldsymbol{k}_{\rm m}$ and $\boldsymbol{k}_{\rm s}$ within a triangular bin partially overlap with several power-spectrum bins. Let us denote by I_{ij_ℓ}/N_B the fraction of triangles in $\mathcal{T}_j$ that have $\boldsymbol{k}_\ell \in \mathcal{K}_i$ (i.e. a bin for k_ℓ and μ_ℓ). Then,

$$(C_{\rm PB})_{ij} \simeq 2\, s_{PB}\, \frac{\hat{P}_i\, \hat{B}_j}{N_P\, N_B}\, \left(I_{ij_1} + I_{ij_2} + I_{ij_3}\right)\,. \tag{2.42}$$

Table 2.1: Specifics of a *Euclid*-like survey in 14 non-overlapping redshift bins centred at z and of width $\Delta z = 0.1$. The comoving volume covered by the survey, V, the galaxy number density, $n_{\rm g}$, the characteristic halo mass, M_0, defined in equation (2.44), and the rescaled pairwise velocity dispersion, $\sigma_{\rm p}$, are expressed in units of h^{-3} Gpc^3, $10^{-3}\,h^3$ Mpc^{-3}, $10^{12}h^{-1}{\rm M}_\odot$, and h^{-1}Mpc, respectively.

z	V	n_g	b_1	b_2	b_{s^2}	M_0	$\mathcal{N}_{\rm HO}$	$\sigma_{\rm p}$
0.7	2.82	2.76	1.18	-0.76	-0.10	1.04	0.455	4.81
0.8	3.28	2.04	1.22	-0.76	-0.13	0.96	0.315	4.72
0.9	3.70	1.53	1.26	-0.75	-0.15	0.88	0.220	4.62
1.0	4.08	1.16	1.30	-0.74	-0.17	0.81	0.156	4.51
1.1	4.42	0.88	1.34	-0.72	-0.19	0.73	0.108	4.39
1.2	4.72	0.68	1.38	-0.70	-0.22	0.67	0.078	4.27
1.3	4.98	0.52	1.42	-0.68	-0.24	0.60	0.055	4.15
1.4	5.20	0.38	1.46	-0.66	-0.26	0.55	0.037	4.03
1.5	5.38	0.26	1.50	-0.63	-0.29	0.49	0.023	3.92
1.6	5.54	0.20	1.54	-0.60	-0.31	0.45	0.017	3.81
1.7	5.67	0.15	1.58	-0.57	-0.33	0.41	0.012	3.70
1.8	5.77	0.11	1.62	-0.53	-0.35	0.37	0.008	3.61
1.9	5.85	0.09	1.66	-0.49	-0.38	0.33	0.006	3.49
2.0	5.92	0.07	1.70	-0.45	-0.40	0.30	0.004	3.40

Note that $\sum_i I_{ij} = N_B$, where the sum is performed over all the bins for the power spectrum. For infinitesimally narrow bins, we can derive the coefficients I_{ij} analytically starting from equations (A.5) and (A.6) or (A.7) and (A.8). However, for the broad angular bins we consider in this work, we determine them numerically.

2.3.3 Survey characteristics and fiducial values

As an example of the forthcoming next generation of galaxy redshift surveys, we consider a *Euclid*-like mission. Within six years starting from 2021, the *Euclid* space telescope is expected to complete a wide survey that will measure $\sim 6 \times 10^7$ galaxy redshifts over 15000 square degrees on the sky (Laureijs, 2009). Low-resolution (slitless) spectroscopy in the near infrared will target the emission lines (mainly Hα) of star-forming galaxies in the approximate redshift interval $0.7 < z < 2.0$.

Since only relatively small samples have been observed so far (for a summary see, e.g., Pozzetti et al., 2016), little is known about the population of emission-line galaxies at these redshifts. Therefore, we must approximate the specifics of a *Euclid*-like survey by using theoretical models that have been calibrated against the current data. In particular, we adopt model 1 in Pozzetti et al. (2016) for the luminosity function of Hα-selected galaxies and assume a limiting flux of $F_{{\rm H}\alpha} > 3 \times 10^{-16}$ erg cm^{-2} s^{-1}. In Table 2.1, we report the corresponding galaxy number densities, $n_{\rm g}$, as a function of redshift. In order to facilitate comparison with previous work, we adopt the same binning strategy as in the *Euclid* Definition Study Report (Laureijs, 2009) and in many other forecasts for this mission (e.g. Amendola et al., 2018): 14 non-overlapping redshift bins of width $\Delta z = 0.1$ whose central values are linearly spaced between 0.7 and 2.0.

The clustering properties of Hα emitters at $z \sim 1$ are also very poorly constrained. Semi-analytic models of galaxy formation combined with N-body simulations suggest that the linear bias parameter

of the emission-line galaxies that will be detected by *Euclid* should be slightly above unity at $z \sim 0.7$ and grow with redshift (Orsi et al., 2010). An approximate fit (that we adopt) for the effective linear bias in each redshift bin is $b_1 = 0.9 + 0.4\,z$ (see appendix A in Pozzetti et al., 2016) although observations over two degree-sized fields at slightly higher redshifts indicate that b_1 could be a bit higher ($b_1 = 2.4^{+0.1}_{-0.2}$ at $z = 2.23$, Geach et al., 2012). Determining realistic fiducial values for the quadratic and tidal bias coefficients of *Euclid* galaxies requires making some additional assumptions. It is a basic tenet of the standard cosmological model that galaxies lie within dark-matter haloes: a central galaxy sits in the densest region of a halo while multiple satellites can be found in the outskirts. The linear and quadratic bias coefficients of the host haloes depend on the halo mass and redshift but can be related to each other by using fitting functions calibrated against N-body simulations, typically polynomials of second or third order (Lazeyras et al., 2016; Hoffmann et al., 2017). Similarly, if halo formation is a local process in Lagrangian space and there is no initial tidal bias, then

$$b_{s^2} = \frac{4}{7}\,(1 - b_1) \tag{2.43}$$

(Catelan et al., 1998, 2000; Baldauf et al., 2012; Chan et al., 2012). In brief, under some reasonable assumptions, knowing b_1 is sufficient to derive b_2 and b_{s^2} for the host haloes. In order to extend this method to the galaxies, we model their halo-occupation number $\langle N_\mathrm{g}|M\rangle$ that gives the mean number of galaxies contained within a single dark-matter halo of mass M. Uncountable studies have shown that, for galaxies selected by luminosity in a broadband optical filter (or by stellar mass), $\langle N_\mathrm{g}|M\rangle$ can be well approximated by the sum of a step function (describing central galaxies and ranging between 0 and 1) and a power law (describing satellite galaxies). However, when galaxies are selected by the intensity of an emission line (or by star-formation rate), $\langle N_\mathrm{g}|M\rangle$ is better described by a uni-modal function that always assumes values smaller than one (for the central galaxies) plus a power law (for the satellites). The latter parameterization has been used by Geach et al. (2012) to model the observed clustering of Hα emitters at $z \sim 2.2$ and by Gonzalez-Perez et al. (2018) to describe the population of [O$_\mathrm{II}$] emitters in a semi-analytic model of galaxy formation. We approximate their results by using a simple expression containing a free parameter (M_0) that determines the typical halo mass and a second one ($\mathcal{N}_\mathrm{HO} \leq 0.95$) that fixes the overall normalization:

$$\langle N_\mathrm{g}|M\rangle = \mathcal{N}_\mathrm{HO}\,(\langle N_\mathrm{c}|M\rangle + \langle N_\mathrm{s}|M\rangle) \tag{2.44}$$

with

$$\langle N_\mathrm{c}|M\rangle = \exp\left\{\left\{-10\left[\log_{10}\left(\frac{M}{M_0}\right)\right]^2\right\}\right\} + 0.05\,\Theta\left(\frac{M}{M_0}\right), \tag{2.45}$$

$$\langle N_\mathrm{s}|M\rangle = 0.003\,\frac{M}{M_0}\,\Theta\left(\frac{M}{M_0}\right), \tag{2.46}$$

and

$$\Theta\left(\frac{M}{M_0}\right) = 1 + \mathrm{erf}\left[2\log_{10}\left(\frac{M}{M_0}\right)\right]. \tag{2.47}$$

The first term on the right-hand side of equation (2.44) describes the halo occupation number of central galaxies while the second one refers to satellite galaxies. Here, M_0 denotes the halo mass at which the mean number of central galaxies reaches its maximum. Given the halo mass function $n(M)$ in each redshift bin (Sheth et al., 2001), we determine M_0 by requiring that the effective linear bias of

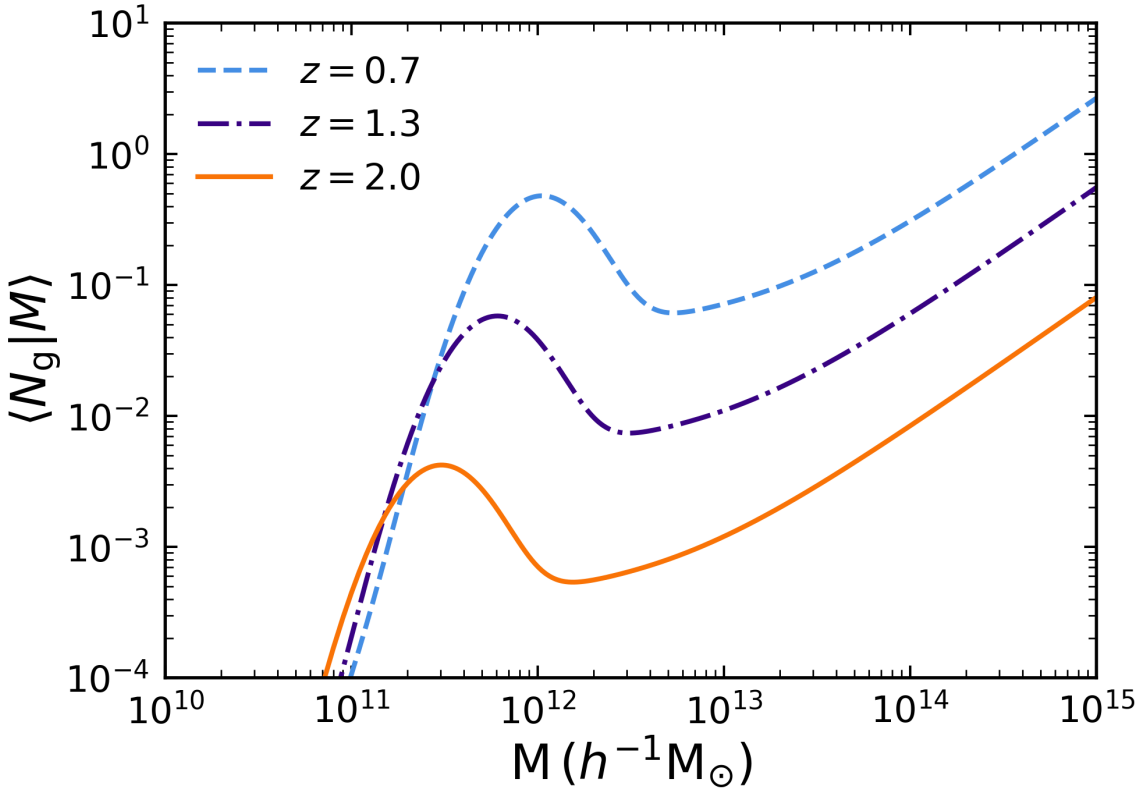

Figure 2.3: Halo-occupation number of the *Euclid* galaxies at different redshifts.

the *Euclid* galaxies

$$b_{eff} = \frac{\int b_1(M)\, n(M)\, \langle N_g|M\rangle \, \mathrm{d}M}{\int n(M)\, \langle N_g|M\rangle \, \mathrm{d}M} \tag{2.48}$$

coincides with the fit given in Pozzetti et al. (2016). Using the resulting M_0, we then determine the effective value of b_2 by averaging the quadratic halo bias with weights given by the mass function and the halo occupation number as in equation (2.48). We have checked the stability of our results with respect to the parameterization of the halo mass function (Bhattacharya et al., 2011, and references therein). Note that, since the halo tidal bias depends linearly on b_1, we can obtain b_{s^2} for the galaxies directly from their linear bias. The complete set of the bias coefficients we obtain is listed in Table 2.1. It is worth stressing that the values of b_2 are always slightly less negative than (but very close to) those that would be obtained from b_1 by straightforwardly applying the relation between the bias parameters that holds for dark-matter haloes. This shows that the details of the halo-occupation model are not very important for determining b_2 and strengthen our confidence in the approximate methods we have used. For the sake of completeness, in Fig. 2.3, we plot the halo-occupation number of the *Euclid* galaxies at different redshifts. The normalization constant $\mathcal{N}_{\mathrm{HO}}$(unnecessary to determine the bias coefficients) is obtained by requiring that $n_g = \int n(M)\, \langle N_g|M\rangle \, \mathrm{d}M$ (see Table 2.1).

The last parameter we need to fix in order to build a fiducial model for the power spectrum and

Table 2.2: Summary of the cosmological models considered in this chapter. Here, $N_{\rm par}$ indicates the total number of free parameters in the fit while the last column gives the name of the Monte Carlo generated Markov chains for the *Planck* data we use to generate the prior.

Model	$N_{\rm par}$	Cosmology	Bias	Nuisance	*Planck* sample
			14 z-bins	14 z-bins	
ΛCDM	61	$\Omega_{\rm cdm}$, $\Omega_{\rm b}$, h, $n_{\rm s}$, A	$b_1(z)$, $b_2(z)$, $b_{s^2}(z)$	$\sigma_{\rm p}(z)$	base-plikHM-TTTEEE-lowTEB
wCDM	62	$\Omega_{\rm cdm}$, $\Omega_{\rm b}$, h, $n_{\rm s}$, A, w	$b_1(z)$, $b_2(z)$, $b_{s^2}(z)$	$\sigma_{\rm p}(z)$	w-base-plikHM-TTTEEE-lowTEB
w_0w_aCDM	63	$\Omega_{\rm cdm}$, $\Omega_{\rm b}$, h, $n_{\rm s}$, A, w_0, w_a	$b_1(z)$, $b_2(z)$, $b_{s^2}(z)$	$\sigma_{\rm p}(z)$	base-w-wa-plikHM-TT-lowTEB-BAO

the bispectrum of *Euclid* galaxies is the rescaled pairwise velocity dispersion, $\sigma_{\rm p}$. As we briefly mentioned above, N-body simulations suggest that, at the redshifts of interest here, $\sigma_{\rm p}$ can be well approximated by linear-theory predictions (Hashimoto et al., 2017). Therefore, neglecting velocity bias, we write $\sigma_{\rm p}^2 = 2\,\sigma^2$ (where $a\,H\,\sigma$ denotes the 1-dimensional velocity dispersion for the dark matter) with

$$\sigma^2 = \frac{f^2}{3}\int_0^\infty \frac{P_{\rm L}(k)}{k^2}\,\frac{{\rm d}^3k}{(2\pi)^3} = \frac{f^2}{6\pi^2}\int_0^\infty P_{\rm L}(k)\,{\rm d}k\,. \tag{2.49}$$

Our results are summarized in Table 2.1.

2.3.4 Cosmological models

Within the CDM scenario with Gaussian initial conditions, we consider three classes of cosmological models characterized by different parameterizations for the equation-of-state parameter of dark energy, w.

We first examine plain vanilla CDM models with a cosmological constant, where $w = -1$ (ΛCDM). They are controlled by 5 parameters. The present-day values of the density parameters for dark matter, $\Omega_{\rm cdm}$, and baryons, $\Omega_{\rm b}$, as well as the Hubble constant, h, fully determine the background. At the same time, we assume a power-law form for the power spectrum of primordial (scalar, adiabatic) curvature perturbations

$$\mathcal{P}_{\mathcal{R}}(k) = A\left(\frac{k}{k_*}\right)^{n_{\rm s}-1}\,, \tag{2.50}$$

which is then completely determined by the spectral index $n_{\rm s}$ and the amplitude A at the pivot scale $k_* = 0.05\,{\rm Mpc}^{-1}$.

The simplest extension to ΛCDM we consider is a phenomenological model in which w stays constant with time but can assume values different from -1. We refer to this case, where w is treated as a sixth cosmological parameter, as wCDM.

The next level of complexity is to use two parameters to describe a time-varying equation of state (see e.g. Sahni & Starobinsky, 2006, for a review). We adopt the popular choice of assuming that w evolves linearly with a and write

$$w = w_0 + w_a\,(1-a) \tag{2.51}$$

(Chevallier & Polarski, 2001; Linder, 2003). Here, w_0 gives the present-day value of the equation-of-state parameter while w_a describes its current rate of change. Although, these phenomenological parameters provide a useful tool to detect deviations from a cosmological constant from experiments, it is not straightforward to map them on to physical dark-energy models (e.g. Scherrer, 2015). Note

that equation (2.51) describes a monotonic (and rather gentle) evolution from the primordial value of $w_0 + w_a$ to w_0.

In all cases, as a fiducial model we use the ΛCDM solution with the best-fitting parameters for the 'TT+lowP+lensing' *Planck* 2015 results (Planck Collaboration et al., 2016): namely, $\Omega_{\rm cdm} = 0.2596$, $\Omega_{\rm b} = 0.0484$, $h = 0.6781$, $n_{\rm s} = 0.9677$, $A = 2.139 \times 10^{-9}$, and $w = -1$. Linear transfer functions for the matter perturbations are computed using the CAMB code (https://camb.info, Lewis et al., 2000; Howlett et al., 2012).

2.3.5 Method

For each redshift interval, we build a data vector that combines the (shot-noise corrected) expectation values for the galaxy power spectrum and the bispectrum in the selected configuration bins. Schematically, we write $\mathbf{D} = (P, B)$ and we compute the Fisher information matrix

$$F_{\alpha\beta} = \frac{\partial \mathbf{D}}{\partial p_\alpha} \cdot \mathbf{C}^{-1} \cdot \frac{\partial \mathbf{D}^T}{\partial p_\beta}, \tag{2.52}$$

where p_α and p_β indicate two of the model parameters and $\mathbf{C}$ is the block covariance matrix

$$\mathbf{C} = \begin{pmatrix} \mathbf{C}_{\rm PP} & \mathbf{C}_{\rm PB} \\ \mathbf{C}_{\rm BP} & \mathbf{C}_{\rm BB} \end{pmatrix}, \tag{2.53}$$

that can be conveniently inverted using

$$\mathbf{C}^{-1} = \begin{pmatrix} \mathbf{C}_{\rm A} & -\mathbf{C}_{\rm A}\mathbf{C}_{\rm PB}\mathbf{C}_{\rm BB}^{-1} \\ -\mathbf{C}_{\rm BB}^{-1}\mathbf{C}_{\rm BP}\mathbf{C}_{\rm A} & \mathbf{C}_{\rm BB}^{-1} + \mathbf{C}_{\rm BB}^{-1}\mathbf{C}_{\rm BP}\mathbf{C}_{\rm A}\mathbf{C}_{\rm PB}\mathbf{C}_{\rm BB}^{-1} \end{pmatrix}, \tag{2.54}$$

with $\mathbf{C}_{\rm A} = (\mathbf{C}_{\rm PP} - \mathbf{C}_{\rm PB}\mathbf{C}_{\rm BB}^{-1}\mathbf{C}_{\rm BP})^{-1}$. We then sum the partial Fisher information matrices obtained for the different redshift intervals and invert the resulting matrix to make a forecast for the covariance matrix of the model parameters.

As a reference case, we consider wavevectors with $k < k_{\rm max}$ where $k_{\rm max} = 0.15\,h\,{\rm Mpc}^{-1}$. This is for three reasons. First, with the current state of the art, it is challenging to model non-linearities in P and B for much larger wavenumbers with an accuracy that allows applications to precision cosmology. Lazanu et al. (2016) have recently tested various models for the real-space bispectrum of matter perturbations against N-body simulations. To the lowest non-vanishing order (tree level), SPT statistically matches the numerical results to better than 5 per cent up to $k_{\rm max} = 0.17\,h\,{\rm Mpc}^{-1}$ for $z = 1$ and $k_{\rm max} = 0.20\,h\,{\rm Mpc}^{-1}$ for $z = 2$. Extending the calculation to next-to-leading order (i.e. adding one-loop corrections) considerably broadens the range of validity of the theory at $z \sim 2$. Substantially larger values for $k_{\rm max}$ at all redshifts (by up to a factor of two, see table II in Lazanu et al., 2016) can also be obtained by either reorganizing the perturbative expansion (e.g. Matsubara, 2008; Crocce et al., 2012) or by adopting an effective-field-theory approach in which the influence of non-perturbative small-scale physics on to the large-scale perturbations is described with modified fluid equations whose extra parameters are calibrated against numerical simulations (e.g. Baumann et al., 2012; Carrasco et al., 2012; Angulo et al., 2014; Baldauf et al., 2015). However, accounting for galaxy biasing, RSD and discreteness effects provide additional challenges for the perturbative models and reduces their range of validity. Secondly, the numerical inversion of $\mathbf{C}$ becomes more

and more demanding with increasing $k_{\rm max}$. In fact, since we use a minimal bin size of $\Delta k = k_{\rm f}$, we end up dealing with very high-dimensional matrices mainly due to the large number of possible triangle configurations for the bispectrum. Our default choice is to use 8 bins (i.e. $N_{\rm p} = 4$ and $N_{\rm a} = 2$) for the triangle orientations with respect to the line of sight. In this case, we use between approximately 31,200 and 65,500 bispectrum bins. Although the outcome of our study does not depend on the adopted angular coordinate system, we only show results obtained by taking bins in $\cos\tilde{\theta}$ and $\tilde{\phi}$. A third motivation for limiting our study to $k_{\rm max} = 0.15\,h\,{\rm Mpc}^{-1}$ is that non-linear effects strongly enhance the non-Gaussian contributions for all the sub-matrices that form $\mathbf{C}$ (e.g. Chan & Blot, 2017). In consequence, the information content of P and B strongly deviates from simplistic expectations based on counting Fourier modes. For instance, when one analyses the power spectrum, these effects lead to the so-called 'translinear information plateau' (Rimes & Hamilton, 2005; Neyrinck & Szapudi, 2007; Takahashi et al., 2009). Basically, with increasing $k_{\rm max}$, the cumulative information about a cosmological parameter grows until it saturates (for $k_{\rm max} \gtrsim 0.2\,h\,{\rm Mpc}^{-1}$). Only by analyzing much smaller (non-perturbative) scales ($k_{\rm max} \gg 1\,h\,{\rm Mpc}^{-1}$) can one retrieve useful information again. Although there are indications that the cumulative information stored in the bispectrum might saturate at smaller scales than for the power spectrum, it is also evident that, in the mildly non-linear regime, it increases at a much smaller rate than in the Gaussian approximation (Kayo et al., 2013; Chan & Blot, 2017). These considerations, together with the fact that the hierarchy of correlation functions (and their Fourier transforms) should be a rather inefficient tool to retrieve information from perturbations on fully non-linear scales (Carron, 2012; Carron & Neyrinck, 2012), have motivated alternative approaches for retrieving the information based on non-linear transforms and Gaussianization procedures (e.g. Carron & Szapudi, 2014, and references therein).

In Table 2.2 we summarize the cosmological and nuisance parameters used in our main investigation. As detailed in Section 2.3.4, the cosmology is specified by fixing 5 to 7 variables depending on the adopted parameterization of the dark-energy equation of state. In parallel, for each redshift bin, we consider 3 bias parameters and the pairwise velocity dispersion, for a total of 56 nuisance parameters that characterize the galaxy population under study. In Section 2.5, we will discuss some modifications to this set-up and their implications.

2.3.6 Priors

Bayesian statistics requires adopting a prior probability distribution for the model parameters. In this regard, we perform our analysis in two steps. First, we study the constraining power on cosmology of a *Euclid*-like survey by itself. In this case, we use directly the Fisher matrix to produce our forecasts. This procedure only uses information from the likelihood function and corresponds to adopting very diffuse priors on all the parameters. Subsequently, we combine the results of this first exercise with the constraints coming from the study of cosmic-microwave-background anisotropies performed by the *Planck* mission. To do this, we proceed as follows. For each of the cosmological models introduced in Section 2.3.4, we download a Markov chain that samples the posterior distribution from the *Planck* web-page[3] and compute the corresponding covariance matrix for the subset of cosmological parameters considered here. We then invert the covariance matrix and sum the result to the *Euclid*-like Fisher matrix. In practice, we treat the *Planck* results as Gaussian priors for our study of galaxy clustering. The exact names of the files we use are reported in Table 2.2. Note that, for the $w_0 w_a$CDM

[3] https://wiki.cosmos.esa.int/planckpla2015/index.php/ Cosmological_Parameters

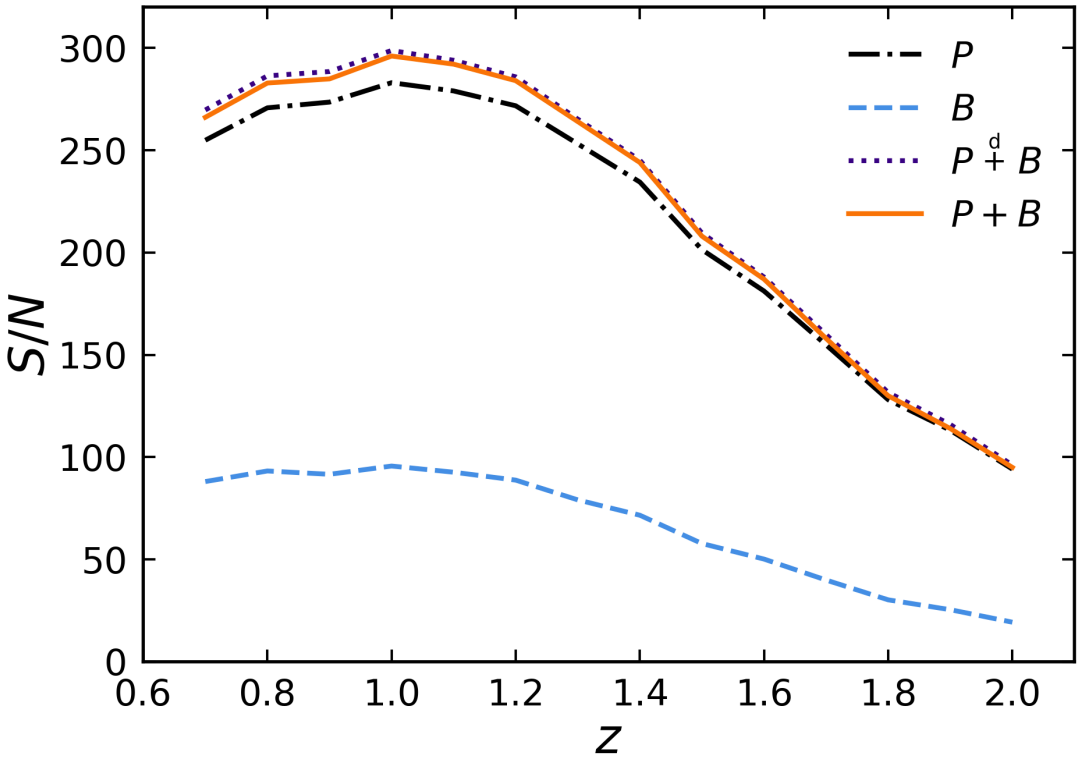

Figure 2.4: Signal-to-noise ratio for measurements of the galaxy power spectrum and the bispectrum in a *Euclid*-like survey as a function of redshift. We show results for the redshift-space power spectrum (dot-dashed), the redshift-space bispectrum (dashed) and their combination (solid). For comparison, we also display the S/N computed by neglecting the cross-covariance between P and B (dotted).

models, we use a combination of current CMB and galaxy-clustering data.

2.4 Results

2.4.1 Signal-to-noise ratio

In Fig. 2.4, we quantify the statistical significance with which the redshift-space power spectrum and bispectrum of *Euclid* galaxies will be measured. We plot the S/N ratio

$$\left(\frac{S}{N}\right)^2 = \mathbf{D}\cdot\mathbf{C}^{-1}\cdot\mathbf{D}^T\,, \tag{2.55}$$

as a function of redshift (solid). We also show individual results for P (dot-dashed) and for B (dashed) as well as for their combination when the cross-covariance $\mathbf{C}_{PB}$ is assumed to vanish (dotted). Thanks to the huge volume covered by the *Euclid*-like survey, both the power spectrum and the bispectrum

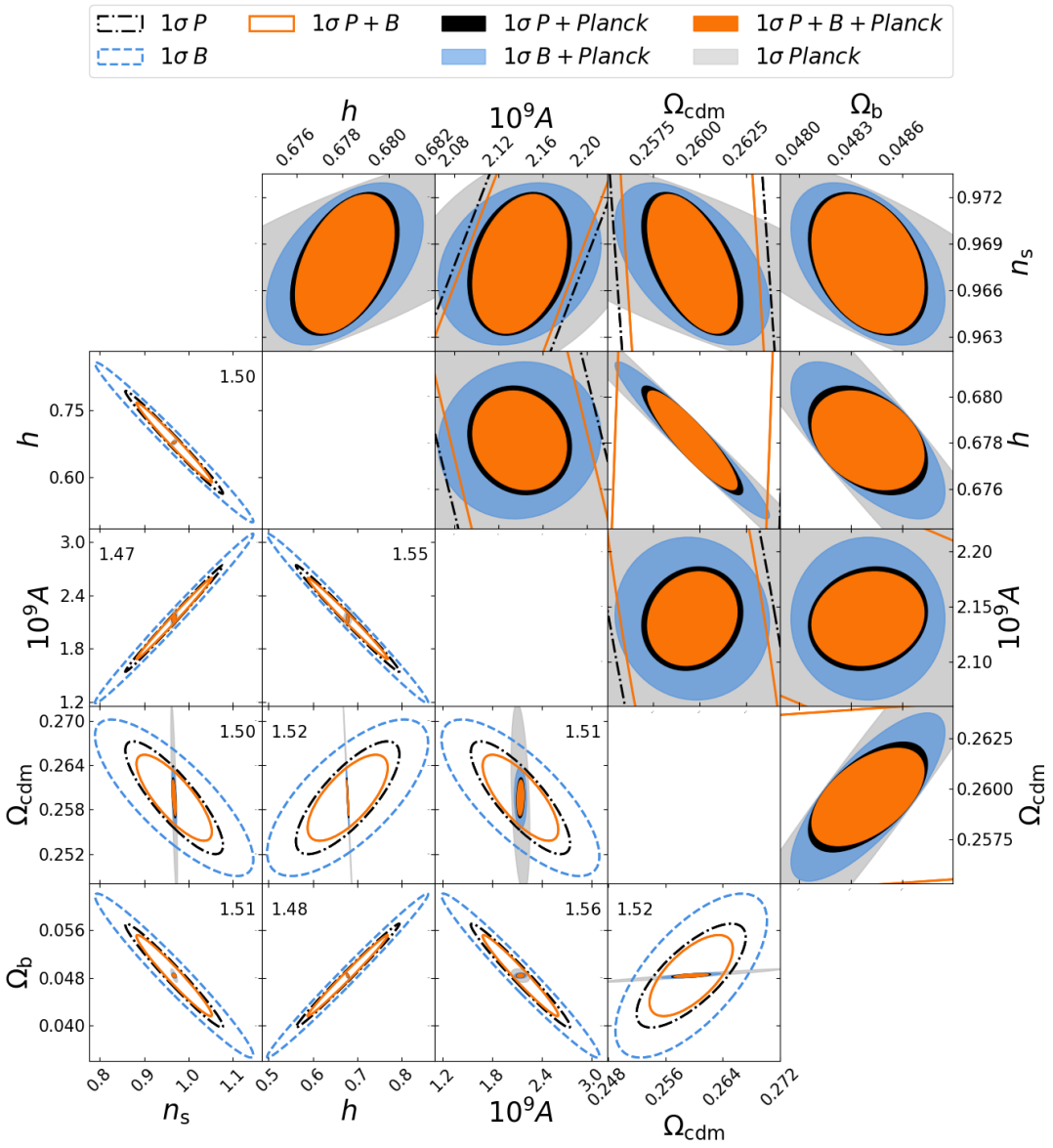

Figure 2.5: Joint 68.3 per cent credible regions for all pairs of cosmological parameters of the ΛCDM model. Different linestyles indicate the forecast for a *Euclid*-like survey based on different observables: namely, the power spectrum (dot-dashed), the bispectrum (dashed), and their combination (solid). The numbers indicate the ratio between the areas enclosed within the dot-dashed and the solid lines. The shaded areas highlight the credible regions obtained by also considering the *Planck* priors introduced in Section 2.3.6. The colour coding is indicated by the top labels. The panels below the diagonal offer a panoramic view while those above the diagonal zoom in for a close up of the central regions.

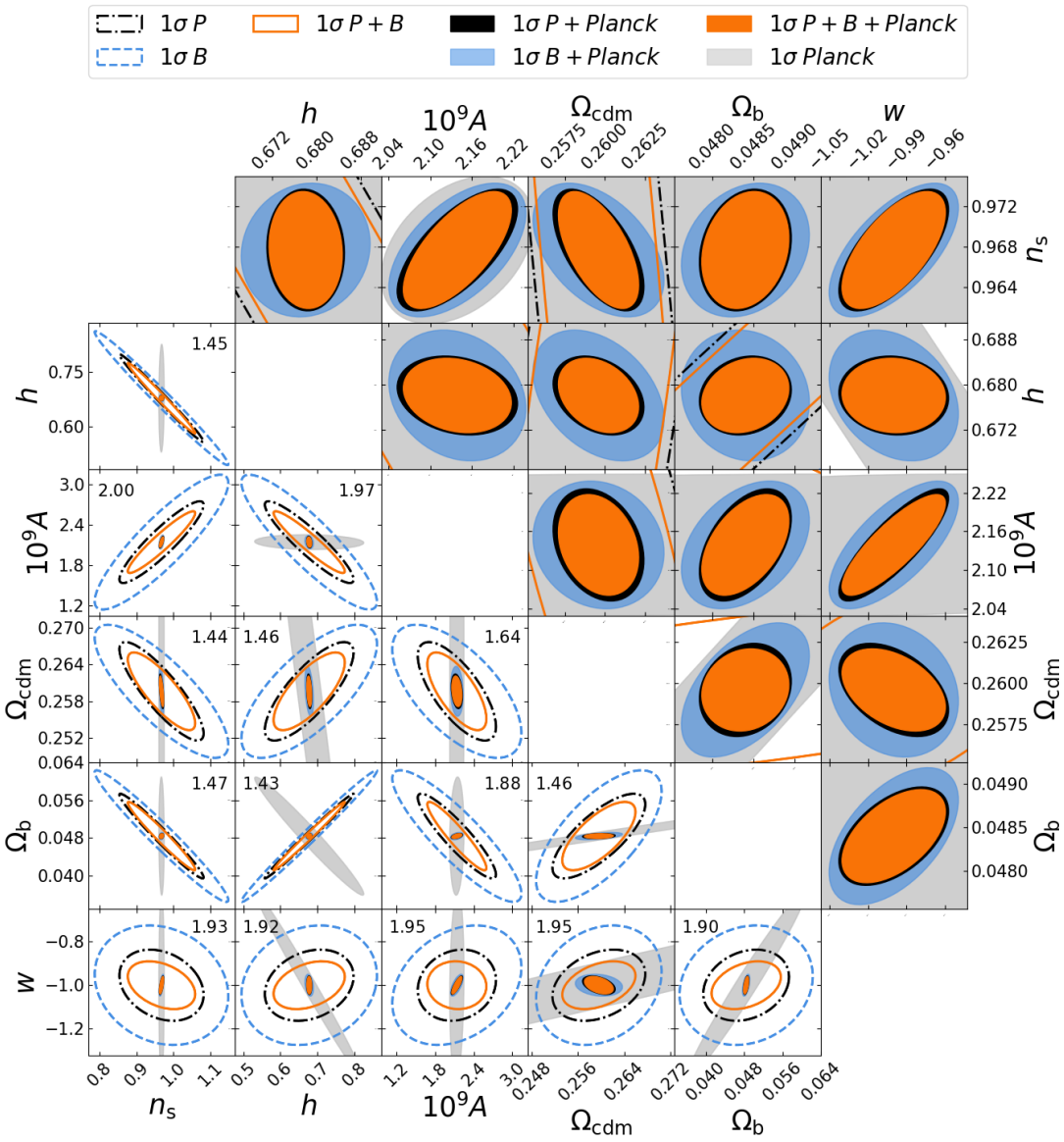

Figure 2.6: As in Fig. 2.5 but for the *w*CDM model.

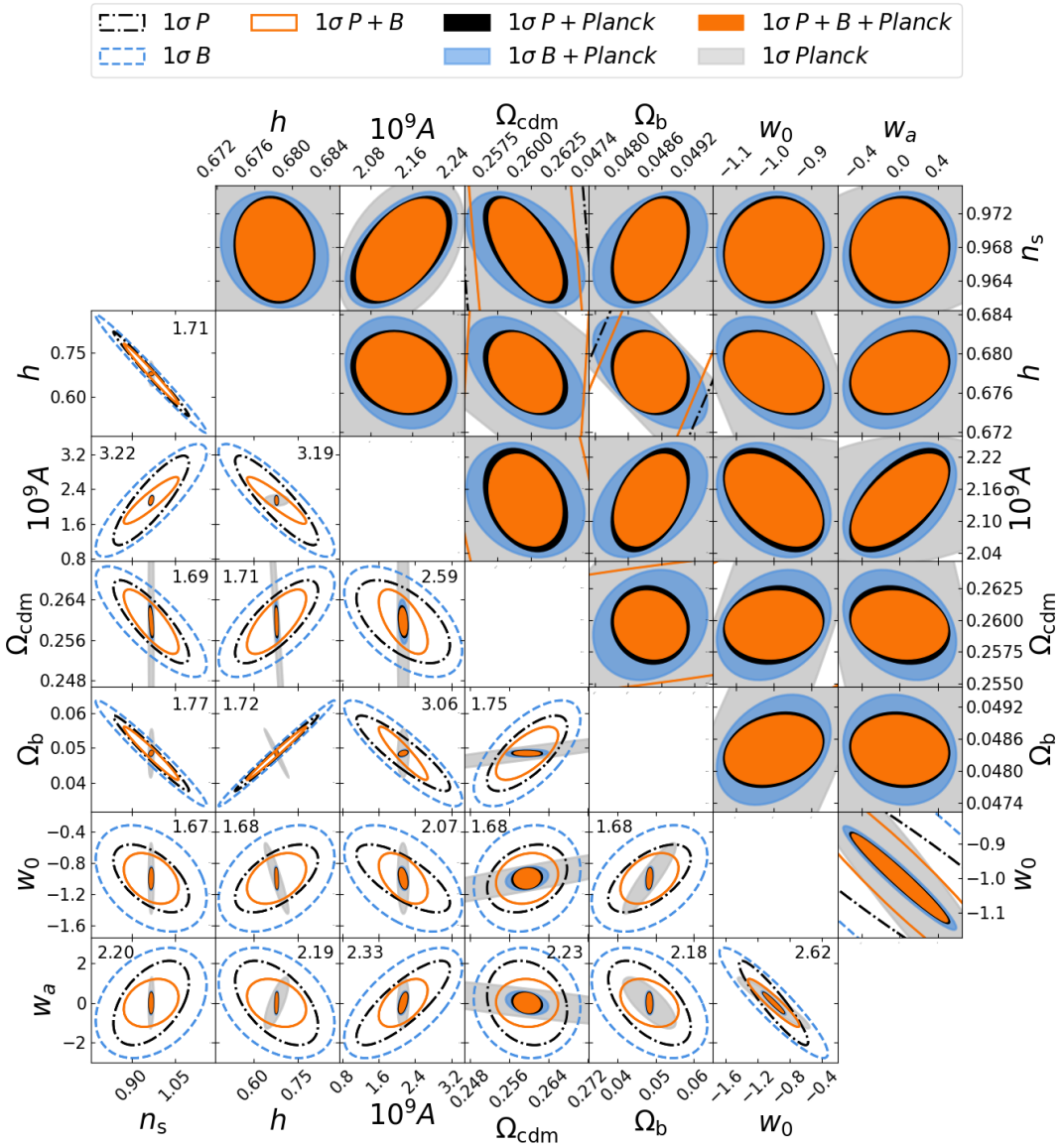

Figure 2.7: As in Fig. 2.5 but for the $w_0 w_a$CDM model.

are clearly distinguishable from noise with high confidence (note that this is not true for the single triangular configurations of the bispectrum whose measurement, given our narrow bins in k, is almost always dominated by noise). The global S/N, however, rapidly drops for $z > 1.2$ mainly due to the decreasing galaxy number density. In spite of the very large number of triangular configurations, we consider that the S/N ratio for B is always a factor of 2.5-3 times smaller than for P. Finally, we note that neglecting the cross-covariance between P and B, as in some previous studies (e.g. Karagiannis et al., 2018), only slightly overestimates the total S/N at the lowest redshifts (see also Song et al., 2015). This is a consequence of the fact that we only consider quasi-linear scales where P and B are weakly correlated. The differences become more marked if the analysis is extended to smaller scales (Byun et al., 2017; Chan & Blot, 2017).

2.4.2 Cosmological parameters

In Figs. 2.5, 2.6, and 2.7, we show the results of our forecasts for the ΛCDM, wCDM and w_0w_aCDM models, respectively. Shown are the joint 68.3 per cent credible regions for all possible pairs of cosmological parameters obtained after marginalizing over all the remaining model parameters. The bottom-left area of the figures is tailored to display the likelihood contours obtained from a *Euclid*-like survey. Dot-dashed, dashed, and solid lines show the constraints coming from the galaxy power spectrum, the bispectrum, and their combination, respectively. In each panel, we report the ratio between the areas enclosed within the dot-dashed and the solid curves. These numbers show that the benefit of combining two- and three-point statistics becomes more marked for the models that include a larger number of free parameters as there are more degeneracies to break. On the other hand, the narrow-shaded regions highlight the credible regions obtained by also considering the *Planck* priors introduced in Section 2.3.6. The top-right areas of the figures zoom in to display the combined results more clearly.

The corresponding marginalized errors for each single variable are reported in Table 2.3. In general, the bispectrum provides similar, but slightly worse, constraints than the power spectrum. Also, the orientation of the likelihood contours is very similar between the two probes. Therefore, the combination of these two- and three-point statistics leads to a non-negligible but moderate gain in the determination of the cosmological parameters.

Adding the *Planck* prior breaks degeneracies in the models by imposing strong constraints on n_s, A, as well as on various combinations of Ω_b, h. In consequence, the parameters that describe the dark-energy equation of state are determined much more precisely. Once combined with *Planck*, the galaxy power spectrum and the bispectrum give very similar constraints on the cosmological parameters. In this case, combining two- and three-point statistics provides only minimal advantages for the cosmology sector but yields a precise measurement of galaxy bias (see Section 2.4.3).

Table 2.3 also shows that the forecast obtained by neglecting the cross-covariance between P and B is only slightly optimistic with respect to the full analysis. This result validates previous studies that do not consider $\mathbf{C}_{\rm BP}$ (provided that they focus on sufficiently large scales). Note that the numerically challenging inversion of the covariance matrix in equation (2.52) becomes trivial when $\mathbf{C}_{\rm BP} = 0$.

2.4.3 Galaxy bias

Being able to accurately measure non-linear galaxy bias is considered one of the classic advantages of bispectrum studies. In Fig. 2.8, we present forecasts for the uncertainty with which an *Euclid*-like

Table 2.3: Expected marginalized 1σ errors (i.e. half of the 68.3 per cent credible-interval size) for the cosmological parameters in the ΛCDM, wCDM, and w_0w_aCDM models obtained considering a *Euclid*-like survey (left) and its combination with *Planck* priors (right). The different columns display results obtained from the galaxy power spectrum, P, the bispectrum, B, and their combination, $P + B$. We also show forecasts computed by neglecting the cross-covariance $\mathbf{C}_{\rm BP}$ that we indicate with the symbol $P \overset{\rm d}{+} B$. Note that, to ease the presentation of the results, the parameters have been rescaled by a multiplicative factor as indicated in the leftmost column of each sector. The bottom row gives the FoM for the dark-energy parameters w_0 and w_a.

	Euclid-like alone					*Euclid*-like with *Planck* prior			
	P	B	$P \overset{\rm d}{+} B$	$P + B$		P	B	$P \overset{\rm d}{+} B$	$P + B$
					ΛCDM				
$10\,n_{\rm s}$	0.72	1.17	0.53	0.56	$10^3\,n_{\rm s}$	3.02	3.43	2.91	2.93
$10\,h$	0.76	1.19	0.56	0.59	$10^3\,h$	1.55	2.24	1.38	1.41
$10^{10}A$	3.95	6.28	2.87	3.01	$10^{11}A$	3.09	4.86	2.60	2.80
$10^3\,\Omega_{\rm cdm}$	5.01	6.96	3.56	3.82	$10^3\,\Omega_{\rm cdm}$	1.79	2.73	1.54	1.58
$10^3\,\Omega_{\rm b}$	5.71	9.02	4.26	4.46	$10^4\,\Omega_{\rm b}$	2.27	2.94	2.12	2.14
					wCDM				
$10\,n_{\rm s}$	0.75	1.19	0.56	0.60	$10^3\,n_{\rm s}$	3.96	4.35	3.78	3.81
$10\,h$	0.79	1.21	0.59	0.63	$10^3\,h$	4.61	7.64	4.27	4.35
$10^{10}A$	3.99	6.58	2.87	3.01	$10^{11}A$	5.73	6.52	5.08	5.14
$10^3\,\Omega_{\rm cdm}$	5.28	7.14	3.83	4.17	$10^3\,\Omega_{\rm cdm}$	1.86	2.68	1.61	1.64
$10^3\,\Omega_{\rm b}$	5.87	9.13	4.45	4.74	$10^4\,\Omega_{\rm b}$	3.69	5.13	3.45	3.49
$10\,w$	1.07	1.80	0.71	0.72	$10^2\,w$	2.80	3.30	2.61	2.64
					w_0w_aCDM				
$10\,n_{\rm s}$	0.86	1.26	0.58	0.62	$10^3\,n_{\rm s}$	4.13	4.52	3.92	3.96
$10\,h$	0.93	1.30	0.62	0.66	$10^3\,h$	2.78	3.74	2.65	2.67
$10^{10}A$	6.78	8.55	3.48	3.54	$10^{11}A$	6.32	7.07	5.62	5.67
$10^3\,\Omega_{\rm cdm}$	5.37	7.16	3.83	4.17	$10^3\,\Omega_{\rm cdm}$	2.00	2.85	1.71	1.77
$10^3\,\Omega_{\rm b}$	7.12	9.99	4.75	5.02	$10^4\,\Omega_{\rm b}$	4.59	6.81	4.21	4.26
$10\,w_0$	2.85	4.47	2.00	2.13	$10^2\,w_0$	8.61	9.88	8.28	8.38
w_a	1.40	1.83	0.78	0.79	$10\,w_a$	3.40	3.88	3.26	3.29
FoM(w_0w_a)	6.66	3.03	18.10	17.43	FoM(w_0w_a)	147.06	93.32	166.71	162.49

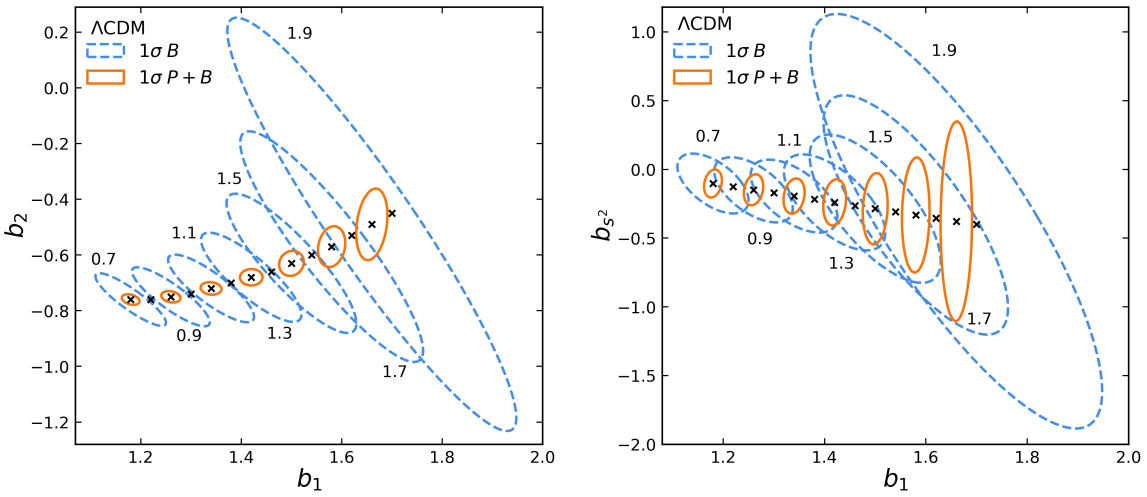

Figure 2.8: Joint 68.3 per cent credible regions for pairs of bias parameters determined using the bispectrum (dashed) and the combination between the power spectrum and the bispectrum (solid) for a *Euclid*-like survey. To improve readability, we mark with crosses the fiducial values for all redshift bins but we show the credible regions only for alternate bins. The mean redshift for the sample increases from left to right. The numerical labels indicate the central value of each redshift bin and are located in proximity of the corresponding contours to help identify them.

survey can determine the bias parameters in a ΛCDM model (results are similar for the other cases considered in this chapter). The bispectrum provides tight constraints on the bias coefficients at low redshift but it does not contain enough information to uniquely determine them at higher redshifts where estimates of b_1 and b_2 (and, to a lesser degree, b_1 and b_{s^2}) are degenerate. Simultaneously fitting the power spectrum and the bispectrum strongly improves the situation. In fact, the power spectrum more tightly constraints b_1 (see also Fig. 2.9) and this is enough to break the degeneracies with b_2 and b_{s^2}. Combining the two probes, leads to even smaller b_1 errors, especially for the w_0w_aCDM model (rightmost panel in Fig. 2.9). It is worth stressing that, in a power-spectrum study, the error on b_1 correlates with that on most cosmological parameters while cosmology-bias cross-correlations are weaker for the bispectrum.

Fig. 2.8 shows that the combination of power spectrum and bispectrum should provide rather tight constraints in the (b_1, b_2, b_{s^2}) space that could be used to derive the halo occupation properties of the galaxies. In fact, empirically measuring deterministic relations between b_1 and b_2 as well as between b_1 and b_{s^2} would shed light on the nature of the biasing process. For instance, measuring a negative b_{s^2} at all redshifts in accordance with equation (2.43) would provide evidence in favour of a local biasing process in Lagrangian space.

2.4.4 Figure of merit for dark-energy constraints

Since the report of the DETF (DETF, Albrecht et al., 2006), it is customary to compare cosmological probes in terms of a conveniently defined FoM, i.e. a single number summarizing the strength of the

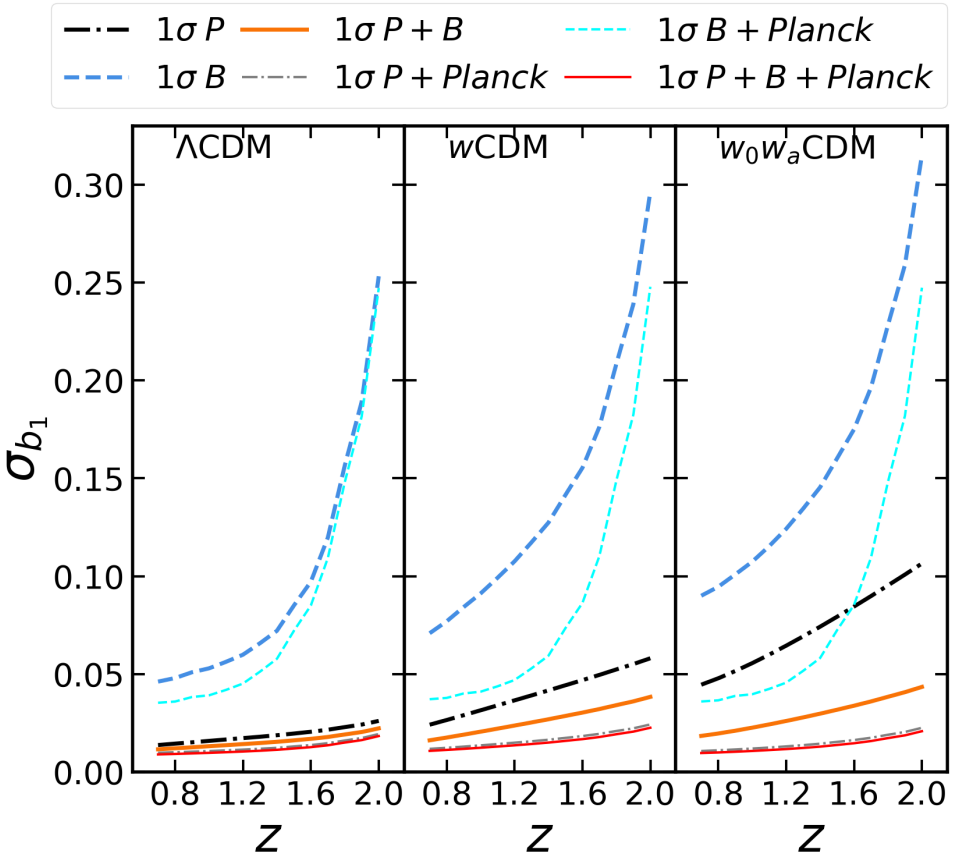

Figure 2.9: Forecast 1σ errors for the linear bias parameter as a function of redshift. Shown are the results for a *Euclid*-like survey (with and without *Planck* priors) based on the galaxy power spectrum (dot-dashed), the bispectrum (dashed), and their combination (solid). Line style and thickness are indicated by the top labels.

constraints that can be set on to the model parameters that describe dynamic dark energy. For the w_0w_aCDM model, we adopt the definition (Wang, 2008; Mortonson et al., 2010)

$$\mathrm{FoM} = \frac{1}{\sqrt{\det \mathrm{Cov}(w_0, w_a)}}, \tag{2.56}$$

where $\mathrm{Cov}(w_0, w_a)$ denotes the 2×2 covariance matrix for the errors on w_0 and w_a (note that our definition is a factor of 6.17π larger than the DETF FoM that is defined as the reciprocal of the area in the w_0-w_a plane that encloses the 95 per cent credible region). Our results are reported in the last row of Table 2.3. We find that the galaxy power spectrum in a *Euclid*-like survey gives an FoM that is more than two times larger than for the bispectrum. However, combining two- and three-point statistics improves the FoM by a factor of 2.6 with respect to considering the power spectrum only[4]. This promising result is, however, weakened by considering the current CMB+clustering constraints as a prior. In this case, adding the bispectrum only improves the FoM by 11 per cent. The reason

[4] The corresponding factors for other combinations of cosmological parameters can be directly read in the bottom left-hand panels of Figs. 2.5, 2.6, and 2.7.

for this behaviour is as follows. The improvement for the *Euclid* data mainly derives from partially breaking the degeneracy between b_1 and the amplitude of P and B for all redshift bins. As we have shown in the previous Section, combining P and B allows a much better determination of the linear bias parameters at all redshifts (the marginalized errors shrink by a factor between 2 and 3). These 14 parameters are degenerate with the amplitudes of the clustering signals that depend on both A and the linear growth factors (thus on w_0 and w_a)[5]. Once the *Planck*'s data are taken into consideration, A is extremely well determined and the constraints on b_1, w_0 and w_a do not improve significantly by adding the galaxy bispectrum to the power spectrum.

2.5 Discussion

In this section, we study how modifications to our standard setup influence the forecast results. For simplicity, we only consider the ΛCDM model and focus on the redshift bin centred at $z = 1$.

2.5.1 Dependence on the bin width Δk

So far, we have presented results obtained using narrow wavenumber bins with $\Delta k = k_\mathrm{f}$. This choice is motivated by the trade-off between minimizing information loss and taking into account the effect of the window function of the survey. However, it is difficult to imagine that such narrow bins will be ever used in actual observational studies. This is mainly because the large dimensionality of the data makes the estimation of covariance matrices prohibitive, at least when it is done using a large number of mock galaxy catalogues. Here, we quantify the influence of the bin size Δk on the forecast results. As a measure of information content, we generalize the definition of FoM given in equation (2.56) and write

$$\mathrm{FoM} = \frac{1}{\sqrt{\det \mathrm{Cov}(p_1, \ldots, p_n)}}\,, \tag{2.57}$$

where $(p_1, \ldots, p_n)$ denotes the set of model parameters that belong to a given sector (e.g. 'cosmology', 'bias', etc.). Note that the quantity $\mathrm{FoM}^{1/n}$ gives an effective error estimate for a single parameter. In Fig. 2.10, we illustrate how the forecast constraints from the analysis of the power spectrum and the bispectrum degrade as the size of Δk increases. Shown is the ratio $\mathrm{FoM}^{1/n}(\Delta k)/\mathrm{FoM}^{1/n}(\Delta k = k_\mathrm{f})$ that provides an indication of the mean information loss per model parameter and allows us to easily compare results obtained for different sectors. In all cases, the deterioration of the constraints with increasing Δk is noticeable. For instance, using $\Delta k = 5k_\mathrm{f}$ typically leads to error bars on the model parameters that are 20 per cent larger than in our reference case. Note that the recent analysis of the bispectrum monopole from the BOSS DR12 CMASS[6] sample (Gil-Marín et al., 2017) adopts $\Delta k = 6k_\mathrm{f}$ due to the limited number of mock catalogues available to estimate the covariance matrix. It is only by compressing the data vector with the Karhunen-Loève transform that Gualdi et al. (2018) could employ thinner k-bins down to $\Delta k = 2k_\mathrm{f}$.

[5] We have checked that, if the linear bias coefficients are kept fixed at their fiducial value, the FoM for the dark-energy parameters only improves by a factor of 1.25 when P and B are combined.

[6] Baryon Oscillation Spectroscopic Survey (BOSS), data reliase 12 (DR12), constant mass (CMASS)

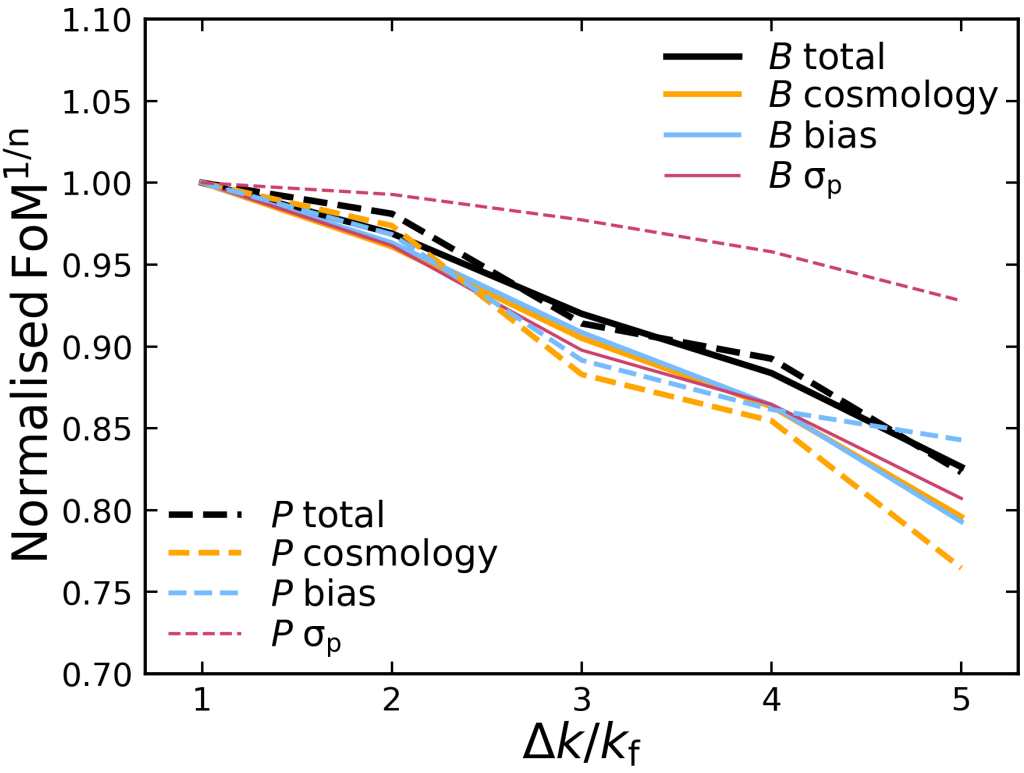

Figure 2.10: Typical information loss per model parameter as a function of the bin size Δk. Shown is the function $\mathrm{FoM}^{1/n}(\Delta k)$ normalized to one at $\Delta k = k_\mathrm{f}$ (the value we used in Section 2.4). Results for the power spectrum and the bispectrum measured from a *Euclid*-like survey at $0.95 < z < 1.05$ are shown with dashed and solid lines, respectively. Model parameters are grouped in different sectors as indicated by the labels. The figure refers to the ΛCDM model.

2.5.2 Dependence on k_max

The results presented in Section 2.4 have been obtained considering all Fourier modes with $k < k_\mathrm{max} = 0.15\,h\,\mathrm{Mpc}^{-1}$. This choice was dictated primarily by theoretical limitations. In fact, it is challenging to develop models for the galaxy bispectrum in redshift space that are sufficiently accurate on smaller scales. However, it is difficult to draw a precise line that marks where models lose their predictive power. For this reason, here we explore how the Fisher-matrix forecast depends on the choice of k_max. An alternative approach would be to include 'theoretical errors' in the likelihood and extend the analysis to large wavenumbers (Baldauf et al., 2016). Though, this would force us to always deal with impractically large covariance matrices and, also, assumptions would have to be made in order to estimate the size of the theoretical errors for the bispectrum in redshift space. For these reasons, we prefer to use the more traditional method of varying k_max. Our results are presented in Fig. 2.11. For the cosmology sector, the quantity $\mathrm{FoM}^{1/n}$ scales as k_max^α with $\alpha \simeq 2.7$ for the power spectrum and $\alpha \simeq 3.6$ for the bispectrum. If these scaling properties can be extrapolated beyond $0.2\,h\,\mathrm{Mpc}^{-1}$, our

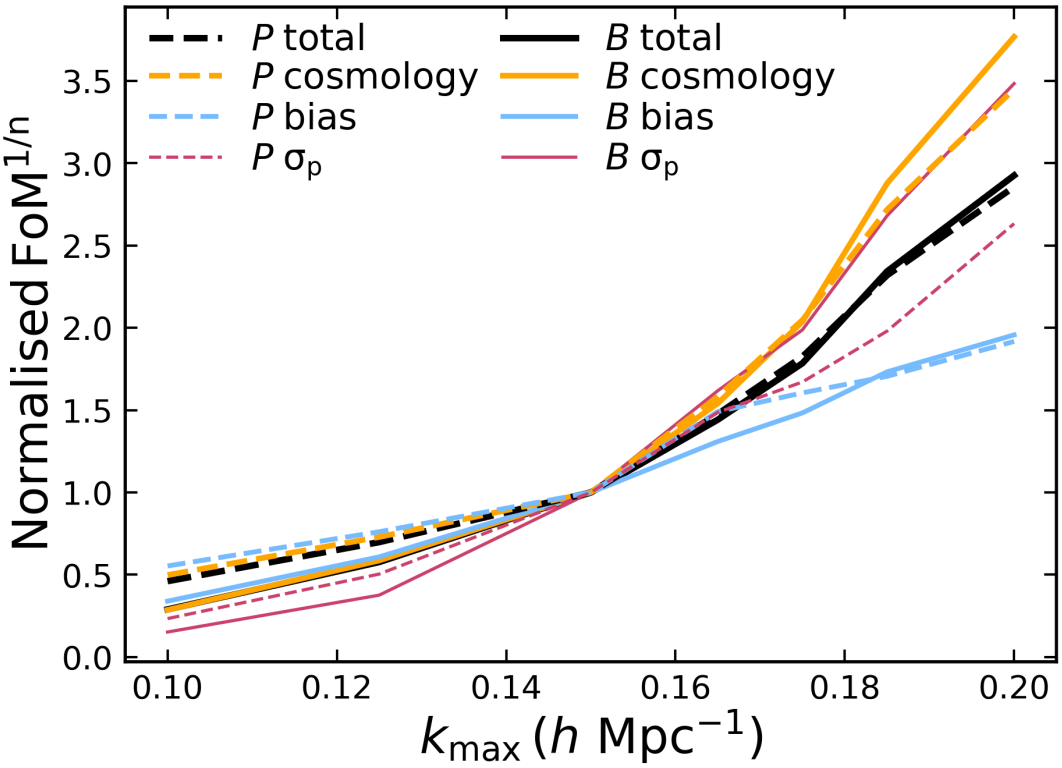

Figure 2.11: As in Fig. 2.10 but as a function of $k_{\rm max}$.

results imply that the bispectrum will achieve the same constraining power as the power spectrum for $k_{\rm max} \sim 0.43\,h\,{\rm Mpc}^{-1}$.

2.5.3 Binning of triangle orientations

In Fig. 2.12, we investigate how the quantity ${\rm FoM}^{1/n}$ depends on the number of bins used to describe the orientation of the triangular configurations for the bispectrum with respect to the line of sight. For simplicity, we only show results for the complete fit including all cosmological and nuisance parameters (that we labelled 'total' in Figs. 2.10 and 2.11) as the individual plots for the different sectors all appear very similar. The first important thing to mention is that just considering the monopole of the bispectrum in redshift space (i.e. $N_{\tilde{\phi}} = N_{\tilde{\mu}_1} = 1$) leads to a non-negligible loss of information. In this case, individual parameter constraints degrade, on average, by ~ 30 per cent with respect to our reference case ($N_{\tilde{\phi}} = 2$, $N_{\tilde{\mu}_1} = 4$). Taking into account the lowest-order non-vanishing multipoles with $m = 0$ (i.e. setting $N_{\tilde{\phi}} = 1$ but $N_{\tilde{\mu}_1} > 1$) is already enough to recover most of the lost information (see also Gagrani & Samushia, 2017). However, it is necessary to also consider the variation of the bispectrum with respect to the azimuthal angle in order to further shrink the parameter constraints by 7 (for B) and 1.5 (for P and B combined) per cent. Note that our reference case represents a good compromise between minimizing the number of bins and keeping most of the

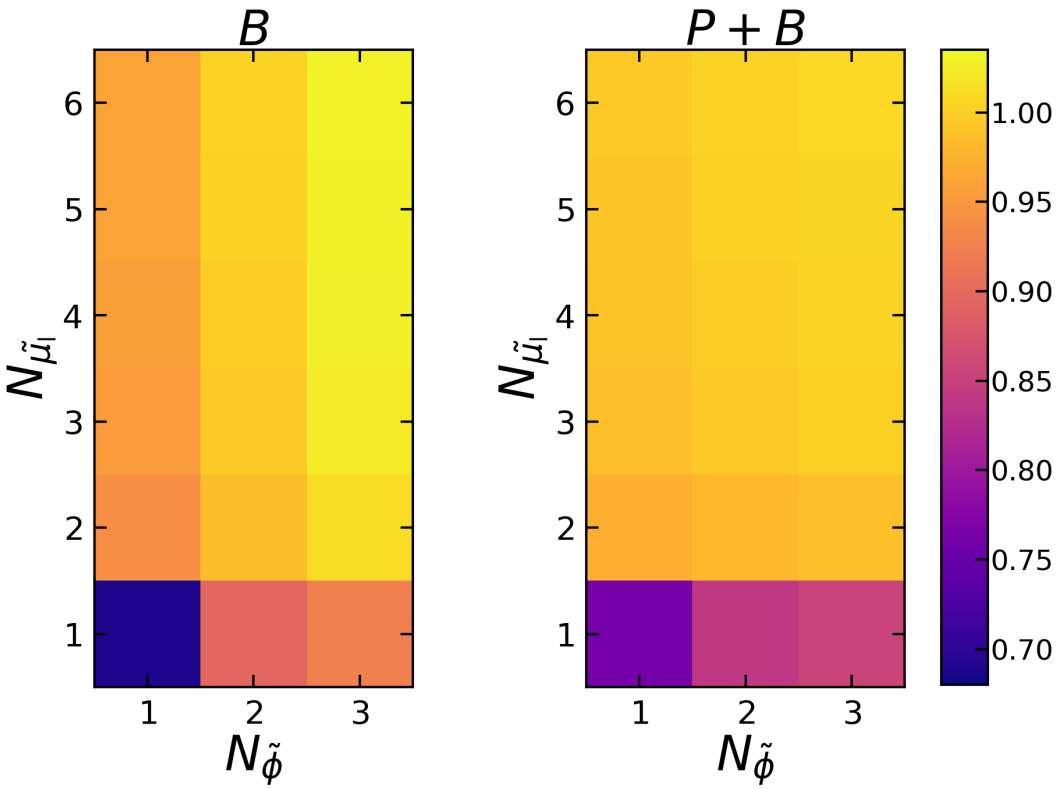

Figure 2.12: As in Fig. 2.10 but as a function of the number of bins used to describe the orientation of the triangular configuration of wavevectors with respect to the line of sight. Here, $N_{\tilde{\phi}}$ and $N_{\tilde{\mu}_1}$ denote the number of bins in the azimuthal angle $\tilde{\phi}$ and in the cosine of the polar angle $\tilde{\theta}$ (measured with respect to the longest wavevector), respectively. Shown is the quantity $\mathrm{FoM}^{1/n}$ evaluated for a generic $(N_{\tilde{\phi}}, N_{\tilde{\mu}_1})$ pair divided by the value it assumes for our reference case $N_{\tilde{\phi}} = 2$ and $N_{\tilde{\mu}_1} = 4$.

information contained in the data.

2.5.4 Shot-noise subtraction

In line with previous theoretical work (e.g. Sefusatti et al., 2006; Song et al., 2015; Gualdi et al., 2018), the results presented in Section 2.4 quantify the cosmological dependence of the actual galaxy-clustering signal and thus assume that we can perfectly subtract the systematic shot-noise contributions to the power spectrum and the bispectrum. In a real survey, however, the mean galaxy density and the shot-noise corrections can only be estimated with some uncertainty (e.g. by using the selection function and the mask, Feldman et al., 1994; Scoccimarro, 2000, 2015). Moreover, it is reasonable to expect that shot noise is not exactly Poissonian as evidenced by the analysis of mock catalogues based on N-body simulations (e.g. Mo & White, 1996; Hamaus et al., 2010; Baldauf et al., 2013). Therefore, various approaches have been taken in the literature to generalize equations (2.25) and (2.26). For instance, in their analysis of the BOSS survey, Gil-Marín et al. (2014) rescale the shot-noise terms

$P'_{\rm shot}$ and $B_{\rm shot}$ by the same constant factor that is then fit to the data. Similarly, Schmittfull et al. (2015) use two scale-independent factors to correct $P'_{\rm shot}$ and $B_{\rm shot}$ in order to fit the bispectrum of dark-matter haloes extracted from N-body simulations. This phenomenological approach can be motivated by writing a more general bias expansion that includes stochastic contributions (e.g. Dekel & Lahav, 1999; Matsubara, 1999; Angulo et al., 2015; Senatore, 2015; Desjacques et al., 2018, and references therein). In this case, the term $\epsilon(\boldsymbol{x}) + \epsilon_1(\boldsymbol{x})\delta(\boldsymbol{x})$ should be added to the right-hand side of equation (2.17). Here, ϵ denotes the leading stochastic contribution to the bias relation while ϵ_1 is the random part of the linear bias. By definition, both these fields have zero mean. Within these assumptions, it is straightforward to show that the power spectrum and the bispectrum of ϵ replace $P_{\rm shot}$ and $B_{\rm shot}$ in equations (2.25) and (2.26), respectively. On the other hand, the cross-spectrum between ϵ and ϵ_1 takes the place of $P'_{\rm shot}$ in equation (2.26). A popular strategy is to assume that, on large scales, these terms are approximately constant and somewhat close to the predictions of Poisson sampling. In this Section, we explore the consequences of considering $P_{\rm shot}$, $P'_{\rm shot}$, and $B_{\rm shot}$ as three additional free parameters (using the fiducial values $n_{\rm g}^{-1}$, $n_{\rm g}^{-1}$, and $n_{\rm g}^{-2}$, respectively). The same approach has been adopted by Karagiannis et al. (2018) to study the constraining power of the galaxy bispectrum on primordial non-Gaussianity.

For the power spectrum, we find that fitting the amplitude of the additional white noise term, $P_{\rm shot}$, worsens the constraints on all cosmological parameters by between 21 and 32 per cent (the worst case being for $n_{\rm s}$) while basically leaves the errors on b_1 and $\sigma_{\rm p}$ unchanged.

A quick look at equation (2.26) shows that the situation is more complex for the bispectrum as the shot-noise contribution also contains a scale-dependent part that is proportional to the sum of three power spectra. For this reason, if we repeat the forecast presented in Section 2.4 by taking into account shot noise and assuming that (i) equation (2.26) exactly applies and (ii) we perfectly know $\bar{n}$, then most of the constraints on the fit parameters improve. The largest upgrades take place for $\Omega_{\rm cdm}$ (66 per cent), $n_{\rm s}$ (47 per cent), and A (44 per cent) while the smallest one applies to $\sigma_{\rm p}$ (30 per cent). Only the marginalized constraints in the non-linear bias parameters get slightly worse (by 7 per cent for b_2 and by 3.5 per cent for b_{s^2}).

We can now relax assumptions (i) and (ii) above by replacing $n_{\rm g}^{-1}$ and $n_{\rm g}^{-2}$ in equation (2.26) with two independent free parameters, $P'_{\rm shot}$ and $B_{\rm shot}$, that are then fit to the data including shot noise. After marginalizing the posteriors over $P'_{\rm shot}$ and $B_{\rm shot}$, we find that the constraints on b_{s^2} and $\sigma_{\rm p}$ worsen by nearly 50 and 30 per cent, respectively, compared with our reference case while those on the cosmological parameters improve nearly as much as in the example discussed in the previous paragraph.

Similar outcomes are found when we combine the power spectrum and the bispectrum: the constraint on $\Omega_{\rm cdm}$ improves by 55 per cent with respect to the corresponding reference case in Table 2.3, those on $n_{\rm s}$ and A by nearly 30 per cent, while the error on b_2 increases by a factor of 3. This happens because b_2 is degenerate with $B_{\rm shot}$. Using the *Planck* prior mitigates the differences. In this case, the uncertainties for all fit parameters deteriorate by less than 30–40 per cent with respect to the corresponding reference case.

The tests presented above have been performed at $z = 1$ where the systematic shot-noise contribution is ~ 10 per cent of the actual clustering signal for both P and B. Of course, the impact of shot noise becomes more marked at higher redshifts were the number density of galaxies drops significantly. At $z \sim 2$, for instance, shot noise is comparable with the clustering signal.

Based on these results, we conclude that the treatment of shot noise in pure clustering studies (i.e. without external priors) has an impact on the resulting cosmological constraints and can alter them

significantly. The tests performed here also suggests that our main analysis might be conservative for parameters like $\Omega_{\rm cdm}$, $n_{\rm s}$, and A.

2.5.5 Treatment of galaxy bias

In our main analysis, we have used 3 bias parameters per redshift bin (for a total of 42) and fit them independently to the data. This is the safest approach as it does not rely on any other assumption than the bias expansion given in equation (2.17). However, it is reasonable to expect that the bias parameters change smoothly with redshift. In this case, it makes sense to approximate each of them with with a simple fitting function that captures their variation. We consider here a quadratic function of redshift for each bias coefficient. This reduces the number of nuisance parameters with respect to our standard treatment from 42 to 9. Our results show that implementing this simplified procedure does not give any practical advantage as the errors on the cosmological parameters basically remain unchanged with respect to our standard treatment.

2.6 Summary and conclusions

Galaxy clustering is a powerful cosmological probe. Two-point statistics in configuration and Fourier space are routinely used to constrain models for our Universe. The question addressed in this chapter is whether the galaxy bispectrum in redshift space contains additional information about the cosmological parameters.

The literature about the galaxy bispectrum mostly focuses either on the real-space statistic or on its redshift-space monopole. For this reason, in Section 2.3.2, we first illustrate the phenomenology of RSD for the bispectrum and explore different parameterizations for the spatial orientation of the triangles of wavevectors with respect to the line of sight. We then generalize the expressions found in the literature for the covariance matrix of bispectrum estimates and, in particular, for their cross-covariance with measurements of the power spectrum – see equation (2.42).

We use the Fisher information matrix to forecast constraints on a large number of cosmological and nuisance parameters from future measurements of the galaxy bispectrum and the power spectrum in redshift space. We consider flat FLRW models dominated by dark energy and CDM with Gaussian primordial perturbations. As an example of the forthcoming generation of experiments, we adopt the specifications of a *Euclid*-like galaxy redshift survey (Table 2.1). In our principal analysis, we only consider wavenumbers with $k \leq k_{\rm max} = 0.15\,h\,{\rm Mpc}^{-1}$ that define mildly non-linear scales on which fluctuations in the galaxy density can be treated perturbatively. Within this range, it should thus be possible to build robust models for the galaxy power spectrum and bispectrum. The main conclusions of our work are as follows:

(i) The galaxy bispectrum and the power spectrum in redshift space set constraints of similar strength on the cosmological parameters (Table 2.3). Therefore the bispectrum can be used as a consistency check for power-spectrum studies.

(ii) Posterior correlations between the model parameters derived from the bispectrum and the power spectrum are, in most cases, very similar (Figs. 2.5–2.7). For this reason, combining the two probes only moderately improves the cosmological constraints with respect to considering them individually.

(iii) For instance, considering both statistics together partially breaks the degeneracies between the linear bias coefficients and the galaxy-clustering amplitudes in all redshift bins. In consequence, the

FoM for the dark-energy parameters w_0 and w_a improves by a factor of 2.6 with respect to only using the power spectrum.

(iv) This advantage, however, vanishes once priors based on the results of the *Planck* mission and of current clustering studies are included in the analysis. In this case, combining the power spectrum with the bispectrum does not give any appreciable benefit other than precisely determining the parameters that describe galaxy bias.

(v) For wavenumbers $k < 0.15\,h\,\mathrm{Mpc}^{-1}$, the cross-covariance between the power spectrum and the bispectrum has a small influence on parameter estimation (Table 2.3) and may be safely neglected to first approximation.

(vi) Taking broad bins for the legs of the triangles of wavevectors leads to some information loss for the bispectrum (Fig. 2.10). For instance, using $\Delta k = 5k_\mathrm{f}$ gives cosmological constraints which are suboptimal by 20 per cent.

(vii) Since the number of bins in the triangular configurations for the bispectrum grows more rapidly with the maximum wavenumber than the number of bands in the power spectrum, the relative importance of the two probes strongly depends on the value of k_max that is considered (Fig. 2.11). We find that, for $k_\mathrm{max} = 0.15\,h\,\mathrm{Mpc}^{-1}$, the power spectrum provides slightly tighter constraints than the bispectrum on most parameters. However, our results also suggest that the bispectrum becomes the leading probe if the analysis is extended beyond $k_\mathrm{max} \simeq 0.43\,h\,\mathrm{Mpc}^{-1}$ (assuming that an accurate theoretical model is available at such wavenumbers).

(viii) RSD contain precious information about the cosmological parameters. Just considering the monopole moment of the bispectrum leads to a non-negligible loss of information. Individual error bars for the fit parameters typically grow by 50 per cent (Fig. 2.12). Taking into account the lowest-order non-vanishing multipoles with $m = 0$ recovers most of the lost information. Considering also variations of the bispectrum with the azimuthal angle further reduces the error bars by a few up to 10 per cent.

(ix) The way shot noise is handled in the clustering analysis influences the cosmological results (especially for Ω_cdm, n_s and A) as well as the non-linear bias parameter b_2. However, this dependence is significantly reduced by also considering CMB-based priors.

(x) Using a smooth function of redshift to describe the evolution of the bias coefficients does not lead to any practical advantage with respect to fitting individual parameters for every redshift bin.

CHAPTER 3

Binning effects on cosmological constraints from the bispectrum[1]

3.1 Introduction

The ultimate goal of many theoretical studies is to draw comparisons between predictions and observational data. For future missions, such as *Euclid*, it is important to have planned such a comparison well in advance of the actual data release. The actual observational data will be binned in some way and theoretical models should be adapted to this issue. Thirdly, the bispectrum binning method used in Chapter 2 (the full average of the wavevectors and the bispectrum) is computationally expensive. Usually, other approaches are used to increase the speed of calculations, which unfortunately comes at the cost of a loss in accuracy compared to using the full averaging. Additionally, the forecast results are dependent on the choice of bispectrum binning. A widely-used technique is to use one wavevector and respectively one value of the bispectrum per bin. This value can be taken to be the a middle of the bin, or on some 'effective' point. Also a choice of logarithmic wavevector scale may be used instead of a linear scale.

Therefore, in this Chapter we study several ways of the bispectrum binning. We compare the methods, discuss their advantages and disadvantages in dependence of the required task. Finally, we show how the binning strategy affects the forecast.

3.2 Method

In this Chapter we use the models of the redshift space power spectrum and the bispectrum, parameters of the *Euclid*-like survey, estimators for Fisher and covariance matrices, which were used in Chapter 2. However, here we present results only for the ΛCDM and the w_0w_aCDM cosmological models.

[1]The paper Yankelevich & Porciani, *Binning effects on cosmological constraints from the bispectrum* will be submitted to *Monthly Notices of the Royal Astronomical Society*.

3.3 Binning strategy

3.3.1 Average model

The first method of calculating the values of the power spectrum and bispectrum (refered to as the 'average') is the same as that discussed in Chapter 2. In this method, all possible wavevectors are generated within the range $[k_{\rm min}, k_{\rm max}]$. The values of the power spectrum are then calculated for each wavevector k, as are the bispectrum values for each set of three wavevectors $k_{\rm s}, k_{\rm m}, k_{\rm l}$, which form triangles. In this scenario, there are many different triangles which fall into the same triangular bin, each of them providing an associated value of the bispectrum. Finally, the wavevectors, power spectrum, and bispectrum are averaged for each bin (or triangular bin). Since we are working in the RSD framework, the same averaging process is performed for each of the parameters describing the spatial orientation: μ and μ_1, $\tilde{\phi}$.

There are three main advantages of this method. Firstly, it provides more accurate values of the power spectrum or the bispectrum, compared to those computed only at one set of k. Secondly, all types of triangles are automatically generated, including degenerate and non-closed triangles[1]. Thirdly, it is easy to incorporate a direct counter inside the code for generating the wavevectors. For example, for the number of modes per bin N_P and N_B, and for the number of overlapping bins between the power spectrum and the bispectrum for the full covariance combination I_{ijl} (for equation 2.42).

The main disadvantage of this method is its non-flexibility with respect to parameter changes. The power spectrum and the bispectrum have to be recomputed from scratch with every combination of parameters used in the model. Moreover, this method requires significant computational time, when compared to simpler methods (the actual amount of time depends on the language and structure of the code).

In the following study, we assume the results of this binning as the 'true' ones.

3.3.2 Middle of the bin method

The most straightforward method (here after called 'middle') is based on using only one characteristic configuration of wavevector per bin and respectively one value of the power spectrum and bispectrum. Here we use the bin center for each configuration. The indisputable advantages of the technique are speed and easy implementation. However, this method is approximate, and as we will show, is not accurate.

3.3.3 Effective method

The effective method (hereafter referred to as 'effective') is a hybrid between the average and middle of the bin techniques. Firstly, the wavevectors are generated and binned in the same way as the 'average' technique. These averaged values are the effective wavevectors for the following method. Then, like in 'middle' technique, values for the power spectrum and the bispectrum are calculated for each bin, using the characteristic configurations computed in the first step. The advantages of 'effective' compared to 'average' are the computational speed and the flexibility to input parameters changes. Since the characteristic values of wavevectors depend only on $k_{\rm min}$, $k_{\rm max}$ and Δk, they need to be

[1] For example, the configuration where wavevectors are $k_{\rm s} = 3.4$, $k_{\rm m} = 4.4$, $k_{\rm l} = 7.8$, but the triangular bin is $(3, 4, 8)$.

calculated only once. Also, as we will show, this technique yields a more accurate power spectrum and bispectrum than the 'middle' model.

3.4 Results

3.4.1 Signal-to-noise ratio

In Fig. 3.1, we plot the differences in S/N that are computed using the 'average', 'effective' and 'middle' techniques of calculating the power spectrum and the bispectrum as a function of redshift for a *Euclid*-like survey. To speed up the calculation, in this Chapter we use only the diagonal combination of the power spectrum and the bispectrum covariance matrix. For the bispectrum, the difference between methods ranges from 7 – 12 per cent, while the difference for the power spectrum and the combination is negligible. In the case of wider bins, $\Delta k \gg k_{\rm f}$, this effect will be larger.

3.4.2 Cosmological parameters

We present the forecast for cosmological parameters (marginalized over all redshift bins), for velocity dispersion and galaxy bias for $z = 1.0$ and for normalized FoM obtained with the *Euclid*-like survey. In Fig.3.2 it is shown the ratio for 1σ errors and FoM between the average, effective and middle of the bin methods for the forecast results for ΛCDM and w_0w_aCDM models for the power spectrum, the bispectrum and their combination.

The plot is divided into six main subsections by black bold lines. The first two (going from bottom to top) are the results for the power spectrum within the w_0w_aCDM model (first subsection) and within the ΛCDM model (second subsection). Similarly, the third and the fourth subsections show the bispectrum, and the fifth and the sixth present the combination of the power spectrum and the bispectrum. In all subsections, each row gives the ratio between the results of the two models. The first row I is the ratio between 'effective' and 'average'; the second row II is the ratio between 'middle' and 'average'; the third row III is the ratio of 'middle' and 'effective'. In general, for all cases, the biggest errors of cosmological parameters and accordingly smallest FoM is provided by the average method. These errors decrease moving to effective technique, and the smallest errors and the highest FoM are obtaining with the middle of the bin model. The differences in case I are smaller than in case II, and case III is significantly smaller than the others. Let us look in details on some elements. For example, for the parameter A obtained with the bispectrum, the relative difference between the methods is 10–14 per cent for the case I, and 18-22 for the case II. While for the velocity dispersion, the differences do not exceed 3 per cent. We can see, that the parameters, which affect the amplitude the power spectrum, e.g. A, w_0, w_a and b_1 are more sensitive to the way of the wavevector binning rather than the others. Particularly, in w_0w_aCDM model, because of a number of degeneracies between cosmological parameters.

In Fig.3.3, we present the results of our forecast for the dark energy equation of state parameters w_0w_a in the w_0w_aCDM cosmology for the average, effective and middle of the bin models. The likelihood contours obtained from a *Euclid*-like survey for the power spectrum (top-left subplot), the bispectrum (bottom-left) and their combination (bottom-right) are displayed. Dashed, dot-dashed, and solid lines show the 1σ constraints coming from the average, effective and middle of the bin methods, respectively. We also demonstrate in detail how the binning issue affects the forecast for galaxy bias parameters. In Fig. 3.4, the forecast for the tidal bias parameter b_{s^2} as a function of redshift is shown.

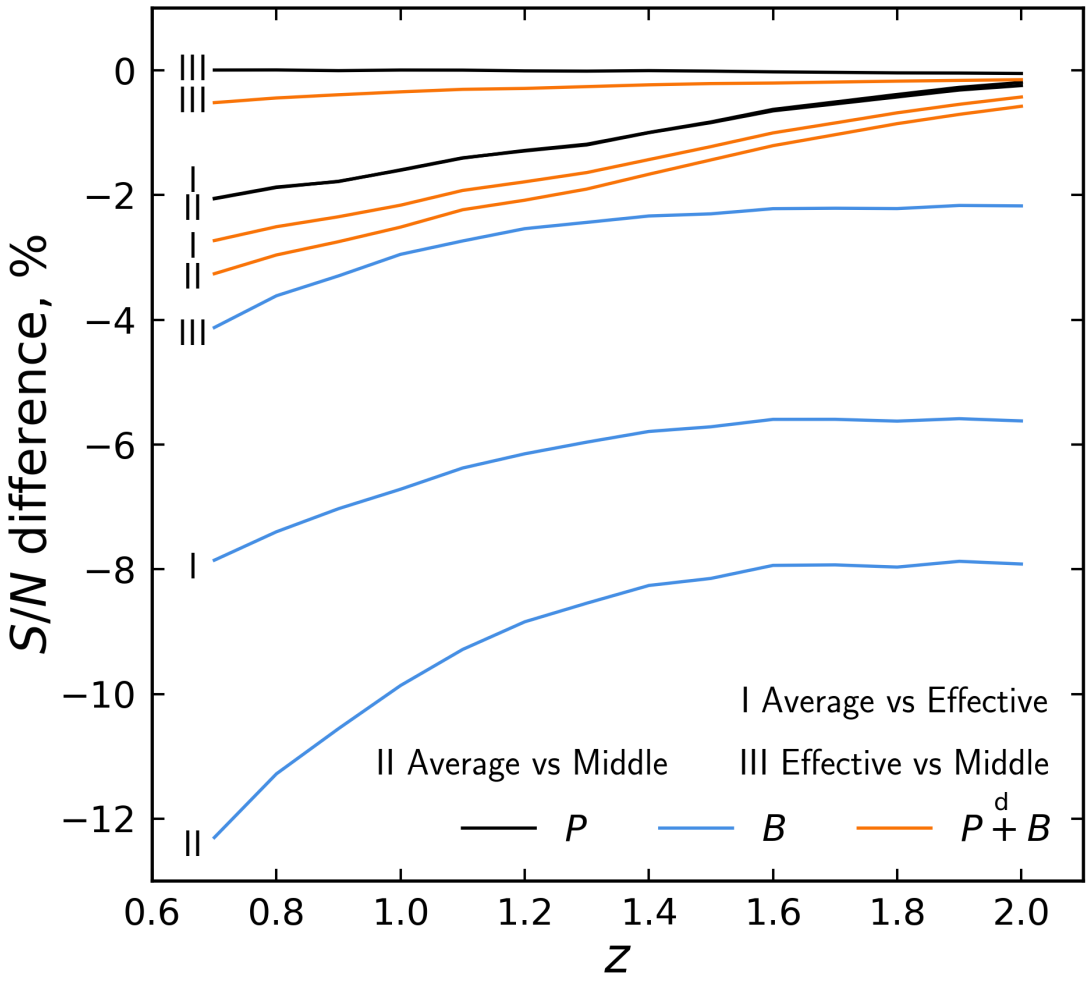

Figure 3.1: The difference in S/N for the average, effective and middle of the bin methods of calculating the power spectrum (black), the bispectrum (blue) and their diagonal combination (orange) in a *Euclid*-like survey as a function of redshift. We show the relative difference between average and effective (I), average and middle of the bin (II), effective and middle of the bin (III) methods.

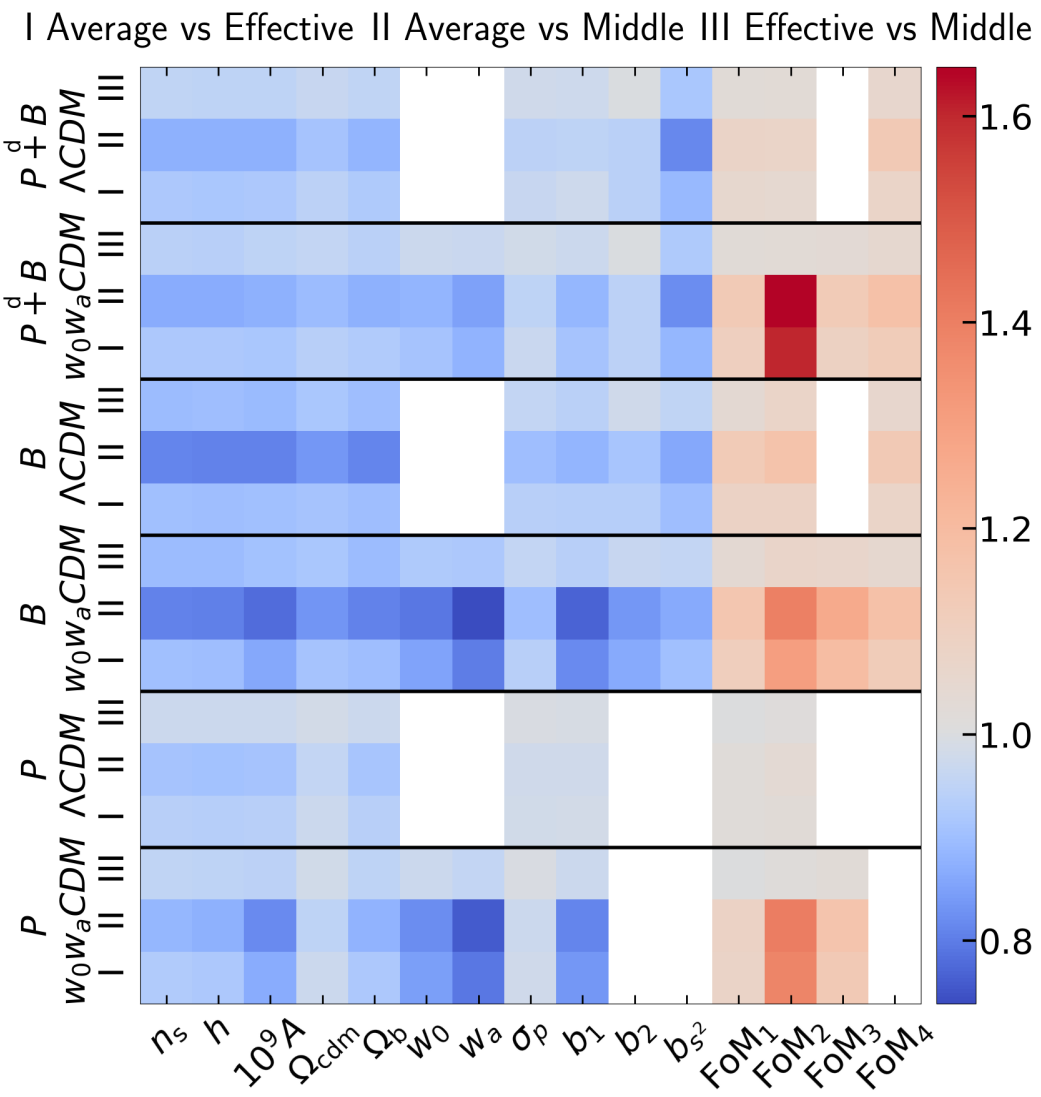

Figure 3.2: Comparison of the three methods to generate sets of wavenumbers for the power spectrum and the bispectrum. Shown is the ratio between 1σ errors for cosmological parameters and normalized FoM for ΛCDM and w_0w_aCDM models within the *Euclid*-like survey. The symbols for the FoM are the following: 1 – total set of parameters, 2 – cosmological parameters only, 3 – the dark-energy equation of state, 4 – galaxy bias. The legend of comparison is the same as in Fig. 3.1. The value of the ratio is shown by the colorbar.

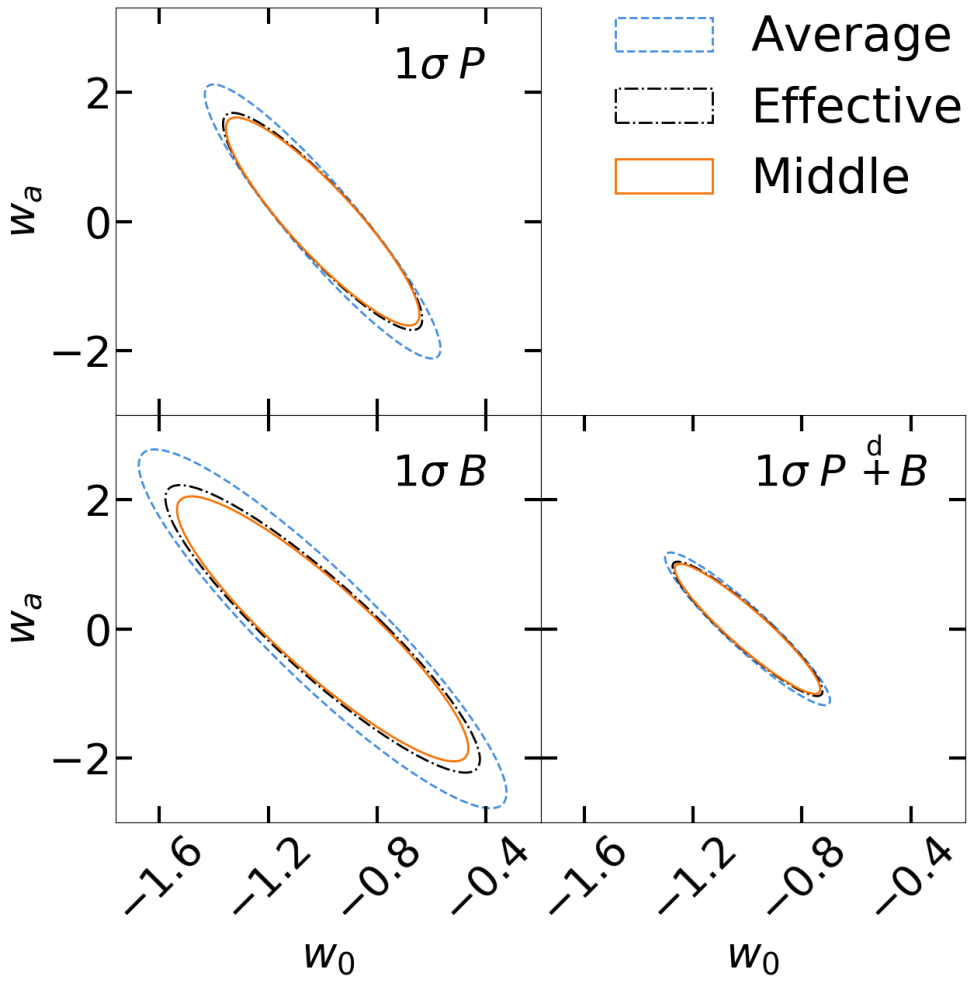

Figure 3.3: Joint 68.3 per cent credible regions for dark-energy equation of state parameters w_0 and w_a of the w_0w_aCDM model for average (dashed), effective (dot-dashed) and middle of the bin (solid) models. The subplots represent the power spectrum, the bispectrum and their diagonal combination forecast. A *Euclid*-like survey is assumed.

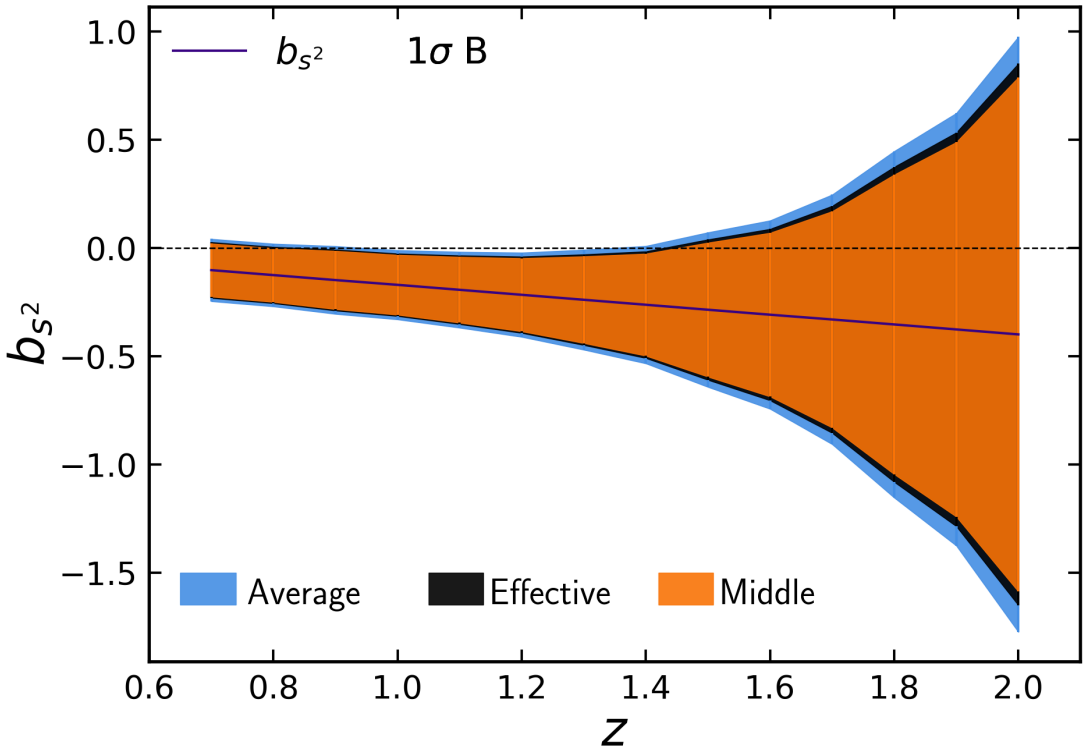

Figure 3.4: Forecast 1σ errors for the tidal bias parameter as a function of redshift. Shown are the results for a *Euclid*-like survey based on the galaxy bispectrum, calculated by three different binning techniques: 'average' (blue), 'effective' (black) and 'middle' (orange). The Purple solid line indicates the fiducial values of the tidal bias.

Presented are the 1σ errors for a *Euclid*-like survey based on the galaxy bispectrum, calculated by the three methods. The relative differences between the methods are about $9-11$ per cent and $13-15$ per cent for the comparison between 'average'-'effective' and 'average'-'middle' respectively.

In Table 3.1, we report the FoM for w_0 and w_a for the three techniques presented above. In general, the 'average' provides the smallest FoM compared to the 'effective' (1.21, 1.41, and 1.16 times smaller for the power spectrum, the bispectrum and, the combination, respectively) and the 'middle' (1.33, 1.60, and 1.27, accordingly) models. The FoM for average, effective and middle bin methods in combination with the *Planck* prior have minimal differences that do not exceed 10 per cent. Thus, the influence of the binning strategy only slightly affects the forecast obtained from combining results of the two probes.

Table 3.1: The FoM for the dark-energy parameters w_0 and w_a obtained considering a *Euclid*-like survey (left) and its combination with *Planck* priors (right) for average, effective and middle binning. The different columns display results obtained from the galaxy power spectrum, P, the bispectrum, B, and their diagonal combination, $P \overset{\mathrm{d}}{+} B$.

	Euclid-like alone			*Euclid*-like with *Planck* prior		
	P	B	$P \overset{\mathrm{d}}{+} B$	P	B	$P \overset{\mathrm{d}}{+} B$
Average	6.66	3.02	18.10	147.06	93.90	166.95
Effective	8.57	4.27	21.64	151.37	99.41	175.42
Middle	8.98	4.83	22.99	151.40	102.90	177.51

3.5 Discussion

In this section, we discuss how modifications to the average method influence the forecast results, in the case of a w_0waCDM model.

3.5.1 Dependence on the definition of the 'triangle bin'

In this chapter, for a 'triangle bin' we consider the configuration where the values of the bins satisfy the triangle inequality $i_\mathrm{s} + i_\mathrm{m} \geq i_\mathrm{l}$. Here we discuss how including non-closed triangular bins or excluding degenerate triangular bins can change the forecast results. If we exclude degenerate triangles, the total number of triangles decreases by 6 – 7 per cent, dependent on the redshift bin. Simultaneously, 1σ errors for cosmological parameters for the bispectrum B and the combination $P \overset{\mathrm{d}}{+} B$ increase by 4.5 – 13 per cent and 1–15 per cent respectively. Using a different approach, when one includes non-closed triangles (the bin configuration satisfies the condition $i_\mathrm{s} + i_\mathrm{m} + 1 \geq i_\mathrm{l}$), the total number of triangles increases by 5 – 6 per cent, and the 1σ errors for cosmological parameters decrease by 4.5 – 13 per cent for the bispectrum and 1 – 15 per cent for the combination of the power spectrum and the bispectrum. We used the same definition of the 'triangular bin' for the forecast presented in the Chapter 2.

3.5.2 Comparison of normal and log-scale binning

We also investigate the dependence of the obtained results on the choice of binning, from the fiducial case with $\Delta k = k_\mathrm{f}$ to log-scale where $\Delta \ln k = \ln\left(k_\mathrm{max}/k_\mathrm{min}\right)/N_\mathrm{bins}$.

Firstly, the 1σ errors for the cosmological parameters become larger. For example, for the power spectrum, for the parameters n_s, h, Ω_cdm, Ω_b and σ_p, errors increase by 2.6 – 8.8 per cent. Moreover, for the parameters which affect the amplitude of the power spectrum, e.g. A, w_0, w_a and b_1, there is a difference of 24, 37, 48, and 42 per cent respectively. Fortunately, in the case of the bispectrum, changes in the errors only increase by 2.5 to 14 per cent (for the w_a parameter). For the combination of the power spectrum and the bispectrum, the errors do not increase by more than 12 per cent (again, for the w_a parameter).

3.5.3 Dependence on the bin width Δk

In this chapter we always assume $\Delta k = k_\mathrm{f}$. This is the ideal case, which produces the most accurate forecast. However, the current observational data cannot be yet split in such narrow bins (see

Section 2.5.1). Future studies on the effect of the binning strategy on the galaxy bispectrum forecast for wider bins are needed.

3.6 Summary and conclusions

There are several ways of generating the sets of the wavevector for which the power spectrum and the bispectrum will be calculated. These methods have different advantages and disadvantages. The question addressed in this chapter is how the choice of the binning effects the forecast results. In many research, people use just one value of the wavevector per bin. This influences the results not in a positive way. Therefore, we recommend to use the average method of binning, as the most reliable from all models studied in the work.

The main conclusions of our work are as follows:

(i) The comparison of the average, effective and middle on the bin methods show 6 – 12 per cent difference for the S/N for the bispectrum. However, all methods give approximately the same S/N for the power spectrum and the joint probe up to 3 per cent level.

(ii) The cosmological parameters, which affect the amplitude of the power spectrum, are more sensitive to the way of the wavevector binning rather than the others.

(iii) The average method provides more conservative constraints on the FoM for w_0–w_a than the effective and middle of the bin cases. For instance, for the bispectrum the errors are 1.4 – 1.6 times bigger, for the combination probe they are bigger in 1.15 – 1.3 times. However, adding *Planck* priors smooths this effect below 10 per cent.

(iv) Including the non-closed triangles into the Fisher forecast helps improve the parameters constraints up to 15 per cent. On the contrary, excluding degenerate triangles results in the growth of errors up to 15 per cent.

(v) Using a log-scale binning leads to increasing 1σ errors for cosmological parameters up to 14 per cent for the bispectrum and up to 12 per cent for the combination probe. However, for the parameters determining the amplitude of the power spectrum significant changes (up to 49 per cent for w_a parameter) of the forecast result can happen.

(vi) The average method provide more accurate and more conservative forecast than the other methods..

CHAPTER 4

Conclusions and outlook

In the final chapter, we summarise the main results of this Ph.D. thesis. During this work, we studied the galaxy bispectrum, its properties, and the way to extract new cosmological information from it.

4.1 Summary of the projects and results

For years the bispectrum has been mentioned as a useful tool to study cosmology (e.g Fry, 1994; Matarrese et al., 1997; Scoccimarro et al., 1998). Until recently, surveys were not large enough to make observations suitable for studying the bispectrum. Fortunately, now we have many tools to investigate the bispectrum: new generations of telescopes have been commissioned and the necessary computing power is easily available. For instance, the *Euclid* mission will observe a large volume of the sky, which will enable precise measurements of the bispectrum to be performed. Therefore, we decided to investigate the properties of the bispectrum, with the goal of estimating the effect of implementing the bispectrum into the cosmological forecast for future missions, and to demonstrate the benefits of the using tools such as the redshift-space bispectrum in many cosmological aspects.

First of all, we studied the properties of the galaxy bispectrum in redshift space. We explored different parametrizations for the spatial orientation of the triangles of wavevectors with respect to the line of sight. This is the first time such a study has been attempted, and so we have documented several different approaches for the parametrizations, to aid in future research using this technique. We demonstrate that with only one quarter of the full parameter space of the spatial orientation, the RSD bispectrum can be fully determined. This result enables a significant decrease in computational costs without loss of precision.

Secondly, we investigated the uses of the bispectrum as a statistical tool in measuring the cosmological parameters. We present the Fisher matrix forecast for the set of cosmological parameters in ΛCDM, wCDM and w_0w_aCDM models for the *Euclid*-like surveys. The forecast was made for the power spectrum, the bispectrum and their combination, with and without cross-covariance terms. From our analysis of the forecast's results, we demonstrate that the combination of the power spectrum and the bispectrum gives much better constraints on cosmological parameters compared to a single probe. For example, for the dark-energy equation of state, the joint forecast improves the FoM by a factor of 2.6. We demonstrate that investing the computational time in adding the bispectrum yields much more accurate constraints on cosmological parameters than previous studies where this was omitted.

Finally, we studied different techniques for the bispectrum binning. Raw observations of galaxy

clustering must be binned using an approach that is suitable for storage and data processing, and the bispectrum binning should be adaptable for this comparison. We find that the average technique produces the most accurate results, and we demonstrate that our results will be an extremely useful reference for future comparisons of theoretical predictions with observational data.

The methods and results produced during this work are also very useful for the science working groups of the Euclid consortium. First of all, the study of the bispectrum as a statistical tool to obtain cosmological information is the foundation for several projects within the 'Higher-order statistics' work-package of the galaxy clustering science working group. One of the goals of the work-package is to make a forecast, with the *Euclid* survey specifications, using the higher-order statistics and to see if this can help to extract new cosmological information. This goal was reached in Chapter 2 of this thesis. Also, the sets of wavevectors and the bispectrum obtained from different binning methods (they are presented in Chapter 3) are now being used in another project. The goal of this project is to compare theoretical predictions for the matter bispectrum against measurements from a large set of N-body simulations. The paper is now in preparation. The results have been presented at the Euclid consortium meetings. Finally, the code for evaluating the Fisher matrix for the power spectrum was modified to fit the specific requirements of the *Euclid* inter-science working group task force for forecasting (IST:F). The modified Fisher matrix code was validated as an official forecast *Euclid* code and the results have been used in Euclid Collaboration et al. (2019). The paper is currently under revision of the *Euclid* Consortium Editorial Board and after this will be submitted to the journal Astronomy & Astrophysics.

4.2 Ongoing work and outlook

The first topic which we will be exploring soon is testing the effects of adding the non-Gaussian contributions to the covariance matrices for the power spectrum, the bispectrum and especially for their combination. In this thesis, the bispectrum covariance matrix always includes a non-Gaussian term. For this reason, it is necessary to make the same extension to all covariance matrices. For example, the addition of the trispectrum term is a very complicated process but it should help to make the forecast more realistic. The most interesting and important aim of this work is to realize if we actually need all these extensions or not. Most likely, the effect of adding the non-Gaussian terms can play an important role for one task and can be neglected for others to speed up the calculations. In general, this project will help us to understand more about the properties of the covariance matrices which may be important for other topics in astrophysics as well.

The second goal will be to make a more accurate forecast using the Markov chain Monte Carlo (MCMC) method for the same cosmological models as in Chapter 2 and extended ones. The Fisher-matrix method works well only if the likelihood function is approximately Gaussian. Strictly speaking, there is no guarantee that this is correct for all cosmological data sets. Also, the Fisher matrix becomes unstable if a large amount of degenerate parameters are included in the model. This sets constraints on number of parameters that can be used in one Fisher matrix. Therefore, MCMC will provide more reliable forecasts for cosmological models with a large number of parameters.

Naturally, the next step will be to use the MCMC method based on mock data. In particular, we will use the *Euclid* flagship mock galaxy catalogue (currently in final stage of preparation) to contribute to the *Euclid* Consortium work.

The final goal will be to work with the real observational data. For this study it will be necessary to

account for many additional effects, like the selection one, window function, survey configuration, etc.

Despite the cosmological constant problem has been known for a very long time, it is still one of the hottest topics in cosmology and upcoming surveys can help us to understand more about it. That is why the main goal of the future research is to contribute to the understanding of the origin of cosmic acceleration, measuring neutrino masses and constrain the level of the primordial non-Gaussianity. This will help us to push the boundaries of our knowledge about the Universe.

Bibliography

Albrecht A., et al., 2006, arXiv e-prints, pp astro–ph/0609591

Amendola L., et al., 2018, Living Reviews in Relativity, 21, 2

Angulo R. E., Baugh C. M., Frenk C. S., Lacey C. G., 2014, MNRAS, 442, 3256

Angulo R., Fasiello M., Senatore L., Vlah Z., 2015, JCAP, 9, 029

Assassi V., Baumann D., Green D., Zaldarriaga M., 2014, JCAP, 8, 056

Baldauf T., Seljak U., Desjacques V., McDonald P., 2012, Phys. Rev. D, 86, 083540

Baldauf T., Seljak U., Smith R. E., Hamaus N., Desjacques V., 2013, Phys. Rev. D, 88, 083507

Baldauf T., Mercolli L., Mirbabayi M., Pajer E., 2015, JCAP, 5, 007

Baldauf T., Mirbabayi M., Simonović M., Zaldarriaga M., 2016, arXiv e-prints, p. arXiv:1602.00674

Ballinger W. E., Peacock J. A., Heavens A. F., 1996, MNRAS, 282, 877

Bardeen J. M., Bond J. R., Kaiser N., Szalay A. S., 1986, ApJ, 304, 15

Barkana R., Loeb A., 2001, Phys. Rep., 349, 125

Baugh C. M., Efstathiou G., 1993, MNRAS, 265, 145

Baumann D., Nicolis A., Senatore L., Zaldarriaga M., 2012, JCAP, 7, 051

Bel J., Hoffmann K., Gaztañaga E., 2015, MNRAS, 453, 259

Bernardeau F., Colombi S., Gaztañaga E., Scoccimarro R., 2002, Phys. Rep., 367, 1

Bertolini D., Schutz K., Solon M. P., Zurek K. M., 2016, JCAP, 6, 052

Beutler F., et al., 2014, MNRAS, 443, 1065

Bhattacharya S., Heitmann K., White M., Lukić Z., Wagner C., Habib S., 2011, ApJ, 732, 122

Bianchi D., Gil-Marín H., Ruggeri R., Percival W. J., 2015, MNRAS, 453, L11

Borzyszkowski M., Bertacca D., Porciani C., 2017, MNRAS, 471, 3899

Bunn E. F., 1995, Ph.D. Thesis,

Byun J., Eggemeier A., Regan D., Seery D., Smith R. E., 2017, MNRAS, 471, 1581

Carrasco J. J. M., Hertzberg M. P., Senatore L., 2012, Journal of High Energy Physics, 9, 82

Carron J., 2012, Physical Review Letters, 108, 071301

Carron J., Neyrinck M. C., 2012, ApJ, 750, 28

Carron J., Szapudi I., 2014, MNRAS, 439, L11

Catelan P., Lucchin F., Matarrese S., Porciani C., 1998, MNRAS, 297, 692

Catelan P., Porciani C., Kamionkowski M., 2000, MNRAS, 318, L39

Chan K. C., Blot L., 2017, Phys. Rev. D, 96, 023528

Chan K. C., Scoccimarro R., Sheth R. K., 2012, Phys. Rev. D, 85, 083509

Chevallier M., Polarski D., 2001, International Journal of Modern Physics D, 10, 213

Clowe D., Bradač M., Gonzalez A. H., Markevitch M., Randall S. W., Jones C., Zaritsky D., 2006, ApJL, 648, L109

Coe D., 2009, arXiv e-prints, p. arXiv:0906.4123

Cole S., et al., 2005, MNRAS, 362, 505

Colless M., et al., 2001, MNRAS, 328, 1039

Crocce M., Scoccimarro R., Bernardeau F., 2012, MNRAS, 427, 2537

Croton D. J., et al., 2004, MNRAS, 352, 1232

DESI Collaboration et al., 2016a, arXiv e-prints, p. arXiv:1611.00036

DESI Collaboration et al., 2016b, arXiv e-prints, p. arXiv:1611.00037

Davis M., Efstathiou G., Frenk C. S., White S. D. M., 1985, ApJ, 292, 371

Dekel A., Lahav O., 1999, ApJ, 520, 24

Desjacques V., Jeong D., Schmidt F., 2018, Phys. Rep., 733, 1

Dodelson S., 2003, Modern cosmology

Eisenstein D. J., et al., 2005, ApJ, 633, 560

Euclid Collaboration et al., 2019, Submitted to Euclid Consortium Editorial Board, prepaired to submittion to A&A

Feldman H. A., Kaiser N., Peacock J. A., 1994, ApJ, 426, 23

Fisher R. A., 1935, Journal of the Royal Statistical Society, 98, 39

Fisher K. B., Scharf C. A., Lahav O., 1994, MNRAS, 266, 219

Fonseca de la Bella L., Regan D., Seery D., Hotchkiss S., 2017, JCAP, 11, 039

Frieman J. A., Gaztañaga E., 1999, ApJL, 521, L83

Fry J. N., 1994, Physical Review Letters, 73, 215

Fry J. N., Gaztanaga E., 1993, ApJ, 413, 447

Fry J. N., Melott A. L., Shandarin S. F., 1993, ApJ, 412, 504

Gagrani P., Samushia L., 2017, MNRAS, 467, 928

Gaztañaga E., Norberg P., Baugh C. M., Croton D. J., 2005, MNRAS, 364, 620

Gaztañaga E., Cabré A., Castander F., Crocce M., Fosalba P., 2009, MNRAS, 399, 801

Geach J. E., Sobral D., Hickox R. C., Wake D. A., Smail I., Best P. N., Baugh C. M., Stott J. P., 2012, MNRAS, 426, 679

Geller M. J., Huchra J. P., 1989, Science, 246, 897

Giannantonio T., Porciani C., Carron J., Amara A., Pillepich A., 2012, MNRAS, 422, 2854

Gil-Marín H., Wagner C., Noreña J., Verde L., Percival W., 2014, JCAP, 12, 029

Gil-Marín H., Noreña J., Verde L., Percival W. J., Wagner C., Manera M., Schneider D. P., 2015, MNRAS, 451, 539

Gil-Marín H., Percival W. J., Verde L., Brownstein J. R., Chuang C.-H., Kitaura F.-S., Rodríguez-Torres S. A., Olmstead M. D., 2017, MNRAS, 465, 1757

Gonzalez-Perez V., et al., 2018, MNRAS, 474, 4024

Gorbunov D. S., Rubakov V. A., 2011b, Introduction to the Theory of the Early Universe: Cosmological Perturbations and Inflationary Theory. World Scientific Publishing Co, doi:10.1142/7873

Gorbunov D. S., Rubakov V. A., 2011a, Introduction to the Theory of the Early Universe: Hot Big Bang Theory. World Scientific Publishing Co, doi:10.1142/7874

Gualdi D., Manera M., Joachimi B., Lahav O., 2018, MNRAS, 476, 4045

Gualdi D., Gil-Marín H., Schuhmann R. L., Manera M., Joachimi B., Lahav O., 2019, MNRAS, 484, 3713

Hamaus N., Seljak U., Desjacques V., Smith R. E., Baldauf T., 2010, Phys. Rev. D, 82, 043515

Hamilton A. J. S., 1998, Linear Redshift Distortions: A Review. Springer Netherlands, Dordrecht, pp 185–275, doi:10.1007/978-94-011-4960-0_17, https://doi.org/10.1007/978-94-011-4960-0_17

Harrison E. R., 1970, Phys. Rev. D, 1, 2726

Hashimoto I., Rasera Y., Taruya A., 2017, Phys. Rev. D, 96, 043526

Heavens A., 2009, arXiv e-prints, p. arXiv:0906.0664

Heavens A. F., Taylor A. N., 1995, MNRAS, 275, 483

Hoffmann K., Bel J., Gaztañaga E., 2017, MNRAS, 465, 2225

Howlett C., Lewis A., Hall A., Challinor A., 2012, JCAP, 1204, 027

Hubble E., 1929, Proceedings of the National Academy of Science, 15, 168

Huchra J., Davis M., Latham D., Tonry J., 1983, ApJS, 52, 89

Jackson J. C., 1972, MNRAS, 156, 1P

Jeong D., Komatsu E., 2009, ApJ, 703, 1230

Jing Y. P., Börner G., 1998, ApJ, 503, 37

Jing Y. P., Börner G., 2004, ApJ, 607, 140

Kaiser N., 1987, MNRAS, 227, 1

Karagiannis D., Lazanu A., Liguori M., Raccanelli A., Bartolo N., Verde L., 2018, MNRAS, 478, 1341

Kayo I., Takada M., Jain B., 2013, MNRAS, 429, 344

Kazin E. A., Sánchez A. G., Blanton M. R., 2012, MNRAS, 419, 3223

Kirshner R. P., Oemler Jr. A., Schechter P. L., Shectman S. A., 1981, ApJL, 248, L57

Kulkarni G. V., Nichol R. C., Sheth R. K., Seo H.-J., Eisenstein D. J., Gray A., 2007, MNRAS, 378, 1196

Kuruvilla J., Porciani C., 2018, MNRAS, 479, 2256

Laureijs R., 2009, arXiv e-prints, p. arXiv:0912.0914

Lazanu A., Giannantonio T., Schmittfull M., Shellard E. P. S., 2016, Phys. Rev. D, 93, 083517

Lazeyras T., Wagner C., Baldauf T., Schmidt F., 2016, JCAP, 2, 018

Lesgourgues J., Mangano G., Miele G., Pastor S., 2013, Neutrino Cosmology

Lewis A., Challinor A., Lasenby A., 2000, Astrophys. J., 538, 473

Lin H., Kirshner R. P., Shectman S. A., Landy S. D., Oemler A., Tucker D. L., Schechter P. L., 1996, ApJ, 471, 617

Linder E. V., 2003, Physical Review Letters, 90, 091301

Lucy L. B., 1974, AJ, 79, 745

Maartens R., Abdalla F. B., Jarvis M., Santos M. G., 2015, Advancing Astrophysics with the Square Kilometre Array (AASKA14), p. 16

March M., 2013, Advanced Statistical Methods for Astrophysical Probes of Cosmology. Springer Theses, Springer Berlin Heidelberg, https://books.google.de/books?id=bTFEAAAAQBAJ

Marín F., 2011, ApJ, 737, 97

Markevitch M., Randall S., Clowe D., Gonzalez A., Bradac M., 2006, in 36th COSPAR Scientific Assembly.

Matarrese S., Verde L., Heavens A. F., 1997, MNRAS, 290, 651

Matsubara T., 1999, ApJ, 525, 543

Matsubara T., 2008, Phys. Rev. D, 77, 063530

McDonald P., Roy A., 2009, JCAP, 8, 020

Mehrem R., 2009, arXiv e-prints, p. arXiv:0909.0494

Meiksin A., White M., 1999, MNRAS, 308, 1179

Mo H. J., White S. D. M., 1996, MNRAS, 282, 347

Mohammed I., Seljak U., Vlah Z., 2017, MNRAS, 466, 780

Moradinezhad Dizgah A., Lee H., Muñoz J. B., Dvorkin C., 2018, JCAP, 5, 013

Mortonson M. J., Huterer D., Hu W., 2010, Phys. Rev. D, 82, 063004

Neyrinck M. C., Szapudi I., 2007, MNRAS, 375, L51

Nichol R. C., et al., 2006, MNRAS, 368, 1507

Orsi A., Baugh C. M., Lacey C. G., Cimatti A., Wang Y., Zamorani G., 2010, MNRAS, 405, 1006

Pápai P., Szapudi I., 2008, MNRAS, 389, 292

Peacock J. A., 1992, in Martinez V. J., Portilla M., Saez D., eds, Lecture Notes in Physics, Berlin Springer Verlag Vol. 408, New Insights into the Universe. p. 1, doi:10.1007/3-540-55842-X_28

Peacock J. A., 1999, Cosmological Physics

Peacock J. A., Dodds S. J., 1994, MNRAS, 267, 1020

Peebles P. J. E., 1993, Principles of Physical Cosmology

Peebles P. J. E., Yu J. T., 1970, ApJ, 162, 815

Planck Collaboration et al., 2014, A&A, 571, A16

Planck Collaboration et al., 2016, A&A, 594, A13

Planck Collaboration et al., 2018, arXiv e-prints, p. arXiv:1807.06209

Pozzetti L., et al., 2016, A&A, 590, A3

Press W. H., Schechter P., 1974, ApJ, 187, 425

Rimes C. D., Hamilton A. J. S., 2005, MNRAS, 360, L82

Robertson A., Massey R., Eke V., 2017, MNRAS, 465, 569

Rubin V. C., Ford Jr. W. K., 1970, ApJ, 159, 379

Sahni V., Starobinsky A., 2006, International Journal of Modern Physics D, 15, 2105

Saito S., Baldauf T., Vlah Z., Seljak U., Okumura T., McDonald P., 2014, Phys. Rev. D, 90, 123522

Sargent W. L. W., Turner E. L., 1977, ApJL, 212, L3

Scherrer R. J., 2015, Phys. Rev. D, 92, 043001

Schmittfull M., Baldauf T., Seljak U., 2015, Phys. Rev. D, 91, 043530

Schneider P., 2006, Extragalactic Astronomy and Cosmology

Schramm D. N., Steigman G., 1981, ApJ, 243, 1

Scoccimarro R., 2000, ApJ, 544, 597

Scoccimarro R., 2004, Phys. Rev. D, 70, 083007

Scoccimarro R., 2015, Phys. Rev. D, 92, 083532

Scoccimarro R., Colombi S., Fry J. N., Frieman J. A., Hivon E., Melott A., 1998, ApJ, 496, 586

Scoccimarro R., Couchman H. M. P., Frieman J. A., 1999a, ApJ, 517, 531

Scoccimarro R., Zaldarriaga M., Hui L., 1999b, ApJ, 527, 1

Scoccimarro R., Feldman H. A., Fry J. N., Frieman J. A., 2001, ApJ, 546, 652

Scoccimarro R., Sefusatti E., Zaldarriaga M., 2004, Phys. Rev. D, 69, 103513

Sefusatti E., Komatsu E., 2007, Phys. Rev. D, 76, 083004

Sefusatti E., Crocce M., Pueblas S., Scoccimarro R., 2006, Phys. Rev. D, 74, 023522

Senatore L., 2015, JCAP, 11, 007

Sheth R. K., Mo H. J., Tormen G., 2001, MNRAS, 323, 1

Slepian Z., et al., 2017, MNRAS, 468, 1070

Song Y.-S., Taruya A., Oka A., 2015, JCAP, 8, 007

Subba Rao M. U., Aragón-Calvo M. A., Chen H. W., Quashnock J. M., Szalay A. S., York D. G., 2008, New Journal of Physics, 10, 125015

Takahashi R., et al., 2009, ApJ, 700, 479

Taruya A., Saito S., Nishimichi T., 2011, Phys. Rev. D, 83, 103527

Taylor A. N., Hamilton A. J. S., 1996, MNRAS, 282, 767

Tegmark M., Taylor A. N., Heavens A. F., 1997, ApJ, 480, 22

Tellarini M., Ross A. J., Tasinato G., Wands D., 2016, JCAP, 6, 014

Verde L., et al., 2002, MNRAS, 335, 432

Vogeley M. S., Szalay A. S., 1996, ApJ, 465, 34

Wang Y., 2008, Phys. Rev. D, 77, 123525

White S. D. M., Davis M., Efstathiou G., Frenk C. S., 1987, Nature, 330, 451

Yamauchi D., Yokoyama S., Takahashi K., 2017a, Phys. Rev. D, 95, 063530

Yamauchi D., Yokoyama S., Tashiro H., 2017b, Phys. Rev. D, 96, 123516

Yang J., Schramm D. N., Steigman G., Rood R. T., 1979, ApJ, 227, 697

Yankelevich V., Porciani C., 2019, MNRAS, 483, 2078

Zeldovich Y. B., 1972, MNRAS, 160, 1P

Appendix

APPENDIX A

Appendix for Chapter 2

A.1 Coordinate systems

We introduce here two different coordinate systems in order to parameterize the relative orientation between a triangle of wavevectors and the line of sight.

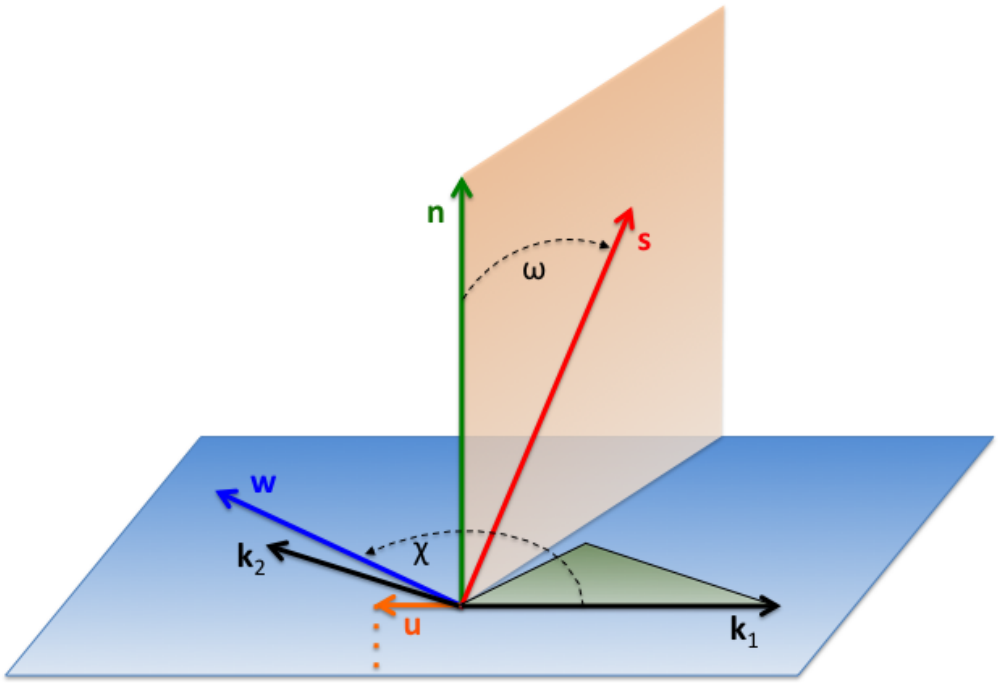

Figure A.1: Schematic showing the definition of the angles (ω, χ).

A.1.1 Using the triangle's normal as the polar axis

Let us consider a triangle of sides $\boldsymbol{k}_1$, $\boldsymbol{k}_2$ and $\boldsymbol{k}_3$ such that $\boldsymbol{k}_1 + \boldsymbol{k}_2 + \boldsymbol{k}_3 = 0$. The triangle lies on a plane whose normal vector is parallel to $\boldsymbol{n} = \boldsymbol{k}_1 \times \boldsymbol{k}_2$. The orientation of the unit vector $\hat{\boldsymbol{n}} = \boldsymbol{n}/||\boldsymbol{n}||$ with respect to the line-of-sight direction $\hat{\boldsymbol{s}}$ can be described in terms of a single rotation around the axis $\boldsymbol{w} = \hat{\boldsymbol{n}} \times \hat{\boldsymbol{s}}$ (see Fig. A.1). We want to build a right-handed orthonormal basis starting from $\hat{\boldsymbol{s}}$ and $\hat{\boldsymbol{w}}$. For the third element of the basis we pick a unit vector $\hat{\boldsymbol{u}}$ parallel to $\hat{\boldsymbol{s}} \times \hat{\boldsymbol{w}} = \hat{\boldsymbol{n}} - (\hat{\boldsymbol{n}} \cdot \hat{\boldsymbol{s}})\, \hat{\boldsymbol{s}}$, i.e. $\hat{\boldsymbol{u}} = (\hat{\boldsymbol{n}} - (\hat{\boldsymbol{n}} \cdot \hat{\boldsymbol{s}})\, \hat{\boldsymbol{s}})/\sqrt{1 - (\hat{\boldsymbol{n}} \cdot \hat{\boldsymbol{s}})^2}$. In the base $\hat{\boldsymbol{w}}$, $\hat{\boldsymbol{u}}$, $\hat{\boldsymbol{s}}$, the rotation from $\hat{\boldsymbol{n}}$ to $\hat{\boldsymbol{s}}$ is described by the matrix,

$$\mathbf{R} = \begin{pmatrix} 1 & 0 & 0 \\ 0 & \hat{\boldsymbol{n}} \cdot \hat{\boldsymbol{s}} & -||\hat{\boldsymbol{n}} \times \hat{\boldsymbol{s}}|| \\ 0 & ||\hat{\boldsymbol{n}} \times \hat{\boldsymbol{s}}|| & \hat{\boldsymbol{n}} \cdot \hat{\boldsymbol{s}} \end{pmatrix} . \tag{A.1}$$

In fact, $\hat{\boldsymbol{n}}$ is a column vector with coordinates

$$(\hat{\boldsymbol{n}} \cdot \hat{\boldsymbol{w}}, \hat{\boldsymbol{n}} \cdot \hat{\boldsymbol{u}}, \hat{\boldsymbol{n}} \cdot \hat{\boldsymbol{s}}) = (0, \sqrt{1 - (\hat{\boldsymbol{n}} \cdot \hat{\boldsymbol{s}})^2}, \hat{\boldsymbol{n}} \cdot \hat{\boldsymbol{s}}) \tag{A.2}$$

and applying the rotation to it one gets $(0, 0, 1)$. This is a rotation by an angle $0 \leq \omega < \pi$ such that $\cos\omega = \hat{\boldsymbol{n}} \cdot \hat{\boldsymbol{s}}$ and $\sin\omega = ||\hat{\boldsymbol{n}} \times \hat{\boldsymbol{s}}|| = ||\boldsymbol{w}||$ (note than $\sin\omega \geq 0$). This completely describes the relative orientation of the plane of the triangle with respect to the line of sight.

Now, we only need to describe the orientation of the triangle on its plane. Note that, being perpendicular to $\hat{\boldsymbol{n}}$, the basis element $\hat{\boldsymbol{w}}$ lies on the plane of the triangle. It is thus convenient to measure the orientation of the triangle in its plane by looking at the orientation of, say, $\boldsymbol{k}_1$ with respect to $\hat{\boldsymbol{w}}$. In order to quantify this, we introduce the angle χ ($0 \leq \chi < 2\pi$) such that $\hat{\boldsymbol{k}}_1 \cdot \hat{\boldsymbol{w}} = \cos\chi$ and $(\hat{\boldsymbol{k}}_1 \times \hat{\boldsymbol{w}}) \cdot \hat{\boldsymbol{n}} = \sin\chi$. It is worth stressing that $\hat{\boldsymbol{k}}_1 \times \hat{\boldsymbol{w}} = \hat{\boldsymbol{k}}_1 \times (\hat{\boldsymbol{n}} \times \hat{\boldsymbol{s}})/||\boldsymbol{w}|| = (\hat{\boldsymbol{k}}_1 \cdot \hat{\boldsymbol{s}})\, \hat{\boldsymbol{n}}/||\boldsymbol{w}||$ and $\sin\chi = (\hat{\boldsymbol{k}}_1 \cdot \hat{\boldsymbol{s}})/||\boldsymbol{w}|| = \mu_1/\sin\omega$. The angle χ denotes the rotation angle around $\hat{\boldsymbol{n}}$ from $\hat{\boldsymbol{k}}_1$ to $\hat{\boldsymbol{w}}$.

Let us now reverse the problem and determine the line-of-sight components of $\boldsymbol{k}_1, \boldsymbol{k}_2, \boldsymbol{k}_3$ for given ω and χ. The shape and the handedness of the triangle matter. A common choice is to parameterize the relative orientation of $\boldsymbol{k}_1$ and $\boldsymbol{k}_2$ in terms of the angle θ_{12} such that $\hat{\boldsymbol{k}}_2 \cdot \hat{\boldsymbol{k}}_1 = \cos\theta_{12}$ and $||\boldsymbol{n}|| = ||\boldsymbol{k}_1 \times \boldsymbol{k}_2|| = |\sin\theta_{12}|$. In principle, $0 \leq \theta_{12} < 2\pi$ and, for a fixed shape, triangles with θ_{12} and $2\pi - \theta_{12}$ have opposite handedness (see Fig. A.2). However, $\hat{\boldsymbol{n}}$, $\hat{\boldsymbol{w}}$ and $\hat{\boldsymbol{u}}$ flip sign when the handedness is switched. It is thus much more convenient to express the shape of the triangle in terms of a rotation angle around $\hat{\boldsymbol{n}}$ and always use an angle ξ_{12} such that $0 \leq \xi_{12} < \pi$ and $\sin\xi_{12} \geq 0$. In words, $\xi_{12} = \arccos\left(\hat{\boldsymbol{k}}_1 \cdot \hat{\boldsymbol{k}}_2\right)$ is the (shortest) rotation angle around $\hat{\boldsymbol{n}}$ from $\hat{\boldsymbol{k}}_1$ to $\hat{\boldsymbol{k}}_2$. Triangles with the same shape but opposite handedness have identical ξ_{12}.

We recall that, using the vector basis we have introduced above, $\hat{\boldsymbol{n}} = (0, \sin\omega, \cos\omega)$ and $\hat{\boldsymbol{s}} = (0, 0, 1)$, so that $\boldsymbol{w} = (\sin\omega, 0, 0)$ and $\boldsymbol{u} = (0, \sin\omega, 0)$. From the definitions $\hat{\boldsymbol{k}}_1 \cdot \hat{\boldsymbol{w}} = \cos\chi$ and $(\hat{\boldsymbol{k}}_1 \times \hat{\boldsymbol{w}}) \cdot \hat{\boldsymbol{n}} = \sin\chi$, it follows that

$$\boldsymbol{k}_1 = k_1\, (\cos\chi, -\cos\omega \sin\chi, \sin\omega \sin\chi) . \tag{A.3}$$

Since the vector $\hat{\boldsymbol{k}}_2$ corresponds to a rotation of $\hat{\boldsymbol{k}}_1$ by an angle ξ_{12} around $\hat{\boldsymbol{n}}$ while $\hat{\boldsymbol{w}}$ is rotated from $\hat{\boldsymbol{k}}_1$ by an angle χ around $\hat{\boldsymbol{n}}$, it follows that

$$\boldsymbol{k}_2 = k_2\, (\cos(\chi - \xi_{12}), -\cos\omega \sin(\chi - \xi_{12}), \sin\omega \sin(\chi - \xi_{12})) . \tag{A.4}$$

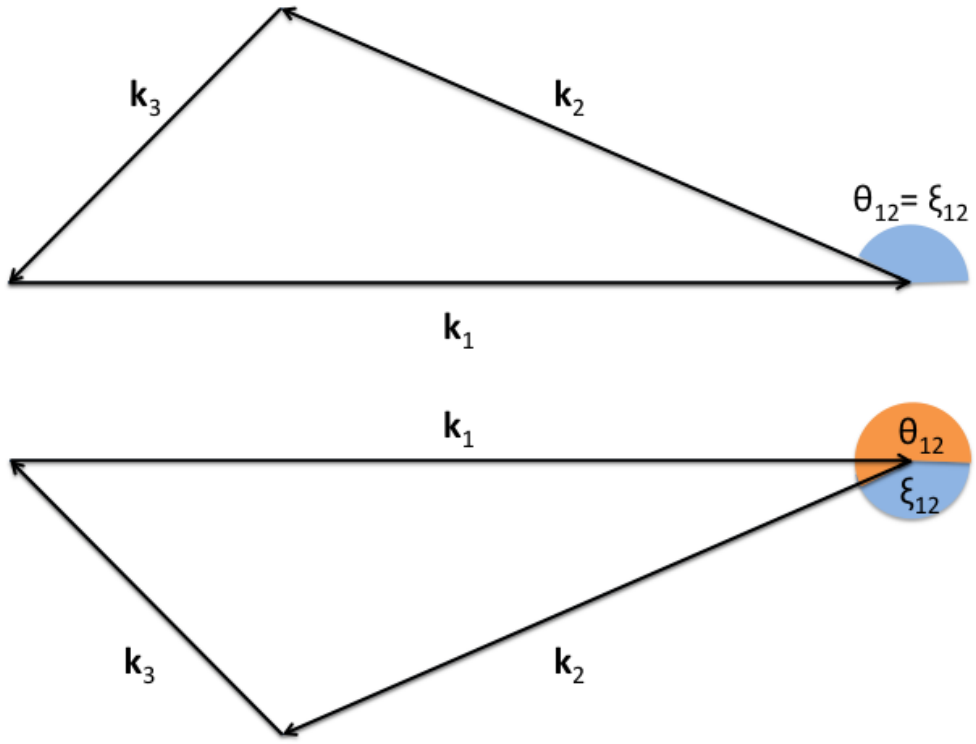

Figure A.2: Definition of the angles θ_{12} and ξ_{12} for two triangles with the same shape but opposite handedness.

This univocally fixes the RSD:

$$\mu_1 = \sin\omega \sin\chi \,, \tag{A.5}$$
$$\mu_2 = \sin\omega \sin(\chi - \xi_{12}) \,. \tag{A.6}$$

A.1.2 Using k_1 as the polar axis

Scoccimarro et al. (1999) use a different parameterization in terms of the polar angle $0 \leq \theta < \pi$ and the azimuthal angle $0 \leq \phi < 2\pi$ that define the orientation of $\hat{\boldsymbol{s}}$ with respect to $\hat{\boldsymbol{k}}_1$ (see Fig. A.3). In order to link this approach to our previous discussion, let us build a right-handed orthonormal basis by complementing $\hat{\boldsymbol{n}}$ and $\hat{\boldsymbol{k}}_1$ with another unit vector $\hat{\boldsymbol{e}}$ lying in the plane of the triangle – i.e, $\hat{\boldsymbol{e}}$ is the unit vector of $\boldsymbol{e} = \boldsymbol{n} \times \boldsymbol{k}_1 = k_1^2\, \boldsymbol{k}_2 - (\boldsymbol{k}_1 \cdot \boldsymbol{k}_2)\, \boldsymbol{k}_1$ or $\hat{\boldsymbol{e}} = [\hat{\boldsymbol{k}}_2 - (\hat{\boldsymbol{k}}_1 \cdot \hat{\boldsymbol{k}}_2)\, \hat{\boldsymbol{k}}_1]/\sqrt{1 - (\hat{\boldsymbol{k}}_1 \cdot \hat{\boldsymbol{k}}_2)^2}$. In the basis $(\hat{\boldsymbol{k}}_1, \hat{\boldsymbol{e}}, \hat{\boldsymbol{n}})$, $\hat{\boldsymbol{k}}_2$ is a column vector of coordinates $(\cos\xi_{12}, \sin\xi_{12}, 0)$ - note once again that both $\hat{\boldsymbol{n}}$ and $\hat{\boldsymbol{e}}$ flip sign if the handedness of the triangle is changed and this is why we can use ξ_{12} instead of θ_{12}. For the azimuth ϕ, we use the angle between $\hat{\boldsymbol{n}}$ and the projection of $\hat{\boldsymbol{s}}$ on the plane defined by $\hat{\boldsymbol{n}}$ and $\hat{\boldsymbol{e}}$.

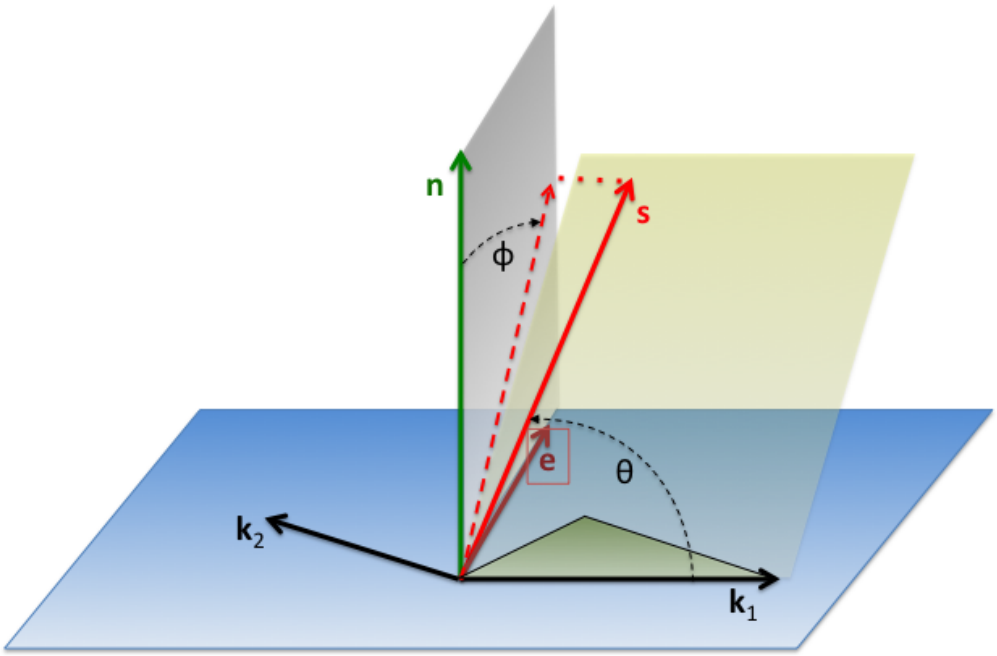

Figure A.3: Schematic showing the definition of the angles (θ, ϕ).

This means that $\cos\phi = 0$ (i.e. $\phi = \pi/2$ or $3\pi/2$) whenever $\hat{\boldsymbol{s}}$ lies on the plane of triangle. Given all this, in the basis $(\hat{\boldsymbol{k}}_1, \hat{\boldsymbol{e}}, \hat{\boldsymbol{n}})$, $\hat{\boldsymbol{s}}$ is the column vector of coordinates $(\cos\theta, \sin\theta\,\sin\phi, \sin\theta\,\cos\phi)$ so that

$$\mu_1 = \cos\theta\,, \tag{A.7}$$

$$\mu_2 = \cos\theta\cos\xi_{12} + \sin\theta\sin\phi\sin\xi_{12}\,. \tag{A.8}$$

For generic vectors $\boldsymbol{k}_1, \boldsymbol{k}_2$ and $\hat{\boldsymbol{s}}$ defined in an arbitrary basis (e.g. a Fourier grid used to measure the bispectrum in a numerical simulation or for a galaxy catalogue), the angles θ and ϕ can be determined as follows. The polar angle is simply given by $\theta = \arccos\left(\hat{\boldsymbol{k}}_1 \cdot \hat{\boldsymbol{s}}\right)$. For the azimuth, instead, it is convenient to introduce the vector $\boldsymbol{s}_\perp = \hat{\boldsymbol{s}} - (\hat{\boldsymbol{s}} \cdot \hat{\boldsymbol{k}}_1)\,\hat{\boldsymbol{k}}_1$ (which gives the component of $\hat{\boldsymbol{s}}$ perpendicular to $\boldsymbol{k}_1$) and calculate the real numbers $\cos\phi = \hat{\boldsymbol{s}}_\perp \cdot \hat{\boldsymbol{n}} = (\hat{\boldsymbol{s}} \cdot \hat{\boldsymbol{n}})/||\boldsymbol{s}_\perp|| = \sigma_n$ and $\sin\phi = \hat{\boldsymbol{s}}_\perp \cdot \hat{\boldsymbol{e}} = (\hat{\boldsymbol{s}} \cdot \hat{\boldsymbol{e}})/||\boldsymbol{s}_\perp|| = \sigma_e$. If $\sin\phi > 0$, then $\phi = \arccos(\sigma_n)$ while, if $\sin\phi < 0$, $\phi = 2\pi - \arccos(\sigma_n)$.

A.1.3 Matching the different coordinate systems

Starting from the expressions for $\boldsymbol{k}_1$, $\boldsymbol{k}_2$ and $\boldsymbol{s}$ in the (θ, ϕ) coordinates and applying the definitions of the angles ω and χ, one obtains:

$$\cos\omega = \sin\theta\cos\phi\,, \tag{A.9}$$

$$\sin\omega = \sqrt{1-\sin^2\theta\cos^2\phi}\,, \tag{A.10}$$

$$\cos\chi = \frac{-\sin\theta\sin\phi}{\sqrt{1-\sin^2\theta\cos^2\phi}}\,, \tag{A.11}$$

$$\sin\chi = \frac{\cos\theta}{\sqrt{1-\sin^2\theta\cos^2\phi}}\,. \tag{A.12}$$

Vice versa, starting from the expressions in terms of (ω, χ), one derives:

$$\cos\theta = \sin\omega\sin\chi\,, \tag{A.13}$$

$$\sin\theta = \sqrt{1-\sin^2\omega\sin^2\chi}\,, \tag{A.14}$$

$$\cos\phi = \frac{\cos\omega}{\sqrt{1-\sin^2\omega\sin^2\chi}}\,, \tag{A.15}$$

$$\sin\phi = \frac{-\sin\omega\cos\chi}{\sqrt{1-\sin^2\omega\sin^2\chi}}\,. \tag{A.16}$$

A.1.4 Symmetries

RSD are quadratic in the μ_i and do not change if μ_1, μ_2 and μ_3 change sign simultaneously. In terms of the (θ, ϕ) variables, this means that the galaxy bispectrum in redshift space is symmetric with respect to the transformation

$$\begin{cases} \theta \to \pi - \theta\,, \\ \phi \to 2\pi - \phi\,. \end{cases} \tag{A.17}$$

In fact, by considering equations (A.7) and (A.8), one can easily prove that this transformation changes sign to μ_1, μ_2 and μ_3. This means that the (θ, ϕ) variables are somewhat redundant and not all the parameter space they cover is necessary to describe the RSD. It is thus appealing to seek for new angular coordinates that make the necessary region more compact and do not present duplications. In fact, this helps reduce the number of bins needed to represent all possible configurations. For instance, we can halve the size of parameter space by introducing a new set of coordinates $(\tilde{\theta}, \phi')$ such that $\tilde{\theta} = \min(\theta, \pi - \theta)$ and

$$\phi' = \begin{cases} \phi\,, & \text{if } \theta < \pi/2\,, \\ 2\pi - \phi\,, & \text{otherwise.} \end{cases} \tag{A.18}$$

In this case, $0 \leq \tilde{\theta} < \pi/2$ (or $0 < \tilde{\mu} = \cos\tilde{\theta} \leq 1$) and $0 \leq \phi' < 2\pi$. However, RSD possess still another symmetry deriving from the fact that they only depend on $\sin\phi$ (and, equivalently, on $\sin\phi'$). Since, $\sin(\pi - x) = \sin x$, we can further halve the area of parameter space by introducing the variable

$\pi/2 \leq \tilde{\phi} < 3\pi/2$ defined as follows

$$\tilde{\phi} = \begin{cases} \pi - \phi' \,, & \text{if } 0 \leq \phi' < \pi/2 \,, \\ \phi' \,, & \text{if } \pi/2 \leq \phi' < 3\pi/2 \,, \\ 3\pi - \phi' \,, & \text{if } 3\pi/2 \leq \phi' < 2\pi \,. \end{cases} \tag{A.19}$$

The angular variables $\tilde{\theta}$ and $\tilde{\phi}$ are optimal in the sense that they suffice to describe all possible configurations while minimizing the size of parameter space.

Similarly, we can derive optimal variables also starting from the coordinates (ω, χ). Equations (A.5) and (A.6) show that μ_1 and μ_2 change sign if $\chi \to \pi + \chi$ while ω is left unchanged. It follows that considering the variable $0 \leq \tilde{\chi} < \pi$ defined as

$$\tilde{\chi} = \begin{cases} \chi \,, & \text{if } \chi < \pi \,, \\ \chi - \pi \,, & \text{otherwise} \,. \end{cases} \tag{A.20}$$

is sufficient to identify the configurations with opposite signs of μ_1 and μ_2. In fact, under the transformation $\theta \to \pi - \theta$ and $\phi \to 2\pi - \phi$, ω is unchanged while both $\cos\chi$ and $\sin\chi$ change sign that corresponds to the transformation $\chi \to \pi + \chi$. The second symmetry, in this case, derives from the fact that the RSD only depend on $\sin\omega$. Therefore, we can further reduce the extension of parameter space by introducing the variable $\tilde{\omega} = \min(\omega, \pi - \omega)$ so that $\cos\tilde{\omega} = |\cos\omega|$. The set $(\tilde{\omega}, \tilde{\chi})$ is optimal.

A.2 Bias parameters

In Table A.1, we report the forecast errors for the galaxy-bias parameters corresponding to our main analysis presented in Section 2.4.

Table A.1: Expected marginalized 1σ errors for the galaxy bias parameters b_1, b_2 and b_{s^2} in the ΛCDM, wCDM and w_0w_aCDM models obtained considering a *Euclid*-like survey. The different rows display results obtained from the galaxy power spectrum (P, only for b_1), the bispectrum (B), and their combination ($P + B$) for 14 redshift bins centred at redshift z (different columns).

Probe	Param.	0.7	0.8	0.9	1.0	1.1	1.2	1.3	1.4	1.5	1.6	1.7	1.8	1.9	2.0
ΛCDM model															
P	b_1	0.014	0.014	0.015	0.016	0.017	0.017	0.018	0.019	0.020	0.021	0.022	0.023	0.024	0.026
B	b_1	0.046	0.048	0.051	0.053	0.056	0.060	0.066	0.072	0.085	0.097	0.120	0.157	0.189	0.253
$P + B$	b_1	0.012	0.012	0.013	0.013	0.014	0.014	0.015	0.015	0.016	0.017	0.018	0.019	0.020	0.022
B	b_2	0.062	0.064	0.070	0.073	0.080	0.089	0.105	0.125	0.164	0.203	0.272	0.384	0.488	0.684
$P + B$	b_2	0.014	0.015	0.016	0.016	0.017	0.019	0.023	0.027	0.035	0.043	0.057	0.079	0.099	0.137
B	b_{s^2}	0.143	0.144	0.156	0.159	0.175	0.194	0.230	0.270	0.355	0.432	0.572	0.795	0.992	1.365
$P + B$	b_{s^2}	0.070	0.071	0.077	0.079	0.086	0.096	0.113	0.132	0.173	0.210	0.277	0.384	0.479	0.658
wCDM model															
P	b_1	0.024	0.027	0.029	0.032	0.034	0.037	0.039	0.042	0.044	0.047	0.050	0.052	0.055	0.058
B	b_1	0.071	0.077	0.084	0.091	0.099	0.108	0.117	0.127	0.142	0.155	0.176	0.209	0.239	0.296
$P + B$	b_1	0.016	0.017	0.019	0.020	0.022	0.023	0.025	0.027	0.028	0.030	0.032	0.034	0.036	0.038
B	b_2	0.074	0.077	0.084	0.088	0.097	0.107	0.123	0.142	0.180	0.218	0.285	0.394	0.497	0.691
$P + B$	b_2	0.015	0.015	0.016	0.016	0.018	0.019	0.023	0.027	0.035	0.043	0.057	0.080	0.100	0.138
B	b_{s^2}	0.146	0.147	0.158	0.160	0.175	0.194	0.230	0.270	0.355	0.433	0.573	0.795	0.993	1.366
$P + B$	b_{s^2}	0.073	0.075	0.081	0.084	0.092	0.102	0.119	0.138	0.178	0.215	0.282	0.388	0.483	0.661
w_0w_aCDM model															
P	b_1	0.045	0.048	0.052	0.056	0.060	0.065	0.069	0.074	0.079	0.085	0.090	0.095	0.101	0.106
B	b_1	0.090	0.095	0.101	0.107	0.115	0.124	0.134	0.145	0.160	0.175	0.196	0.228	0.259	0.315
$P + B$	b_1	0.019	0.020	0.022	0.023	0.025	0.027	0.029	0.031	0.033	0.035	0.038	0.040	0.043	0.045
B	b_2	0.087	0.089	0.093	0.096	0.103	0.112	0.127	0.146	0.183	0.220	0.287	0.395	0.498	0.692
$P + B$	b_2	0.015	0.015	0.016	0.016	0.018	0.019	0.023	0.027	0.035	0.044	0.058	0.080	0.101	0.138
B	b_{s^2}	0.147	0.147	0.158	0.161	0.176	0.195	0.231	0.271	0.356	0.434	0.574	0.796	0.993	1.366
$P + B$	b_{s^2}	0.077	0.078	0.084	0.087	0.095	0.105	0.122	0.141	0.181	0.218	0.284	0.389	0.484	0.663

List of Figures

List of Tables

Acronyms

COBE *Cosmic Background Explorer*. 4

JWST *James Webb Space Telescope*. 34

WFIRST *Wide Field Infrared Survey Telescope*. 34

WMAP *Wilkinson Microwave Anisotropy Probe*. 4, 36

e-ROSITA *extended ROentgen Survey with an Imaging Telescope Array*. 34

2dFGRS Two-degree Field Galaxy Redshift Survey. 4, 35

ALMA Atacama Large Millimeter Array. 34

BAO baryonic acoustic oscillations. 4, 11, 17, 32, 33, 35

BOSS Baryon Oscillation Spectroscopic Survey. 63

C.L. confidence level. 30, 31

CDM Cold Dark Matter. 2, 10–12, 14–16, 36, 51–53, 55, 57–64, 68, 71, 73, 75, 76, 78, 103, 105

CfA Center for Astrophysics. 2, 4

CMASS constant mass. 63

CMB Cosmic Microwave Background. 2, 4, 6, 11, 14, 16, 33, 36, 55, 63, 69

DESI Dark Energy Spectroscopic Instrument. 35

DETF Dark Energy Task Force. 30, 31, 62, 103

DR12 data reliase 12. 63

EdS Einstein-de Sitter. 17, 19

ESA European Space Agency. 6, 31–33, 103

FLRW Friedmann–Lemaître–Robertson–Walker. 2, 6, 8, 40

FoM figure of merit. 31, 60, 62–66, 69, 73, 75, 77–79, 81, 103, 105

GR General Relativity. 2, 7, 8, 15, 33

LSS large scale structure. 2, 11–13, 17, 103

LSST Large Synoptic Survey Telescope. 34

MCMC Markov chain Monte Carlo. 82

PDF probability distribution function. 21

RSD redshift-space distortions. 23, 25, 26, 31, 33, 38, 39, 41, 42, 45–47, 54, 68, 69, 72, 81, 97, 99, 100, 103

S/N signal-to-noise. 43, 55, 56, 73, 74, 79, 104

SDSS Sloan Digital Sky Survey. 4, 6, 12, 13, 20, 25, 35, 36, 103

SKA Square Kilometre Array. 34, 35

SPT Standard Perturbation Theory. 18, 26, 39, 54

Acknowledgements

It has been a long way for me to make my childhood wish to be a cosmologist true. Since high school, I was working very hard to achieve this goal. Here, I would like to thank everyone who has supported me during such a long way.

I would like to express my deepest gratitude to my supervisor Cristiano Porciani, for giving me the opportunity to do Ph.D. in his group, for offering me such a great and fascinated topic, for his professionalism, for sharing his knowledge, for always having an open door, for his patience, for his advises and his kindness. He is the best supervisor that I could ever have!

I would like to express my sincere acknowledgements to the International Max Planck Research School for Astronomy & Astrophysics at the Universities of Bonn and Cologne, the Transregio 33 'The Dark Universe' of Deutsche Forschungsgemeinschaft, the Argelander-Institut für Astronomie for their financial support during all time of my PhD work through research contras and travel allowances. This support gives me, first of all, the opportunity to participate it the Ph.D. programme, and, secondly, to attend conferences, schools, and collaboration meetings. Special thanks to Bonn-Cologne Graduate School for Physics and Astronomy for their additional travel allowances, Honor branch II grant and 'bridge'-funding.

My sincere gratitude to Sabine Derdau, Christina Stein-Schmitz, Le Tran, Barbara Menten and Simone Pott for their help with the bureaucracy and support.

My special thanks go to Natasha, Marina and Erika, who has been my support since the first minutes in Bonn! Thank you for everything!

I am very grateful to my current and former groupmates and officemates for a nice academic atmosphere. Emilio, Joseph, Enrico, Miko and Davit – thank you for your every day help and support, for our lunches and breaks, for scientific and not only discussions, for your work-related and private advices, for travelling together on conferences and having fun, for all new things I learned from you and our day-to-day life!

Additionally, I would like to thank Katharina and Gerrit, who helped me on my first days in AIfA.

Natasha, Pablo, Marina, Joey, Eleni, James, Ana, Jens, Toma, Vladimir, Eleni, Cristos, Sandra, Alessandro, Henning, Hans, Telemachus, Mary, Maitraiyee, Geomar and other people for all time we spent together; for our chanting and chilling; for dinners, BBQ and parties; for hiking and bouldering; for movie nights and playing board games; for doing sightseeing and travelling together; for everything which makes me laugh and feel happy!!

I would like to give a warm thanks to all my friends and colleagues for their unlimited support and patience during the last months of my thesis writing. Special thanks to James and Marcus for their help with the English language check; to Eric and Jens for help with a LaTeX thesis template.

Special thanks to my friends Jenya, Dima & Oksana, Tanya, Sasha & Sasha, Jora and my 'scientific guardian angel' Sergey for their unlimited support during this long way. I would like to express my deepest gratitude to V.G. Kryshtop, the person who believes in me more than I do myself.

And last but not least, I would like to express my love and gratefulness to my mom Alexandra and uncle Davyd. Their love, support, believe help me every day and especially during my Ph.D. time. I would not be able to make all this way without them. There is no way to express my love and gratitude to them.